Stablaste mreže tenzora za kvantne višečestične sustave na konačnoj temperaturi

Reinić, Nora

Master's thesis / Diplomski rad

2023

UNIVERSITY OF ZAGREB
FACULTY OF SCIENCE
DEPARTMENT OF PHYSICS

Nora Reinić

TREE TENSOR NETWORKS FOR QUANTUM MANY-BODY SYSTEMS AT FINITE TEMPERATURE

Master Thesis

Zagreb, 2022.

SVEUČILIŠTE U ZAGREBU
PRIRODOSLOVNO-MATEMATIČKI FAKULTET
FIZIČKI ODSJEK

Nora Reinić

STABLASTE MREŽE TENZORA ZA KVANTNE VIŠEČESTIČNE SUSTAVE NA KONAČNOJ TEMPERATURI

Diplomski rad

Zagreb, 2022.

UNIVERSITY OF ZAGREB
FACULTY OF SCIENCE
DEPARTMENT OF PHYSICS

INTEGRATED UNDERGRADUATE AND GRADUATE UNIVERSITY
PROGRAMME IN PHYSICS

Nora Reinić

Master Thesis

Tree Tensor Networks for quantum many-body systems at finite temperature

Advisor: Professor Simone Montangero, dr.sc.
Co-Advisor: Professor Tamara Nikšić, dr.sc.

Master Thesis grade: ____________________

Committee: 1. ______________________

2. ______________________

3. ______________________

Master Thesis defence date: _______________
Zagreb, 2022.

Before all, I would like to thank the people who made this possible.

First, to my supervisor Simone Montangero, thank you for opening me a door to the exciting field of the numerical quantum many-body physics and Tensor Networks, and for all the support throughout my research. Next, to Daniel Jaschke, a big thank you for the countless discussions and guidance through my work. And thanks to everyone from Quantum research group for always being open to any questions. Moreover, thanks to all my professors for sharing their knowledge.

To my friends, thank you for being the everlasting source of humour, you made my studies a thousand times more fun.

To my grandma, for promising me a big party when I graduate.

And most importantly, to my parents, thank you for teaching me the beauty of education and the importance of curiosity.

Stablaste mreže tenzora za kvantne višečestične sustave na konačnoj temperaturi

Sažetak

S drugom kvantnom revolucijom na putu, u posljednje vrijeme raste interes za razvojem programabilnih kvantnih uređaja sposobnih nadmašiti klasična računala u određenim zadacima. Budući da se u stvarnosti fizički sustav nikada ne može ohladiti do temperature apsolutne nule, za potpuni opis fizike kvantnih uredaja mora se uzeti u obzir efekte konačne temperature. Međutim, strategije analiziranja svojstava višečestičnih kvantnih sustava na konačnim temperaturama, tj. miješanih kvantnih stanja, zahtijevaju baratanje prostorima u kojima broj parametara raste eksponencijalno s veličinom sustava, te je njihova primjena stoga ograničena na male fizičke sustave. Klasa numeričkih algoritama temeljena na tenzorskim mrežama pokazala se uspješnom u prevladavanju ove poteškoće, proširujući dohvatljive simulacije na veći broj čestica. U okviru ovoga rada razvijen je i implementiran efikasan algoritam za izračunavanje matrice gustoće višečestičnih sustava temeljen na stablastim tenzorskim mrežama. Predstavljene su numeričke tehnike za izračunavanje čistoće stanja, Von Neumannove entropije, Rényijeve entropije proizvoljnog reda, negativnosti i prepletenosti formacije za sustave konačnih temperatura. Metoda je primijenjena na sustavima sastavljenim od $N = 8$, 16 i 32 qubita. Pristup je testiran na jednodimenzionalnom kvantnom Isingovom modelu gdje su uspješno detektirane tri faze - feromagnetska, paramagnetska, i neuređena faza na konačnoj temperaturi, te je kod kritične točke utvrđeno područje najveće prepletenosti. Nadalje, predložena metoda je korištena za proučavanje sustava neutralnih Rydbergovih atoma fiksiranih optičkim pincetama, koji predstavlja jednu od perspektivnih fizičkih platformi kvantnih računala. Kroz ova dva primjera, pokazano je da raspon temperature dohvatljiv našim numeričkim simulacijama ovisi o veličini energetskog procijepa u nisko-energetskom dijelu spektra sustava.

Ključne riječi: kvantni višečestični sustavi, prepletenost, miješana stanja, konačne temperature, mreže tenzora, Rydbergovi atomi

Tree Tensor Networks for quantum many-body systems at finite temperature

Abstract

With the second quantum revolution on its way, there is a rising interest in the development of programmable quantum devices capable of outperforming classical computers in certain tasks. Since, in reality, a physical system can never be cooled down to the absolute zero temperature, the complete description of the physics behind the quantum computing devices has to account for the finite temperature effects. However, strategies for analyzing the properties of quantum systems at finite temperature, i.e. mixed quantum states, require handling of spaces where the number of parameters scales exponentially with the system sizes, and therefore, their application is restricted to small physical systems. The class of numerical algorithms based on tensor network methods has turned out to be successful in overcoming this difficulty, extending possible simulations to large number of particles. Within this thesis, we develop and implement an efficient Tree Tensor Network based algorithm for computing the finite temperature density matrix of the many-body quantum systems. We present the numerical techniques for computing the purity, Von Neumann entropy, Rényi entropies of any order, negativity, and entanglement of formation for the mixed state systems. We apply the method on systems composed of $N = 8$, 16, and 32 qubits. We apply our approach to the one-dimensional quantum Ising model and successfully distinguish the three quantum phases - ferromagnetic, paramagnetic, and the disordered finite-temperature phase, as well as verify the critical point as the point of the largest entanglement. Moreover, we use our method to study the systems of neutral Rydberg atoms trapped in the optical tweezer arrays, representing a physical quantum computing and simulation platform. On these two examples of physical systems, we show that the temperature range accessible to our numerical simulations depends on the gaps between the lower energy levels of the system's spectrum.

Keywords: quantum many-body systems, entanglement, mixed states, finite temperatures, tensor networks, Rydberg atoms

Contents

1 Introduction

Going beyond the classical laws, the rise of the quantum mechanics in the beginning of the twentieth century lead to reestablishing the core concept of the physical reality. The probabilistic approach, once used only as a tool for handling our lack of knowledge about the systems, now turns out to represent the true nature of the physical laws on the micro scales. The idea of exploiting the fundamental principles of quantum physics for a construction of the computing device was born in 1982 as a response to the limitations of the classical simulations of the many-body quantum systems. It was Feynman who suggested, if we want to simulate the quantum systems, we should make a computer whose elements follow the quantum laws [1]. Feynman's suggestion opened the door to a wide new range of possibilities quantum technologies might offer, and today, the potential applications of quantum technologies go beyond the simulation of physical systems, extending to, e.g., quantum cryptography and development of safer communication protocols [2], or even the renewable energy sources [3]. Exploiting superpositions, interference, and entanglement, the theoretical and experimental foundations which allow the construction of the quantum qubits and their elementary operations have been developed [4]. However, the technological obstacle we currently face is that, while such logical gates are possible in small quantum systems, the complete control of a scalable, reliable quantum processor is still an open challenge.

So far, several experimental physical platforms have shown properties suitable for representing the quantum computers, e.g. trapped ions [5–7] and superconductors [8, 9]. In recent years, substantial advancements have been made within quantum computing with neutral Rydberg atoms, opening the door to another promising approach [10–12]. Rydberg atoms are highly excited atoms with the outermost electron being far away from the atomic cation. Due to the extremely large electric dipole moment, they display strong, controllable interactions both among themselves and with an external field [13], making them excellent candidates for programmable quantum devices.

Since in experimental realizations these devices can never be completely cooled down to the absolute zero temperature, there is a particular need for examining their properties at finite temperatures. With the aim of gaining a better understanding of the underlying, collective physical phenomena and improving the accurate control of quantum computing platforms, in this thesis we numerically study the many-body physics of the strongly correlated quantum systems at finite temperatures.

While there are numerous theories dedicated to describing the individual particles, extending the analysis to the systems of large number of physical sites and capturing their collective behaviour is an extremely difficult task, even for the simplest of models. Even though, in principle, we know how to set up the guiding mathematical equations, the problem of the quantum many-body physics lies in the fact that the number of degrees of freedom grows exponentially with the number of particles in the system. Therefore, the complexity of the equations for the large system sizes calls for inventing the appropriate approximations.

From the analytical point of view, the standard approach towards understanding the many-body systems is to propose a simplification of the model, for example Hartree-Fock approximation or random phase approximation. We construct the effective Hamiltonian, and test if it captures the crucial aspects of the original Hamiltonian. However, despite the powerful mathematical techniques and ingenious exploitations of some specific system properties, the fully analytical solutions are still out of reach for the majority of the Hamiltonians. Thus, the integration of analytical simplifications with numerical tools and methods is necessary.

Nevertheless, numerical techniques are as well vastly limited by the exponentially large Hilbert space of the quantum many-body systems. As an example, we take a look at the system of N spin-$1/2$ particles, which resides in the Hilbert space of dimension 2^N. From the computational viewpoint, it can be calculated that storing a complex Hamiltonian matrix with float-like elements for $N = 8$ spins requires $2 \cdot 8 \cdot 2^8 \cdot 2^8 \approx 1.05$ megabytes of memory. However, the exponential scaling implies that this amount escalates very quickly when increasing the number of particles. For the system of $N = 32$ spins, storing a Hamiltonian as a dense matrix already requires $2 \cdot 8 \cdot 2^{32} \cdot 2^{32} \approx 2.95 \cdot 10^5$ petabytes of memory, which is completely out of reach for any exact diagonalization method. Therefore, the exact treatment of the system is limited to only small system sizes, very far away from the thermodynamical limit.

Fortunately, although there is a very large number of possible states in which the system can be, not all of the states are equally relevant. Given that in nature particles often interact only with their nearest neighbours, the majority of the Hilbert space, in fact, stays unpopulated. It can be shown that the low-energy states of non-critical Hamiltonians with local interactions obey the area law of entanglement entropy [14, 15]. Area law tells us that the entanglement entropy of the subregion of space often scales as the boundary area of this subregion, instead of its volume. Only the states which conform to the area law are the candidates for the low-energy eigenstates, reducing the enormously large Hilbert space to a much smaller subspace.

Therefore, by posing the limitations and distinguishing the relevant from unrelevant states, we can avoid handling the entire Hilbert space and drastically save computational resources. Towards the aim of targeting the relevant states and relevant degrees of freedom, a family of numerical methods, called Tensor Network Methods (TNM), has been developed. Within the framework of TNM, quantum objects are parametrized with a set of tensors, decomposing the pure quantum states to the local structures with geometry indicating its bipartite entanglement structure. Hence, the complexity of writing a state in tensor network language scales directly with its content in entanglement. TNM were pioneered by the introduction of the matrix product states (MPS) [16] algorithms, proven to be the equivalent [17, 18] of the density matrix renormalization group (DMRG) previously introduced by White [20] in 1992 as a ground state search method in quantum lattices. Following the success of the MPS, many different TN forms have been constructed, suitable for studying variety of systems of different sizes and in different regimes [21–24].

In this thesis, we develop and implement the TN-based algorithms capable of describing the system properties at finite temperatures. In particular, we examine the purity, Von Neumann entropy, Rényi entropies [25], and the entanglement-related properties negativity [27, 28] and entanglement of formation [26]. However, while quantum correlations are well understood for the pure states, the finite temperature, i.e. mixed state scenario requires substantial effort. Instead of state vectors in the zero-temperature case, the information about the finite-temperature system is contained in the density matrix, and thus studying such systems requires a different, more complex set of tools. To overcome the problem of quantifying the entanglement at finite temperatures, we exploit a particularly convenient TN form, called the Tree Tensor Operators (TTO) [29]. By efficiently compressing the information contained in the density matrices of mixed quantum states, this approach allows the computation of bipartite entanglement measures [30], which are very useful to characterize quantum correlations in the thermal equilibrium in our use case, and more generally, for all mixed quantum states.

To analyze the system, we are faced with the very challenging task of finding the TTO form of the density matrix. In this thesis, we take a deviation via the MPS's mixed state counterpart - the Locally Purified Tensor Networks (LPTN) [31]. To access the system's properties at an arbitrary temperature, we evolve the LPTN form of the infinite temperature density matrix according to the imaginary time evolution [32]. Once we obtain the finite-temperature LPTN density matrix, we convert it to a TTO by the procedure developed in this thesis, using a series of tensor transformations and manipulations.

We apply the algorithms on the well-known 1D Ising model, and on a Rydberg atom model. In particular, we examine a Rydberg chain for system sizes up to 32 qubits, encoding the qubit states into the atom's ground state and into a highly excited Rydberg state.

After the introduction, a short overview of the density matrix formalism is given in Chapter 2, where the density matrix properties and operations are summarized. In Chapter 3, we review the concept of entanglement and why it represents a resource for quantum technologies. The problem of quantifying the entanglement is discussed and two entanglement measures are presented. In Chapter 4, we provide an introduction to Tensor Network Methods, and demonstrate how quantum states and operators are represented with the different Tensor Network forms. In Chapter 5 we then explain the finite-temperature framework and give an overview of the numerical method behind the imaginary time evolution and obtaining the thermal density matrix. Finally, the results of the simulations are presented in Chapter 6 for the Ising model and for the Rydberg atom model.

2 Density matrix formalism

The information about a quantum system is contained in its state. However, there are the situations when we cannot know exactly which particular quantum state describes the system, but can only assign a certain probability of finding it in each of the possible states. Introduced by Von Neumann in 1927 with the motivation of incorporating the statistical mechanics toolbox into the quantum framework, the density matrix formalism allows us to pack both classical and quantum information about the system into a single mathematical object - the density matrix operator. As we will demonstrate in this chapter, extending the concept of quantum states and generalizing it with an operator serves as an elegant way of describing compound systems.

2.1 Density matrix definition and properties

A density matrix, $\hat{\rho}$, is a Hermitian, positive semi-definite matrix, and it is a generalization of the projector operator. We first discuss the case when a system can be described by a state vector, and then extend the mathematical framework to the statistical ensembles of states.

2.1.1 Pure states

When the system is in a defined quantum state, the density matrix is simply equal to the projector to that state,

$$\hat{\rho} = |\psi\rangle \langle\psi| \,, \tag{2.1}$$

and the system is said to be in the *pure state*. Assuming $|\psi\rangle$ is normalized, $\hat{\rho}$ has the following property:

$$\mathrm{Tr}(\hat{\rho}) = 1. \tag{2.2}$$

Since a general state in a discrete finite Hilbert space of the dimension D can be written as:

$$|\psi\rangle = \sum_{n=1}^{D} C_n |\psi_n\rangle , \tag{2.3}$$

where $|\psi_n\rangle$ is some arbitrary orthonormal basis and C_n are the complex coefficients with restriction $\sum_{n=1}^{D} |C_n|^2 = 1$, the general density matrix will have the form:

$$\hat{\rho} = \begin{bmatrix} |C_1|^2 & C_1{C_2}^* & \cdots & C_1{C_D}^* \\ C_2{C_1}^* & |C_2|^2 & \cdots & C_2{C_D}^* \\ \vdots & \vdots & \ddots & \vdots \\ C_D{C_1}^* & C_D{C_2}^* & \cdots & |C_D|^2 \end{bmatrix} . \tag{2.4}$$

More compactly, $\rho_{mn} = \langle\psi_m| \hat{\rho} |\psi_n\rangle = C_m{C_n}^*$. The generalization to the infinite-dimensional Hilbert spaces is possible, but not covered here.

It is easy to show now that density matrix can be used to compute the expectation value of any observable $\hat{O}$, without explicitly accessing the state:

$$\begin{aligned} \langle\hat{O}\rangle &= \langle\psi| \hat{O} |\psi\rangle \\ &= \sum_m \sum_n {C_m}^* C_n O_{mn} = \sum_n \left(\sum_m \rho_{nm} O_{mn} \right) \\ &= \sum_n (\hat{\rho}\hat{O})_{nn} = \mathrm{Tr}(\hat{\rho}\hat{O}). \end{aligned} \tag{2.5}$$

2.1.2 Mixed states

Introducing the density matrix for the pure states does not straightaway seem to have an advantage over the state vector description. But, as stated above, not every system can be associated with a well defined state vector.

Suppose we have a *classical* probability distribution which tells us how likely is to find a system in each of the states $|\psi_j\rangle$. Such system is said to be in the *mixed state*. We define the corresponding density matrix as:

$$\hat{\rho} = \sum_{j=1}^{D} p_j |\psi_j\rangle \langle\psi_j| , \tag{2.6}$$

where p_j is the probability assigned to the state $|\psi_j\rangle$, with $\sum_{j=1}^{D} p_j = 1$. It should be noted that any pure state can be written as a mixed state, with all but one probability equal to zero: $p_i = 1, p_{j\neq i} = 0$.

In a matrix form,

$$\hat{\rho} = \begin{bmatrix} p_1 & 0 & \cdots & 0 \\ 0 & p_2 & \cdots & 0 \\ \vdots & \vdots & \ddots & \vdots \\ 0 & 0 & \cdots & p_D \end{bmatrix}. \tag{2.7}$$

This is a convenient way of storing all available knowledge about the system, and it can be shown that the properties demonstrated above for the pure states hold as well in the mixed state case:

$$\begin{aligned} &\mathrm{Tr}(\hat{\rho}) = 1, \\ &\langle O \rangle = \mathrm{Tr}(\hat{\rho}\hat{O}). \end{aligned} \tag{2.8}$$

Therefore, density matrix is a mathematical tool allowing us to extract the averaged quantities and properties of a general, mixed state system.

2.1.3 Purity

Given a density matrix, a simple way of telling how close the system is to the pure state is to calculate its *purity*. Purity is defined as:

$$\gamma(\hat{\rho}) = \mathrm{Tr}(\hat{\rho}^2). \tag{2.9}$$

Since the trace is invariant of the choice of basis, from the diagonal form of the density matrix in Eq. (2.7) we can read:

$$\gamma(\hat{\rho}) = \sum_{j=1}^{D} p_j^2. \tag{2.10}$$

Therefore,

$$\begin{aligned} &\gamma(\hat{\rho}) = 1 && \text{for pure state } (p_i = 1,\ p_{j\neq i} = 0), \\ &\gamma(\hat{\rho}) = \frac{1}{D} && \text{for maximally mixed state } (\forall p_j = 1/D). \end{aligned} \tag{2.11}$$

The second statement can be proved by inserting the probabilities for maximally mixed state, $\forall p_j = 1/D$, in the definition of purity:

$$\gamma(\hat{\rho}) = \sum_{j=1}^{D} p_j^2 = \sum_{j=1}^{D} \frac{1}{D^2} = D \cdot \frac{1}{D^2} = \frac{1}{D}. \tag{2.12}$$

The closer the purity is to 1, the closer is a system to a pure state.

2.2 Compound systems

Oftenly, we are interested in a system with many different particles, or perhaps we want to take into consideration also the surroundings of our system of interest. It is a common situation that a quantum system is composed out of multiple subsystems. Mathematically, a compound system is described with a tensor product of the subsystems' Hilbert spaces, $\mathcal{H} = \mathcal{H}_1 \otimes \mathcal{H}_2 \otimes ... \otimes \mathcal{H}_N$, N being the number of constituents. Hence, the dimension of the total Hilbert space is equal to the product of the corresponding local Hilbert space dimensions, $d_1 \cdot d_2 \cdots d_N$. A state vector can be written as

$$|\psi\rangle = \sum_{\alpha_1 \alpha_2 ... \alpha_N} C_{\alpha_1 \alpha_2 ... \alpha_N} |\alpha_1\rangle \otimes |\alpha_2\rangle \otimes ... \otimes |\alpha_N\rangle , \tag{2.13}$$

where $\{|\alpha_n\rangle\}$ is a complete set of states in a local Hilbert space of the n-th subsystem, and $\alpha_n = 1, 2, ..., d_n$.

2.2.1 Reduced density matrix

Assume we have a bipartite system, i.e. a system constituting of two distinct parts, A and B, described by a density matrix $\hat{\rho}_{AB}$. Now, suppose we are not interested in the part B, and only want to keep the information about A. Analogously to integrating a joint probability distribution $P(x, y)$ over one variable we are not concerned about, we can obtain the so-called *reduced* density matrix by tracing out a density matrix over all of the states of the subsystem B:

$$\hat{\rho}_A = \mathrm{Tr_B}(\hat{\rho}_{AB}) = \sum_j \langle b_j| \hat{\rho}_{AB} |b_j\rangle , \tag{2.14}$$

where $\{|b_j\rangle\}$ is the basis of the subsystem's B Hilbert space. Reduced density matrix $\hat{\rho}_A$ contains a maximal information we can have about system A independently of B.

2.2.2 Schmidt decomposition

Another useful tool for studying the composite systems is the *Schmidt decomposition* [33]. The theorem of Schmidt decomposition states that for any pure state $|\psi\rangle$ of the bipartite system AB, there exists a set of orthonormal states $\{|a'_n\rangle\}$ for system A and $\{|b'_n\rangle\}$ for system B, such that

$$|\psi\rangle = \sum_n \lambda_n |a'_n\rangle |b'_n\rangle \,, \tag{2.15}$$

where λ_n are the real non-negative numbers satisfying $\sum_n \lambda_n^2 = 1$, called the Schmidt coefficients.

Written in the Schmidt basis, a density matrix has the form:

$$\hat{\rho}_{AB} = \sum_{nm} \lambda_n \lambda_m |a'_n\rangle |b'_n\rangle \langle a'_m| \langle b'_m| \,, \tag{2.16}$$

giving the reduced density matrices:

$$\begin{aligned} \hat{\rho}_A &= \sum_n \lambda_n^2 |a'_n\rangle \langle a'_n| \,, \\ \hat{\rho}_B &= \sum_n \lambda_n^2 |b'_n\rangle \langle b'_n| \,. \end{aligned} \tag{2.17}$$

Thus, as one of the consequences of the Schmidt decomposition, $\hat{\rho}_A$ and $\hat{\rho}_B$ have the identical eigenvalues, λ_n^2.

With the Schmidt decomposition, we conclude the overview of the elementary density matrix toolbox. In the following chapter, we extend this toolbox by relating it to the concept of quantum *entanglement*.

3 Entanglement

There is a crucial concept of the quantum theory allowing the existence of long-distance inter-particle correlations intrinsically different from the classical ones. Such purely quantum correlation is referred to as the entanglement. For a long time, entanglement was a source of confusion among the scientists, being the main concern of the famous EPR [34] paradox arguing the completeness of the quantum theory. After the response to the paradox arrived in the form of Bell's inequalities [35], many experimental and theoretical efforts have been put in improving our understanding of the quantum correlations. But, having a new set of rules dictating the nature's microscopical behaviour is not only the interesting peculiarity, moreover - it is also a very powerful resource, enabling the invention of the new, quantum-based technologies [36]. Today, the experimental progress allows us to isolate, prepare and control individual quantum systems, exploiting their entanglement for the development of algorithms and protocols capable of solving certain tasks much faster than its classical counterparts. Thus, the task of characterizing and quantifying the entanglement is of the uttermost importance.

We begin this chapter by defining the entanglement in terms of separable and non-separable states. Then, we introduce the entropy in the context of the information theory, and connect the classical Shannon entropy to the quantum Von Neumann entropy. Starting from the concept of local operations and classical communication, we discuss the problem of quantifying the entanglement and present some commonly used entanglement measures. Through the chapter, we focus mostly on the concept of the bipartite entanglement, i.e. correlation between two subsystems.

3.1 Separable and entangled states

Given a compound quantum system, entanglement implies that each of the subsystems cannot be described independently of the others. Performing a measurement on one subsystem may affect the outcome of the measurements on the other one. Separability is the concept opposite to entanglement, meaning that if the state is separable, then it is not entangled. In this section, we mathematically define separability for both pure and mixed states.

3.1.1 Pure state separability

A state of a composite system in a pure state is said to be *separable* if it can be written as the tensor product of the states of each of its constituents. Thus, a separable state of a bipartite system AB has a form:

$$|\psi\rangle = |\psi_A\rangle \otimes |\psi_B\rangle = (\sum_i A_i |a_i\rangle) \otimes (\sum_j B_j |b_j\rangle), \tag{3.1}$$

where $\{|a_i\rangle\}$ and $\{|b_j\rangle\}$ are the bases of Hilbert spaces of subsystems A and B, respectively. The corresponding density matrix is:

$$\hat{\rho}_{AB} = |\psi_A\rangle \langle\psi_A| \otimes |\psi_B\rangle \langle\psi_B| . \tag{3.2}$$

Calculating the reduced density matrices of Eq. (3.2) gives:

$$\begin{aligned} \hat{\rho}_A &= |\psi_A\rangle \langle\psi_A| \\ \hat{\rho}_B &= |\psi_B\rangle \langle\psi_B| . \end{aligned} \tag{3.3}$$

Therefore, a reduced density matrix of a separable pure state system is again a pure state. In other words, separability implies we can have the access to the quantum information about each individual part of the system, regardless of the other parts.

However, when a system is in the *entangled* state, the complete knowledge about the compound system does not imply the complete knowledge about its parts. As an example, we consider a state of two two-level quantum systems, i.e. two qubits:

$$|\psi\rangle = \frac{1}{\sqrt{2}}(|00\rangle + |11\rangle). \tag{3.4}$$

where the notation $|ab\rangle$ denotes that the first qubit is in state $|a\rangle$, and the second qubit is in state $|b\rangle$. State in Eq. (3.4) is one of the so-called Bell states, and it is one of the maximally possible entangled state. We can see from Eq. (3.4) that measuring a state of one qubit completely determines the outcome of the measurement on the second qubit. A density matrix can no longer be written in a factorized form, such as in Eq. (3.2), and the corresponding reduced density matrices will have the mixed character:

$$\hat{\rho}_A = \begin{bmatrix} \frac{1}{2} & 0 \\ 0 & \frac{1}{2} \end{bmatrix}, \qquad \hat{\rho}_B = \begin{bmatrix} \frac{1}{2} & 0 \\ 0 & \frac{1}{2} \end{bmatrix}. \tag{3.5}$$

We see that, independently of the first qubit, we will always have a classical probability $1/2$ of finding the second qubit in each of the states, and *vice versa*.

It can be generalized for any entangled state that tracing the density matrix over one of the subsystems yields a mixed state.

3.1.2 Mixed state separability

We have shown that computing a reduced density matrix of a pure state reveals whether a system is in the separable or entangled state. Next, we may ask if a similar criterion can be constructed for the compound system which is initially in the mixed state.

A separable mixed state implies a state with only classical and no quantum correlation between the subsystems. To make this statement more understandable, we explain one possible way, proposed by Werner in 1989 [37], of preparing the classically correlated, separable state of two systems A and B. Suppose we have two devices, each with a setting $j = \{1, ..., n\}$ such that a setting j sets a system i in the state $|\psi_j^i\rangle$. Then, suppose we also have a random number generator, generating a number j with a probability p_j. The mixed state-creating apparatus is set to first generate a random number j, and then switch both devices to the same setting j. Clearly, such two systems are correlated only with a classical random number choice. The corresponding density matrix is:

$$\hat{\rho}_{AB} = \sum_j p_j \; |\psi_j^A\rangle \langle\psi_j^A| \otimes |\psi_j^B\rangle \langle\psi_j^B| = \sum_j p_j \; \hat{\rho}_j^A \otimes \hat{\rho}_j^B. \tag{3.6}$$

Eq. (3.6) is the definition of a separable mixed state. The system is separable if we can find the decomposition as in Eq. (3.6) of the system's density matrix.

Nevertheless, given an arbitrary $\hat{\rho}$, its decomposition over a set of states (not necessarily orthonormal) is not unique, and proving if a decomposition as in Eq. (3.6) exists is not a trivial task. Hence, we are in need for the alternative entanglement measures [38].

3.2 *Entropy*

In this section, we provide a review of the entropy, as a very important quantity in both classical and quantum information theory. We start by motivating the need of quantifying the uncertainty present in the system, and introduce the Von Neumann entropy as a quantum analogue of the classical Shannon entropy. We then mention some of the properties, and introduce the Rényi entropy, as a more general definition of entropy.

3.2.1 Shannon entropy

The Shannon entropy of some variable quantifies how much information, on average, we gain after we learn the value of that variable. Therefore, entropy measures the amount of the information stored in the system. The reason why it is useful to quantify the information is because it tells us directly about the amount of the physical resources needed to store this information (see [33]).

For a variable with D possible outcomes and the probability p_j of obtaining the j-th outcome, Shannon entropy is defined as:

$$\mathcal{S} = -\sum_{j=1}^{D} p_j \log p_j. \tag{3.7}$$

The choice of the logarithm base depends on the application. The basis of 2 expresses the entropy in units of bits, but the other bases, such as natural logarithm, are also used. From now on, we will use the logarithm basis of two.

To make the definition in Eq. (3.7) more intuitive, we can explicitly calculate the result for several specific cases. On the one hand, when a variable has one certain outcome, there is only one non-zero probability, $p = 1$, and the Shannon entropy is equal to zero. In other words, we did not gain any information, because we could predict the outcome with certainty. On the other hand, for a variable with D outcomes and equal probability of obtaining each of them, $p_j = 1/D$, the Shannon entropy is equal to $\log D$. Since the equal probability for each outcome implies the largest uncertainty in the outcome, such probability distribution has the largest possible Shannon entropy. As an example, the Shannon entropy of the two-outcome variable,

$$x = \begin{cases} 1 & \text{with } p \\ 0 & \text{with } 1-p, \end{cases} \tag{3.8}$$

is shown in Fig. 3.1 as a function of p.

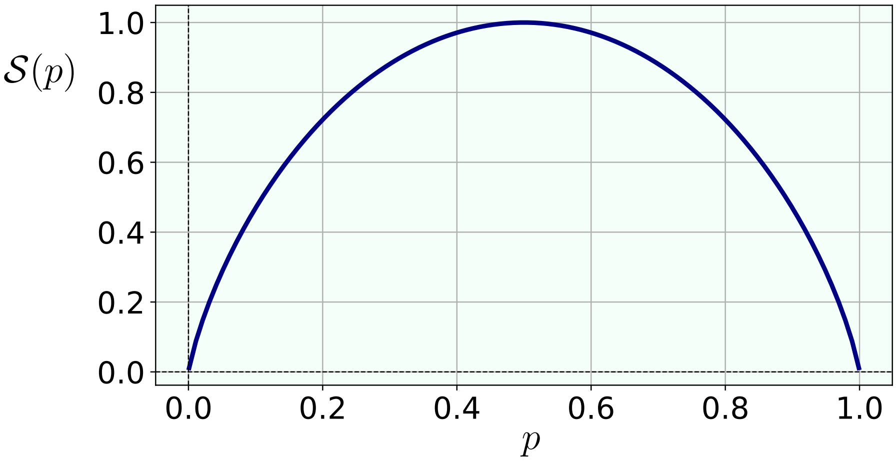

Figure 3.1: Shannon entropy of the two-outcome variable.

3.2.2 Von Neumann entropy

In the quantum case, classical probability distribution is included in the density matrix. Therefore, the generalized expression of the Shannon entropy to the quantum case depends on the system's density matrix:

$$\mathcal{S}(\hat{\rho}) = -\mathrm{Tr}(\hat{\rho} \log \hat{\rho}), \tag{3.9}$$

Eq. (3.9) defines the Von Neumann entropy. Von Neumann entropy is the quantum extension of the Gibbs entropy from the classical statistical mechanics. We may rewrite Eq. (3.9) using the diagonalized form of $\hat{\rho}$:

$$\mathcal{S}(\hat{\rho}) = -\sum_j (p_j \log p_j), \tag{3.10}$$

The eigenvalues are denoted with p_j because they correspond to the mixed state probabilities.

The previous discussion on entropy in the special cases can now be translated to the density matrix language: the Von Neumann entropy is equal to zero when the state is pure, and maximal when the state is maximally mixed. Hence, opposite to the purity (defined in Eq. (2.9)), the Von Neumann entropy tells us how much the system is mixed.

Some of the important Von Neumann entropy properties are:

- Entropy is non-negative:

  $$0 \leq \mathcal{S}(\hat{\rho}) \leq \mathcal{S}(\hat{\rho}_{mm}), \tag{3.11}$$

  where $\hat{\rho}_{mm}$ denotes the maximally mixed density matrix.

- Entropy is invariant under unitary transformations:

  $$\mathcal{S}(\hat{\rho}) = \mathcal{S}(\hat{U}\hat{\rho}\hat{U}^{\dagger}). \tag{3.12}$$

  $\mathcal{S}(\hat{\rho})$ depends only on eigenvalues of $\hat{\rho}$, which do not change with the unitary transformation (change of basis).

- For a composite system AB in a pure state, entropy of each of the subsystems is equal:

  $$\mathcal{S}(\hat{\rho}_A) = \mathcal{S}(\hat{\rho}_B). \tag{3.13}$$

  Recalling the Section 2.2 and the Schmidt decomposition, Eq. (3.13) is the direct consequence of Eq. (2.17).

3.2.3 Rényi entropy

For a discrete probability distribution $\{p_1, ..., p_n\}$, Rényi entropy of order α is defined as [25]:

$$\mathcal{S}_\alpha(\hat{\rho}) = \frac{1}{1-\alpha} \log \left(\sum_j p_j^\alpha \right), \tag{3.14}$$

where $\alpha > 0$ and $\alpha \neq 1$. Eq (3.14) represents the generalized definition of entropy and, in the case $\alpha \longrightarrow 1$, it coincides with the Shannon entropy. It can be shown (see e.g. [39]) that the concept of Rényi entropy becomes very useful in the thermodynamics of fractals, where it can be connected to the generalized fractal dimension.

3.3 Local operations and classical communication

Before we continue to the discussion about the entanglement measures, we provide a short motivation behind the entanglement quantification by explaining how a maximally entangled quantum state can be transformed into any pure state shared between the two parties, Alice and Bob. For that purpose, we introduce the concept of local operations and classical communication (LOCC).

Suppose Alice and Bob share a state of two qubits, so that one of the qubits is given to Alice and the other one is given to Bob. Local operations imply that Alice can only perform the operations (such as unitary transformations and measurements) on her qubit, and Bob can only operate on his. Classical communication means they can exchange the information only in a classical manner. For example, they are allowed to call each other and discuss the results of their measurements, but they are not allowed to exchange any quantum systems.

The important restriction here is that LOCC transformations cannot create the entanglement in the system [40]. However, as we will shortly demonstrate, LOCC can be used to transform one entangled state into another entangled state. Therefore, if some state $\hat{\rho}_1$ cannot be obtained by performing the LOCC on $\hat{\rho}_2$, this means that $\hat{\rho}_2$ does not contain enough entanglement to produce $\hat{\rho}_1$. Thus, the LOCC's no-entanglement-creation rule yields a very nice consequence, that is, we are given the ability to compare and order the states by the amount of their entanglement.

Now, lets say Alice and Bob share a pair of a maximally entangled pure state

$$|\psi\rangle = \frac{1}{\sqrt{2}}(|0\rangle_A |0\rangle_B + |1\rangle_A |1\rangle_B). \tag{3.15}$$

The index A denotes the qubit which belongs to Alice, and index B denotes the qubit which belongs to Bob. We show how the maximally entangled state can be transformed into any other pure state via LOCC. Since there is a Schmidt decomposition for every two-qubit state, we may write it as:

$$|\phi\rangle = \alpha |0\rangle_A |0\rangle_B + \beta |1\rangle_A |1\rangle_B . \tag{3.16}$$

The protocol converting $|\psi\rangle$ to $|\phi\rangle$ is the following [41]: first, Alice introduces to her system the additional qubit which is in state $|0\rangle$. This additional qubit is furthermore referred to as the *ancilla* qubit. The state now looks like this:

$$\frac{1}{\sqrt{2}}(|00\rangle_A |0\rangle_B + |01\rangle_A |1\rangle_B). \tag{3.17}$$

Then, Alice performs the unitary transformation on her two qubits:

$$\begin{aligned} |00\rangle &\longrightarrow \alpha |00\rangle + \beta |11\rangle) \\ |01\rangle &\longrightarrow \beta |01\rangle + \alpha |10\rangle), \end{aligned} \tag{3.18}$$

and we arrive to the state

$$\frac{1}{\sqrt{2}}\Big(|0\rangle_A (\alpha |0\rangle_A |0\rangle_B + \beta |1\rangle_A |1\rangle_B) + |1\rangle_A (\beta |1\rangle_A |0\rangle_B + \alpha |0\rangle_A |1\rangle_B)\Big). \tag{3.19}$$

Next, Alice makes the measurement on the ancilla qubit and reports the result to Bob. There are two possible outcomes: the ancilla is either in the state $|0\rangle$, and the state has collapsed to Eq. (3.17) meaning no further operations are needed, or the ancilla is in the state $|1\rangle$, and Bob needs to apply the σ_x operator to his qubit. Clearly, both cases result in the desired state. In a similar way it can be shown that, starting from a maximally entangled state, we can obtain any mixed state $\hat{\rho}$.

Transforming a general state into some other general state is, however, a bit more complicated problem to consider. It turns out that, in most of the cases, we cannot perform the desired conversion with certainty, but only with some probability.

In order to overcome this issue, it is convenient to study a bit more general situation in which consider a problem

$$\hat{\rho}^{\otimes n} \longrightarrow \hat{\sigma}^{\otimes m}, \tag{3.20}$$

i.e., we are transforming n copies of state $\hat{\rho}$ into m copies of state $\hat{\sigma}$. The largest ratio m/n for which such transformation can be achieved tells us about the relative entanglement content of $\hat{\rho}$ and $\hat{\sigma}$. There is again the possibility to demand the transformation in Eq. (3.20) to be achieved exactly, with 100% chance of success, but we can also decide it is acceptable to allow some extent of uncertainty. In the latter, the imperfections can be arbitrarily reduced with increasing the n, and thus it is useful to consider the *asymptotic regime* in which $n \longrightarrow \infty$. Ratio m/n can thus be interpreted as the asymptotic number of states $\hat{\sigma}$ that can be prepared from $\hat{\rho}$.

3.4 Quantifying the entanglement

With the introduction to LOCC and state transformations, we have set the ground for introducing some possible ways of quantifying the entanglement. We start by presenting the three axioms posed by Vedral et al. [42], constructed as the requirements for testing whether some mathematical quantity complies with the physical concepts associated with the entanglement. These axioms are today seen as the elementary conditions every entanglement measure, $E(\hat{\rho})$, has to satisfy:

- $E(\hat{\rho}) = 0$ *for separable states,*

  because the entangled states are defined as non-separable states.

- $E(\hat{\rho})$ *does not change under local unitary transformations,*

  because local unitary transformation represent the change of basis, and entanglement does not depend on which basis we choose.

- *$E(\hat{\rho})$ cannot be increased by LOCC,*

  because each of the LOCC transformations are either local, therefore cannot increase the correlation inside the whole system, or classical, therefore they can only decrease the entanglement or leave it unchanged.

There are many possible functions known to conform to these requirements, and in this thesis, we introduce two of them: entanglement of formation, whose physical interpretation continues to the story of the state transformations, and negativity, as a more mathematical approach to measuring entanglement.

However, there is one more quantity left to be explained before proceeding to the entanglement of formation and negativity. In the following section, we introduce the *entanglement entropy*.

3.4.1 Entanglement entropy

Entanglement entropy of a pure state composite system AB is defined as:

$$\mathcal{S}_E(\hat{\rho}_{AB}) = \mathcal{S}(\hat{\rho}_A) = \mathcal{S}(\hat{\rho}_B), \tag{3.21}$$

where $\hat{\rho}_A$ and $\hat{\rho}_B$ are reduced density matrices, and $\mathcal{S}(\hat{\rho})$ is Von Neumann entropy. The second equality follows from a fact that Von Neumann entropy depends only on the eigenvalues of the density matrix, and by the Schmidt decomposition, both reduced density matrices $\hat{\rho}_A$ and $\hat{\rho}_B$ have the same eigenvalues. For the convenience, we may rewrite $\mathcal{S}_E(\hat{\rho}_{AB})$ in terms of the Schmidt coefficients,

$$\mathcal{S}_E(\hat{\rho}_{AB}) = -\sum_n \lambda_n^2 \log(\lambda_n^2). \tag{3.22}$$

The simple analysis of Eq. (3.21) reveals that $\mathcal{S}_E(\hat{\rho}_{AB})$ serves as the measure of entanglement between the subsystems A and B for pure states. Recalling the discussion from Section 3.2.2, we know that the Von Neumann entropy measures the degree of mixture of a density matrix. From the Section 3.1.1 we know that, if the pure state is separable, the reduced density matrix is a pure state, and if the state is entangled, the reduced density matrix is a mixture. Hence, it follows that the degree of mixture of the reduced density matrix (and therefore $\mathcal{S}_E(\hat{\rho}_{AB})$) directly indicates the amount of entanglement in the system. It can be calculated:

$$\mathcal{S}_E(\hat{\rho}) = 0 \qquad \text{for separable state,} \tag{3.23a}$$

$$\mathcal{S}_E(\hat{\rho}) = \log(d) \qquad \text{for maximally entangled state,} \tag{3.23b}$$

where d is the local Hilbert space dimension of the subsystems.

As a follow-up to the Section 3.3, it is $\mathcal{S}_E$ which is conserved in the asymptotic regime of the pure state case of Eq. (3.20). As $n \longrightarrow \infty$, the ratio m/n approaches $\mathcal{S}_E(\hat{\rho})/\mathcal{S}_E(\hat{\sigma})$ [43]. Taken into account Eq. (3.23b), it follows that $\mathcal{S}_E(\hat{\rho})$ represents both the asymptotic number of maximally entangled qubit pairs needed to prepare $\hat{\rho}$, and asymptotic number of maximally entangled pairs that can be prepared from $\hat{\rho}$.

Nevertheless, although entanglement entropy completely characterizes the pure state correlations, the mixed state case is again much less understood and calls for more complex methods. There is no unique way of characterizing the mixed state entanglement, and different measures with different physical interpretations have been constructed.

3.4.2 Entanglement of formation

Here we present the *entanglement of formation* (EoF) as one approach to generalizing the entanglement entropy to the mixed states. EoF is defined as:

$$E_F(\hat{\rho}) = \inf_{\psi_j, p_j} \Big\{ \sum_j p_j \mathcal{S}_E(|\psi_j\rangle) \quad : \quad \hat{\rho} = \sum_j p_j \left|\psi_j\right\rangle \left\langle\psi_j\right| \Big\}, \tag{3.24}$$

and it represents the minimal average entanglement entropy over all pure state decompositions of $\hat{\rho}$ [26].

The reason behind a name “entanglement of formation” is that this quantity is expected to be closely related to the asymptotic number of maximally entangled pairs needed to prepare a certain state, i.e. the entanglement cost, $E_C(\hat{\rho})$. So far, it has been shown that the entanglement cost is equal to the regularization of EoF,

$E_F^{\infty}(\hat{\rho})$, defined as:

$$E_F^{\infty}(\hat{\rho}) = \lim_{n\to\infty} \frac{E_F(\hat{\rho}^{\otimes n})}{n}. \tag{3.25}$$

If $E_F(\hat{\rho})$ turns out to be additive, that is:

$$E_F(\hat{\rho}_1 \otimes \hat{\rho}_2) = E_F(\hat{\rho}_1) + E_F(\hat{\rho}_2), \tag{3.26}$$

the equality $E_F(\hat{\rho}) = E_F^{\infty}(\hat{\rho})$ follows. Since the entanglement cost is very complicated to compute (see page 11 of [41] for the mathematical definition), proving that $E_C(\hat{\rho}) = E_F(\hat{\rho})$ would present a major simplification. There are some theoretical and numerical indications of this equivalence.

However, finding the EoF is not an easy task as well, and the analytical solutions of Eq. (3.24) are found only for a few special cases (e.g. for two-qubit states [44]). Therefore, for a general state, the value of EoF can only be accessed through the numerical computations.

3.4.3 Negativity

As already said, for a pure state, the separability can be proved by calculating the Schmidt coefficients of the reduced density matrix and computing the entanglement entropy. Although the same test cannot be applied to the mixed states as well, there is another mathematical check serving as the mixed state separability criterion. The Peres-Horodecki, or the Positive Partial Transpose (PPT) criterion was first proposed by Peres [27] and Horodecki family [28] in 1996, and it presents a necessary requirement for the mixed state to be separable. Note here that, *necessary* does not imply *sufficient* - the PPT criterion has been proved a sufficient separability criterion only for the cases of the Hilbert space dimensions 2×2 and 2×3. The PPT criterion states: if $\hat{\rho}$ is separable, then the density matrix partially transposed with respect to one part of the system will have all non-negative eigenvalues. The partial transpose of the density matrix over one part of the system is defined as:

$$\hat{\rho}^{T_A} = \sum_{ijkl} C_{ijkl} (|a_i\rangle \langle a_j|)^T \otimes |b_k\rangle \langle b_l| = \sum_{ijkl} C_{ijkl} |a_j\rangle \langle a_i| \otimes |b_k\rangle \langle b_l| . \tag{3.27}$$

Therefore, if one or more eigenvalues of $\hat{\rho}^{T_A}$ is negative, the state is not separable. This condition is used to construct an entanglement monotone called *negativity*, defined as:

$$\mathcal{N}(\hat{\rho}) = \frac{\|\hat{\rho}^{T_A}\|_1 - 1}{2}, \tag{3.28}$$

where $\|X\|_1$ is the trace norm, $\|X\|_1 = Tr(\sqrt{X^\dagger X})$. An equivalent definition of negativity is:

$$\mathcal{N}(\hat{\rho}) = \sum_{j} \frac{|\lambda_i| - \lambda_i}{2}, \tag{3.29}$$

where λ_i are the eigenvalues of $\hat{\rho}^{T_A}$. Eq. 3.29 represents the sum over all negative eigenvalues of $\hat{\rho}^{T_A}$.

Equipped with all the theoretical prerequisites, we can now continue to the problem of numerical computation of the presented properties and, in particular, the quantum many-body mixed state properties.

4 Tensor Networks

In this chapter, we introduce the Tensor Network Methods (TNM) [21,22], a class of numerical methods proved to be successful in escaping (to some extent) the obstacle of exponentially-scaling computational complexity in quantum many-body problems. Starting from the definition of tensor, we present the standard Tensor Network (TN) graphical notation and simple tensor manipulations. Then, for the examples of Tree Tensor Networks and Locally Purified Tensor Networks, we demonstrate how quantum states and operators can be transformed and represented through different TN configurations and we show how TN give us the direct access to entanglement structure of quantum states.

4.1 *Tensors and tensor network diagrams*

An N-rank tensor is the N-dimensional array of complex-valued elements, where each of its elements can be accessed through a list of N indices. While there are common names for the several low-rank tensors (Fig. 4.1), a general tensor can be denoted as

$$T_{\alpha_1\alpha_2\ldots\alpha_N}, \qquad \alpha_n = 0, 1, ..., d_n - 1, \tag{4.1}$$

where d_n is the dimension of the n-th axis.

name	rank	symbol
scalar	0	A
vector	1	A_i
matrix	2	A_{ij}

Figure 4.1: Low-rank tensor names and symbols.

A TN is a group of tensors, possibly mutually connected with index contractions. The index contractions imply the summation over the certain index. One basic example is the matrix-matrix multiplication, where the contraction is done over the inner index:

$$C_{ij} = \sum_k A_{ik} B_{kj}. \tag{4.2}$$

The uncontracted indices are referred to as the free indices.

However, one can build much more complicated TN structures, and thus, it is very convenient to introduce the appropriate graphical notation. Within a graphical notation, a tensor is represented with a shape, and his indices are the legs emerging from the shape, as shown in Fig. 4.2.

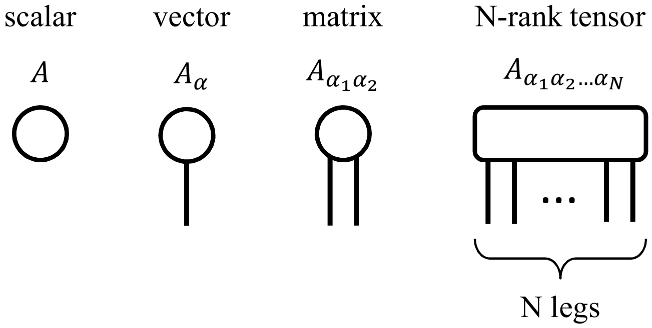

Figure 4.2: Graphical representation of tensors.

The index contraction is represented as the link connecting the two tensors. Following these rules, the example of a matrix-matrix multiplication operation can now be visualised as a diagram in Fig. 4.3.

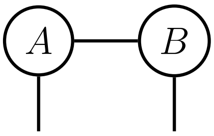

Figure 4.3: Graphical representation of matrix-matrix multiplication.

To make the advantage of using the graphical notation more clear, one can take a look at a bit more complicated TN described by Eq. (4.3), and Fig. 4.4.

$$E_\alpha = \sum_{\beta\gamma\delta\sigma} A_{\alpha\beta} B_{\beta\gamma\delta} C_{\gamma\sigma} D_{\delta\sigma}. \tag{4.3}$$

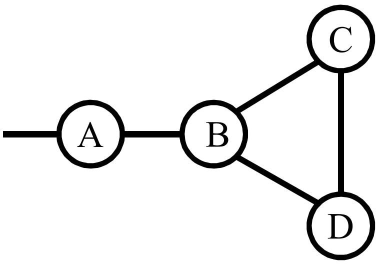

Figure 4.4: Tensor network representing Eq. (4.3).

While in the linear algebra notation the tensor contraction structure might not be apparent at first sight, TN diagrams provide a direct visual insight into the tensors' mutual relations. Thus, writing the TN in a visual form can reveal some, otherwise not-straightforward, properties.

4.2 *Tensor operations*

With the notation defined, we now introduce the basic tensor operations, as a technical prerequisite needed to understand the key idea behind the TNM and the numerical algorithm employed in this thesis.

4.2.1 Index splitting and fusing

A tensor's multidimensionality can be viewed as a tool for storing the information in a structured way. One can notice that, for example, the elements of a vector with 4 components can also be stored into the 2x2 matrix:

$$\begin{bmatrix} a_1 \\ a_2 \\ a_3 \\ a_4 \end{bmatrix} \longrightarrow \begin{bmatrix} a_1 & a_2 \\ a_3 & a_4 \end{bmatrix} . \tag{4.4}$$

In fact, any tensor of some dimension D can be reshaped into an n-rank tensor, with the condition that the product of all of the new axis dimensions corresponds to D. Further, we refer to this as the index splitting.

Of course, such operation can be reversed, and the multiple tensor axis can be fused into one axis. The same condition as the above holds again, hence the tensor of some dimensions $d_1, d_2, ..., d_n$ can only be reshaped into a tensor of the dimension $D = d_1 \times d_2 \times ... \times d_n$. This operation is referred to as the index fusing. Index manipulations can be further generalized to reshaping any N-rank tensor to the tensor of different rank, if the axis dimensions are appropriate.

A graphical depiction of these operations is shown in Fig. 4.5.

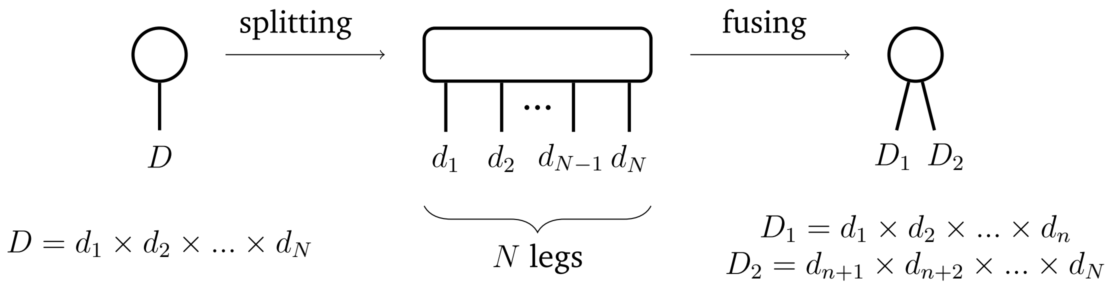

Figure 4.5: Example of reshaping a tensor by index splitting and fusing.

Therefore, there is always a certain freedom in choosing a tensor shape, which allows us to adapt and choose the most appropriate one based on the situation. As we describe later on, the index splitting and fusing are of great importance when it comes to handling quantum many-body objects.

4.2.2 Singular Value Decomposition

The Singular Value Decomposition (SVD) is a generalization of the eigenvalue decomposition to the case of rectangular matrices. Via the SVD, we can decompose any matrix $\mathbf{A} \in \mathbb{C}^{L \times M}$ into the product of three matrices:

$$A_{ij} = \sum_{k=1}^{K} S_{ik} V_{kk} D_{kj}, \qquad K = min(L, M), \tag{4.5}$$

such that $\mathbf{S} \in \mathbb{C}^{L \times K}$ and $\mathbf{D} \in \mathbb{C}^{K \times M}$ are unitary, and $\mathbf{V} \in \mathbb{R}^{K \times K}$ is diagonal, real and positive. The values on the diagonal of matrix **V** are called the singular values.

The importance of SVD lies in the fact that it can be exploited to compress the information contained in a matrix, which is widely used in big data analysis and image processing (see e.g. [45]). The information compression implies discarding a part of the information contained in a matrix. Singular values can be seen as the weight factors distinguishing between which information is valuable to keep, and which is not.

Suppose the diagonal entries in the **V** matrix are ordered in descending order. The number of non-zero singular values is equal to the rank of matrix **A**. Hence, the dimension K can be reduced to the rank of **A** without any loss of the information. Going even further, we can discard all of the singular values smaller than a certain value ε and reduce the dimension to some m_{ε}. On top of that, a maximal allowed bond dimension m_{max} is usually chosen. Therefore, **A** is approximated with:

$$A_{ij} \approx \sum_{j=1}^{m} S_{ik} V_{kk} D_{kj}, \qquad m = \min\{m_\varepsilon, m_{max}\}. \tag{4.6}$$

This corresponds to projecting the matrix onto the reduced subspace spanned by only the remaining left and right singular vectors. The advantage of SVD is that the error produced by truncating the singular values is completely controllable and trackable. In practice, truncation allows us to drastically reduce the dimensions of the matrices. Having in mind that any n-rank tensor can be reshaped into a matrix by fusing its legs, TNM rely on SVD as the main mechanism for information compressing and computational cost reduction.

The SVD operation is graphically shown in Fig. 4.6. After the truncation of the small singular values, the diagonal matrix **V** can be multiplied with **S** or **D**, or $\sqrt{\mathbf{V}}$ can be multiplied with both **S** and **D**. In any case, there remain two matrices of reduced link dimensions. Hereafter, the green dashed rectangle around the tensors in figures will denote the contraction of the enclosed tensors.

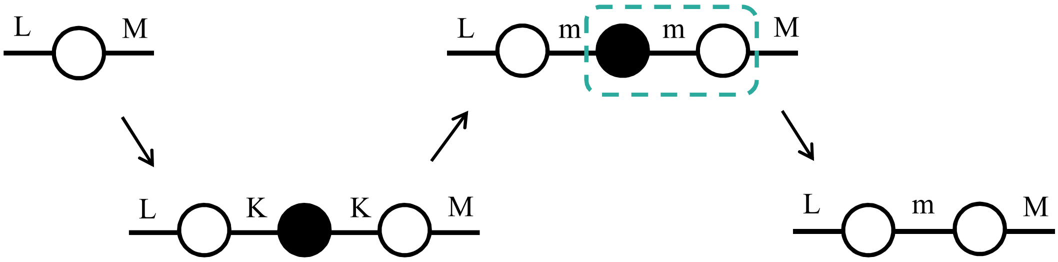

Figure 4.6: Singular Value Decomposition and truncating the bond dimensions. Green dashed rectangles denote the contraction of the enclosed tensors. The bond dimensions are indicated above the tensor legs.

4.2.3 Computational complexity of tensor contractions

To give the insight in how the tensor dimensions influence the computational complexity of the algorithm, we calculate the number of operations needed to perform some simple tensor contractions.

Suppose the dimensions of all of the following tensor legs are equal to m. A scalar product of two vectors, $w = \sum_{j=1}^{m} u_j v_j$, requires $\mathcal{O}(m)$ operations (Fig. 4.7a). A matrix-vector multiplication, $v_i = \sum_{j=1}^{m} A_{ij} u_j$, requires the summation of m elements, for each of the m elements of the resulting vector. Therefore, the total computational complexity is $\mathcal{O}(m^2)$ (Fig. 4.7b). Folowing the analogous logic, performing the matrix-matrix multiplication $C_{ij} = \sum_{k=1}^{m} A_{ik} B_{kj}$ requires $\mathcal{O}(m^3)$ operations

(Fig. 4.7c). A more complex example of the contraction is depicted in Fig. 4.7d. The generalization to the contraction of any two tensors with the total number of free and contracted indices equal to N, yields the computational complexity of $\mathcal{O}(m^N)$. Note that the contracted index is counted only once.

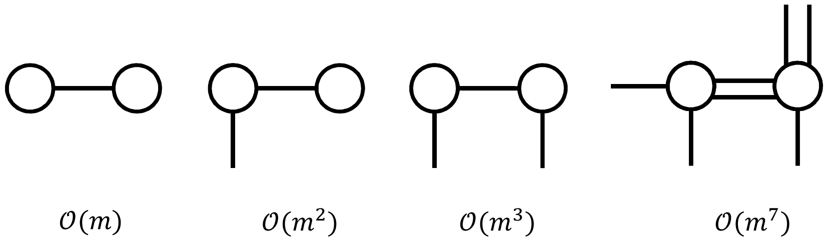

Figure 4.7: Computational complexity of different tensor network contractions. The bond dimension of all the legs is assumed to be the same and equal to m.

It is important to emphasize that, when handling the more complex TN, the number of operations needed for contracting the entire TN will depend on the order in which the indices are contracted. As an example, to contract the TN from Fig. 4.8, one could do it by taking each of the possible ways shown. However, the upper way in Fig. 4.8 up takes $m^5 + m^4 + m^2 = \mathcal{O}(m^5)$ operations in total, while the lower way requires $m^4 + m^4 + m^3 = \mathcal{O}(m^4)$ operations. Therefore, among the tactics for optimizing the TN algorithms is to find the most efficient way of contracting the certain network.

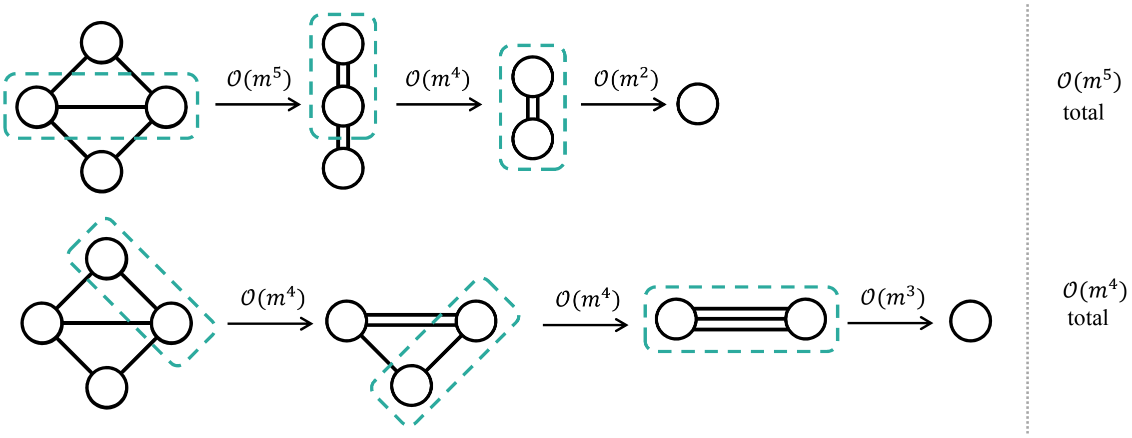

Figure 4.8: Different ways of contracting a tensor network. Green dashed rectangles denote the contraction of the enclosed tensors. The bond dimension of all the legs is assumed to be the same and equal to m. The contraction requires either $\mathcal{O}(m^5)$ operations (top) or $\mathcal{O}(m^4)$ operations (bottom).

4.3 Quantum objects as tensor networks

A quantum many-body wave function of N particles can be written as follows:

$$|\psi\rangle = \sum_{\alpha_1\alpha_2...\alpha_N} C_{\alpha_1\alpha_2...\alpha_N} |\psi_{\alpha_1}\rangle \otimes |\psi_{\alpha_2}\rangle \otimes ... \otimes |\psi_{\alpha_N}\rangle\,, \tag{4.7}$$

where $\alpha_n = 1, 2, ..., d_n$, and d_n is the dimension of the local Hilbert space of the n-th particle. For the sake of simplicity, we assume all of the particles reside in the local Hilbert space of the same dimension d. Therefore, it takes d^N coefficients to describe a generic N-particle quantum state.

In the case of a separable state, the wave function can be rewritten as the tensor product of each of the local states:

$$\begin{aligned} |\psi\rangle &= |\Psi_1\rangle \otimes |\Psi_2\rangle \otimes ... \otimes |\Psi_N\rangle \\ &= \Big(\sum_{\alpha_1} C_{\alpha_1} |\psi_{\alpha_1}\rangle\Big) \otimes \Big(\sum_{\alpha_2} C_{\alpha_2} |\psi_{\alpha_2}\rangle\Big) \otimes ... \otimes \Big(\sum_{\alpha_N} C_{\alpha_N} |\psi_{\alpha_N}\rangle\Big). \end{aligned} \tag{4.8}$$

Instead of d^N coefficients for the case of general state, one needs $N \cdot d$ coefficients to describe a separable state. Therefore, by assuming that no quantum correlations exist between the particles, the scaling of the size of the object needed to store the state information is reduced from exponential to linear dependence on the number of particles. However, despite the very tempting reduction to the linear scaling, treating the physical system as completely separable, i.e. in the mean field approximation, has its limitations.

TN allow us to recognize and preserve the important particle correlations, while retaining the reasonable object size. It can be shown (see [46]) that, by applying basic tensor transformations and SVD, a wave function can be recast to:

$$|\psi\rangle = \sum_{\beta_1\beta_2...\beta_{2(N-1)}} C^{\beta_1}_{\alpha_1} C^{\beta_1\beta_2}_{\alpha_2} ... C^{\beta_{2(N-1)}}_{\alpha_N} |\psi_{\alpha_1}\rangle \otimes |\psi_{\alpha_2}\rangle \otimes ... \otimes |\psi_{\alpha_N}\rangle\,, \tag{4.9}$$

The form in Eq. (4.9) is called the Matrix Product State (MPS). The indices α_n are referred as the physical indices, and β_n are referred as the auxiliary ones.

To make it more comprehensible, a graphical representation of the wave functions in Eq. (4.7), (4.8), and (4.9) is shown in Fig. 4.9. Each of the tensors in the separable wave function (Fig. 4.9b) and MPS (Fig. 4.9c) represents one physical site. Instead of working with the whole wave function, separating it to smaller pieces enables us to distinguish between the sites and perform local operations on each of them. Unlike the separable case, where the tensors are mutually independent, in MPS form there are additional links between the sites representing the quantum particle correlations. The dimension of the auxiliary links can be controlled through SVD, and it can be shown that the obtained singular values scale directly with the amount of entanglement present in the system. Therefore, for a weakly entangled system, the auxiliary bond dimensions is smaller than in the case of a very entangled system.

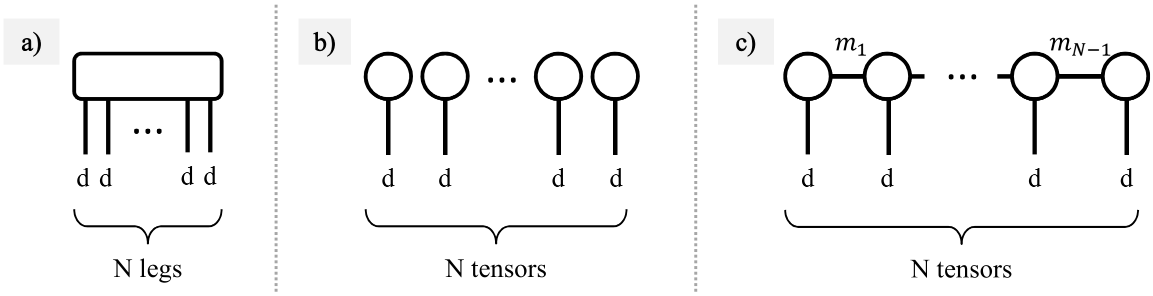

Figure 4.9: State vector as a tensor network. a) General wave function described by d^N coefficients. b) Separable wave function. c) Matrix product state form of a wave function.

Although MPS have shown to be very successful in solving a broad range of problems, by their definition, they represent the pure states. Therefore, the finite-temperature regime, i.e. the mixed state scenario, requires a different strategy.

4.3.1 Locally Purified Tensor Networks

As already discussed in Chapter 2, systems consisting of statistical ensembles cannot be treated as pure states, and are handled within the density matrix formalism. The information about all of the possible states, together with the associated probabilities, is contained in the density matrix operator:

$$\rho = \sum_{j=1}^{K_0} p_j \left|\psi_j\right\rangle \left\langle\psi_j\right| , \tag{4.10}$$

where K_0 is the number of pure states contributing to the density matrix.

Since MPS algebra is thoroughly examined and a large number of techniques are developed within the MPS framework, it is useful to extend the concept of MPS to the mixed state systems. Towards this aim, the density matrix operators with the analogous TN structure are constructed. There are multiple possible approaches to attack this issue (e.g. [47, 48]). In this section, we present the Locally Purified Tensor Network (LPTN) form of a density matrix [31], which is exploited to efficiently compute the density matrix operator of a system at finite temperature.

A density matrix is, by the definition, a positive definite operator. Hence, it can be decomposed as:

$$\rho = XX^\dagger, \tag{4.11}$$

with X_j being the unitary matrix with columns equal to $\sqrt{p_j}\,|\psi_j\rangle$. The number of columns, K_0, is equal to the rank of ρ. Therefore, any density matrix can be depicted with the diagram in Fig. 4.10.

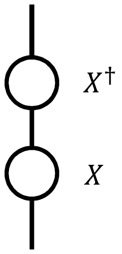

Figure 4.10: Density matrix as a product of two matrices, $\rho = XX^\dagger$, where $X = \sqrt{p_j}\,|\psi_j\rangle$.

In the LPTN form, each of the two tensors, X and $X^\dagger$, have a structure similar to the MPS. The tensor structure of the LPTN for $N = 4$ is depicted with a diagram in Fig. 4.11. Since the two sides of the LPTN are Hermitian conjugates of each other, it is sufficient to store only the elements of X. Elements of $X^\dagger$ can be provided if needed. In the LPTN form, each of the tensors of X (or $X^\dagger$) corresponds to one of the physical sites, i.e. particles in a system.

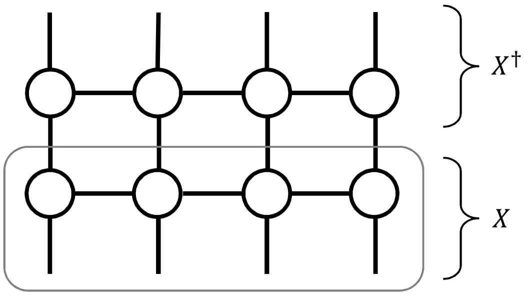

Figure 4.11: Locally purified tensor network form of the density matrix. The part of the tensor network enclosed in the gray rectangle corresponds to X, and the remaining part corresponds to $X^\dagger$.

To give an idea of how the tensor structure of the quantum objects can be manipulated, we now demonstrate how to convert the density matrix from a matrix form to the LPTN form. It should be noted that this procedure is usually not suitable for the practical use, as handling the matrix form of the density matrix is within reach only for the small system sizes. For the bigger systems, we use the methods completely based on TN.

As stated above, we can work with only one side of the operator, X. The transformation is described following the steps in Fig. 4.12. The matrix is oriented so that the lower leg represents the index of the wave function component. Therefore, the lower leg has a dimension of a total Hilbert space, d^N. Upper leg represents the index j from Eq. (4.10), and its dimension is K_0. Suppose that $K_0 = d^N$, which corresponds to the general case in which the density matrix is decomposed over the complete set of states.

As explained in the Section 4.2.1, a tensor leg of appropriate dimension can be split into legs of smaller dimensions. Hence, we can split both lower and upper leg of the X matrix, each into two legs of dimensions d and $d^N - 1$, as shown in Fig. 4.12b. Now, recalling we are also allowed to fuse multiple legs into one, we can fuse them as in Fig. 4.12c. We arrive to the matrix form again, but with matrix shape and order of elements modified in comparison to the initial X. We then perform the SVD on the new matrix and truncate the bond dimensions (Fig. 4.12d). Next, we multiply the diagonal matrix to the right unitary matrix and arrive to the form as in Fig. 4.12e. At this point, we have the left tensor isolated. The left tensor corresponds to the first physical site. In the same manner, we separate each of the remaining sites as well. Thus, we repeat the described procedure on the right tensor and iterate until N tensors are obtained. The iteration is depicted in Fig. 4.12f - 4.12g.

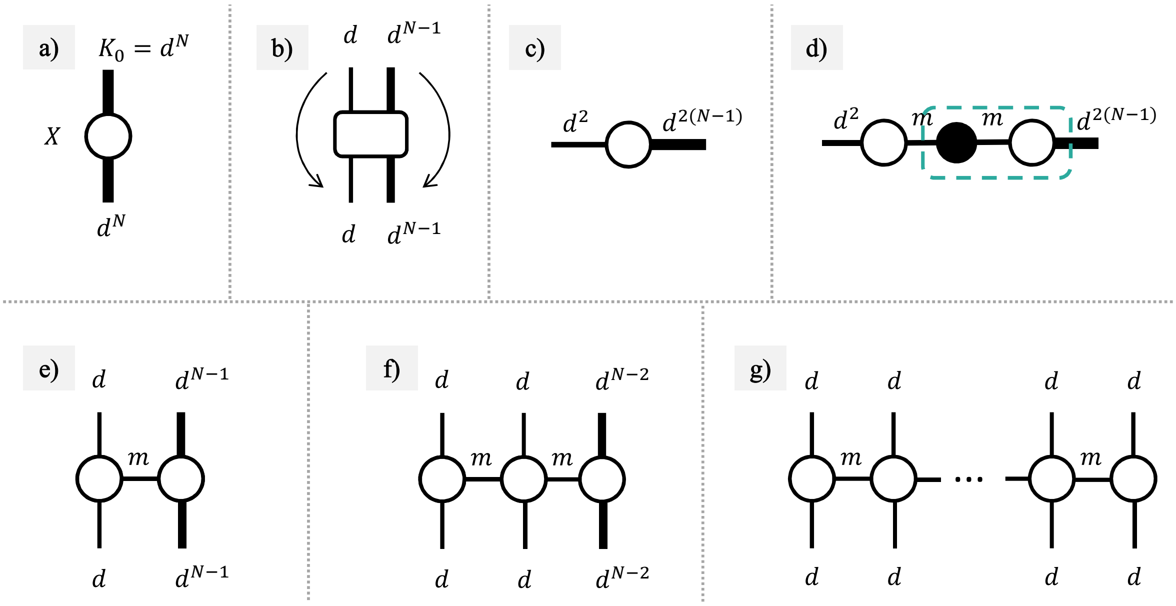

Figure 4.12: Conversion of the density matrix operator from a matrix form to the locally purified tensor network form. The procedure shows how to convert X into one side of the locally purified density matrix. The other side corresponds to $X^\dagger$ and is obtained by taking a Hermitian conjugate of each of the tensors. Arrows denote fusing of the two legs. Green dashed rectangles denote the contraction of the enclosed tensors.

The auxiliary bonds in the LPTN again represent the correlations between the sites, and their dimension is proportional to the amount of entanglement in the system. Since LPTNs allow us to handle density matrices within the MPS framework, they offer a valuable toolbox for achieving a speedup of certain algorithms. In Chapter 5, the LPTN time evolution algorithm for closed systems is discussed.

4.3.2 Tree Tensor Networks

However, in this thesis, we thoroughly explore a different TN representation, called the Tree Tensor Network (TTN) [29]. As we show, the TTNs are found to be extremely suitable for handling the mixed state systems and are able to achieve a drastic decrease of the computational cost of calculating the system's properties within a density matrix formalism. In this chapter, we provide the technical introduction to the TTN, while their application to the finite temperature states is discussed in the next chapter.

The TTN form of the quantum state for $N = 8$ particles is shown in Fig. 4.13. Unlike the MPS, TTN offers the entanglement representation along the bipartite split of each the branches of a tree. The TTN's structure is hierarchical, and the wave function contains $\log_2(N)$ layers. With the top layer being the zeroth, and counting towards the bottom, the n-th layer contains 2^n tensors, each with one leg connecting it to the upper-layer tensor, and two legs branching to the two lower-layer tensors. The bottom layer tensors have two free legs, each of the legs representing one physical site. The dimensions of the free legs are equal to the local Hilbert space dimension d. For the example of 8 sites (TTN in Fig. 4.13), the bottom layer contains 4 tensors and 8 legs in total.

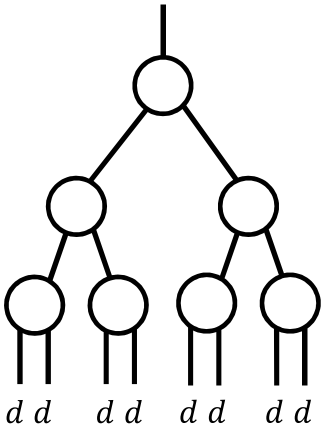

Figure 4.13: Tree tensor network representation of the $N = 8$ quantum state. The legs of the bottom layer tensors have the dimension d of the local Hilbert space, and represent the physical sites.

Now, we demonstrate how to convert a wave function from the vector form to the TTN form. Since any vector of some dimension M can be reshaped into a matrix of dimension $M \times 1$, we can start the conversion procedure from the matrix form. Avoiding a vector form and starting the conversion from a matrix turns out to be more convenient for iterating the certain steps, and will also be necessary later, when we introduce the TTN density matrix.

The key transformation needed for the conversion is depicted in Fig. 4.14a. Starting from a matrix, we aim to recast it to a TN with the three new tensors, and we explain in the next paragraph how to achieve this step in all details. One can notice that tensors of the lower layer of the right structure in Fig. 4.14a) are also matrices. Therefore, we can grow the next lower layer by performing the exact same transformation on each of the two new matrices (Fig. 4.14b)). It is not difficult to see now that, in order to obtain the TTN wave function, one simply needs to iterate the layer-creating procedure and stop once the number of layers reaches $\log_2(N)$.

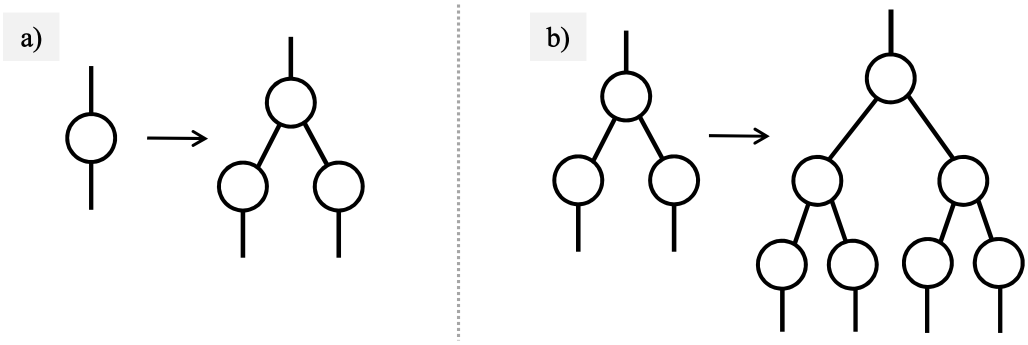

Figure 4.14: Conversion of a matrix into a tree tensor network. a) Transformation of a matrix into the tree-like structure (details explained below). b) Growing a layer on a tree tensor network.

What is left to describe is how exactly is the transformation in Fig. 4.14a) performed. Having a matrix, as in Fig. 4.15a), we can split the leg of dimension d^N into two legs of dimension $d^{N/2}$ each (Fig. 4.15b)). Then, we fuse the legs to obtain a matrix again, so that legs on each of the sides of the red dashed line in Fig. 4.15b) are fused together. We perform the SVD on the obtained matrix, truncate the bond dimensions, and get the TN on the Fig. 4.15c). Further, we fuse the legs as indicated with the red dashed line in Fig. 4.15c), and perform the SVD and truncation on the rightmost tensor. We arrive at the form in Fig. 4.15d). Then, we contract the diagonal matrices with the middle one and, finally, reach the form in Fig. 4.15e), where the dimensions of the bonds between the upper and lower tensors are reduced to some dimension $m < d^{N/2}$.

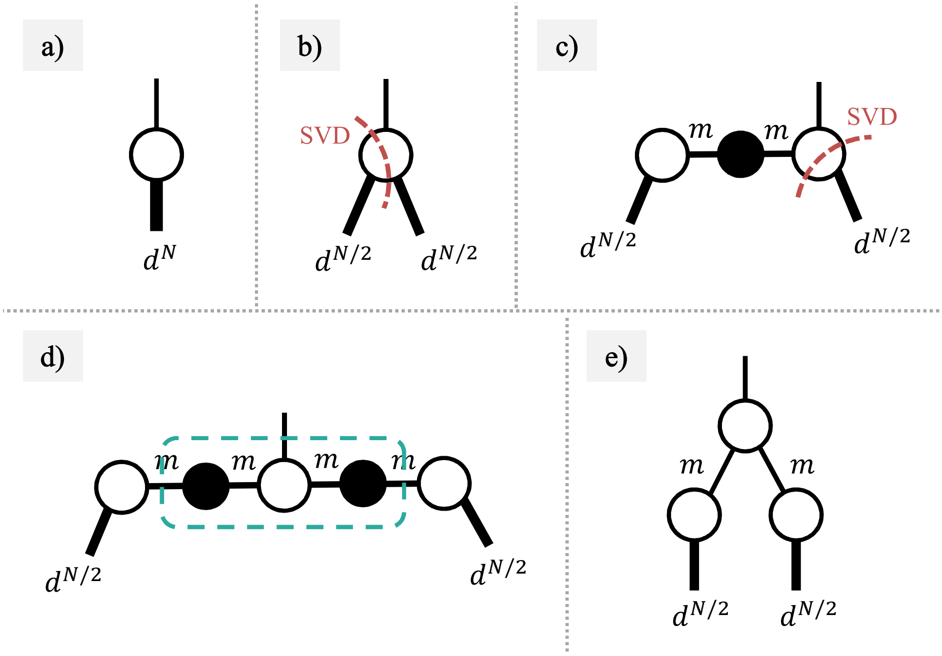

Figure 4.15: Steps for decomposing a matrix into the tree-like structure. Red dashed line defines reshaping of tensor into matrix: the tensor legs above the red dashed line are fused into one matrix leg, and the tensor legs below the red dashed line are fused into the other matrix leg. Green dashed rectangles denote the contraction of the enclosed tensors.

Nevertheless, a TTN wave function can still represent only a pure state. To describe a mixed state, we need a TN form representing the density matrix operator. Thus, in the next section we introduce the Tree Tensor Operators (TTO).

4.3.3 Tree Tensor Operators

A general TTO form is shown on the Fig. 4.16. Unlike the TTN wave function, a TTO has two tree-like sides, grown from each of the legs of the operator in matrix form. The general TTO conversion procedure is shown In Fig. 4.17: in order to transform an operator from a matrix to the TTO form, we first perform the SVD and multiply the diagonal matrix with one of the unitary matrices. Then, we grow the tree structure on each of the obtained tensors in exactly the same manner as we did in the case of the wave function TTN.

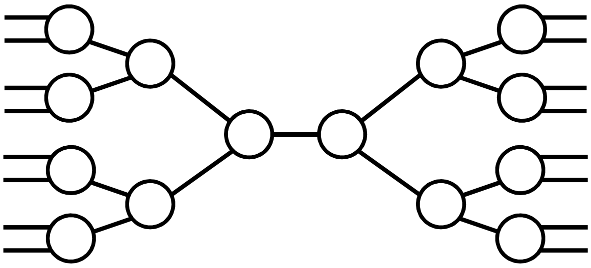

Figure 4.16: Tree tensor operator.

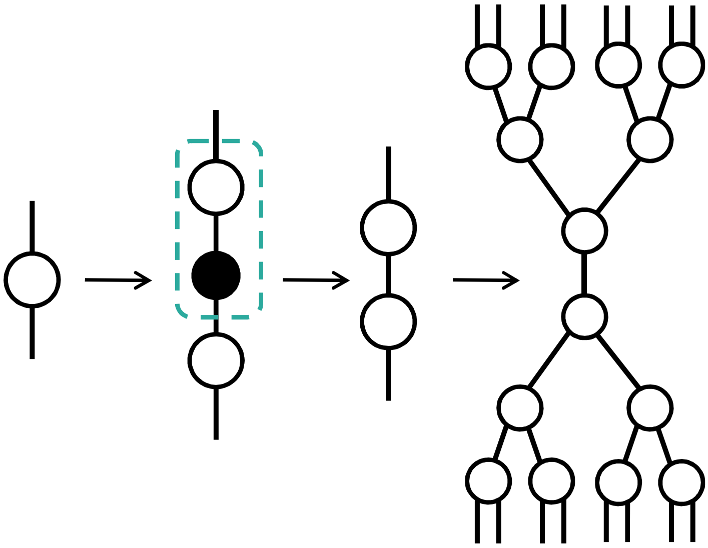

Figure 4.17: Obtaining a tree tensor operator from a matrix.

Now, we have covered all of the concepts needed to understand why TTO is a natural form for a mixed state density matrix operator. Recalling that a density matrix can be written in a form $\rho = XX^{\dagger}$, one can see that it already contains the connecting link between the two sides of the TN operator (Fig. 4.18). Hence, for the TTO density matrix operator we understand the physical meaning of the connecting link.

$$\rho = \sum_{j=1}^{K_0} p_j |\psi_j\rangle\langle\psi_j| \; = \; XX^\dagger =$$

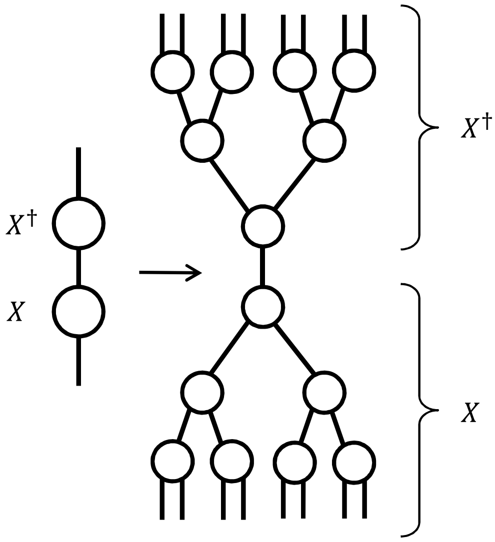

Figure 4.18: Density matrix as a tree tensor operator.

5 Finite temperature algorithms

In this Chapter, we turn the attention to the physical problem of our interest, that is, quantum many-body systems at finite temperature. Within the previous chapters, we introduced the mathematical framework of the density matrix, theory behind the entanglement, and TN as numerical tools. Now we show that quantum many-body systems at finite temperature are a physical realization of mixed states, and present the TN-based numerical method we developed to simulate such systems and extract their entanglement-related properties.

5.1 Quantum systems at finite temperature

Equilibrium statistical physics for classical systems lies on the fact that, in systems consisting of extremely large number of constituents, the detailed individual particle correlations are macroscopically suppressed. If we limit ourselves to some arbitrary precision of measurement, there will always exist a characteristic timescale on which the system is chaotic and we are no longer able to predict the individual particle behaviour for the certain initial conditions. On the larger time scales, the behaviour of the particles appears to be randomized. Moreover, even if (in some hypothetical, physically impossible situation) we were able to measure the behaviour of each of the particles with the absolute precision, the randomness can never be completely removed. Every system is always a part of a bigger system and, therefore, it will always be influenced by the random interactions at the boundaries. Of course, if we could predict even these boundary interactions, the boundary problem would not disappear, it would only redefine what we consider by our system, i.e. shift the existing boundaries a bit further. Thus, there will always exist a characteristic time after which the distribution of particles is no longer correlated with the current distribution of particles.

Physical systems consist of a very large number of particles, order of magnitude of the Avogadro number 10^{23}, thus we definitely cannot rely on following the individual systems and interactions among them. Since the interactions are rapid, during the time of our measurement, the system passes through a large number of the microscopic configurations. It can be justified that looking at the system at equilibrium state is equal to looking at one randomly chosen configuration from the ensemble of all of the possible system configurations.

The fundamental postulate of the classical statistical mechanics is that all of the microscopic configurations of the closed system are equally probable. However, multiple microscopic configurations can realize the same macroscopic state. Hence, some macroscopic states are more probable than others and there exists the stationary probability distribution. We include the additional restrictions and knowledge about our system by modifying the probability distribution to match our constraints.

In this thesis, we are interested in the systems described by the canonical ensemble, i.e. the system has a fixed volume and a number of particles, but can exchange energy with the surroundings and are currently at equilibrium. Such systems are in the thermal equilibrium, meaning the system is fixed at some finite temperature T, where T is the property of the surroundings.

Since the system's total energy is not fixed, the microscopical configurations differ in energy. A corresponding probability distribution can be derived (see e.g. [49]), and a probability p_j can be assigned to each configuration with a total energy E_j:

$$p_j = \frac{1}{Z} e^{-\beta E_j}, \quad Z = \sum_i e^{-\beta E_i}, \quad \beta = \frac{1}{k_B T}. \tag{5.1}$$

The normalization factor Z is called the partition function, and $k_B = 1.380649 \cdot 10^{-23}$ JK^{-1} is the Boltzmann constant.

Now, since in reality, physical systems are built from particles obeying the quantum mechanical laws, each energy E_j corresponds to some quantum energy state $|\psi_j\rangle$. Considering that p_j are the classical probabilities of finding a system in each of the quantum states $|\psi_j\rangle$, we can recognize that the canonical ensemble corresponds to a mixed state with the density matrix

$$\hat{\rho} = \sum_j \frac{e^{-\beta E_j}}{Z} |\psi_j\rangle \langle\psi_j| = \frac{e^{-\beta \hat{H}}}{Z}, \tag{5.2}$$

where $\hat{H}$ is the system's Hamiltonian. Therefore, the density matrix formalism is a natural way of describing the quantum systems at finite temperatures. From now on, we refer to the finite temperature density matrix as the *thermal* density matrix.

Notice here that the probabilities decay exponentially with the system's energy, and the rate of the decay depends on the system's temperature. For the low temperatures, the decay is rapid, and only the first few low-energy states contribute to the density matrix, as the probabilities of finding the system in a high-energy states are negligible. In the limit $T \longrightarrow 0$, the system collapses into the ground state. If the ground state is n-fold degenerate, the state will be a coherent superposition of the first n states. Increasing the temperature increases the probability of finding a system in higher-energy states. In the limit $T \longrightarrow \infty$, system approaches a maximal mixture, where all of the states contribute equally, with a probability $1/d^N$.

5.2 Obtaining the density matrix

Quantum systems at finite temperature are fully described with their density matrix operator. Once we obtain this operator for a given quantum system, we can use it to study different properties. However, finding the thermal density matrix of the many body quantum system is by no means an easy task.

The algorithm described in this section is the core part of this thesis. Our aim was to develop and test the TNM-based method capable of obtaining the many-body thermal density matrix in a TTO form, suitable for efficient extraction of the system's properties. Our method for acquiring the thermal density matrix is a two-step proces. First, we obtain the density matrix in the LPTN form by evolving it according to imaginary time evolution, and then we convert it to the TTO. The first step is described in the Section 5.2.1, and the second step is described in Section 5.2.2.

All codes for the described numerical algorithms were made within this research work and are included in the PY_API_QUANTUM_TEA_LEAVES Python library. The exception is the imaginary time evolution algorithm, which was already implemented within the QUANTUM_GREEN_TEA Fortran library. Both libraries are developed within the Quantum research group at the University of Padova and are licensed under the Apache License, Version 2.0.

5.2.1 Imaginary time evolution

As already mentioned, the system at infinite temperature is in a maximally mixed state. Hence, we can write the corresponding density matrix as:

$$\hat{\rho}_\infty = \begin{bmatrix} \frac{1}{N} & 0 & \cdots & 0 \\ 0 & \frac{1}{N} & \cdots & 0 \\ \vdots & \vdots & \ddots & \vdots \\ 0 & 0 & \cdots & \frac{1}{N} \end{bmatrix} = \frac{1}{N}\mathbb{1}. \tag{5.3}$$

Since the infinite temperature density matrix is proportional to the identity matrix, we can always insert it in a definition of the arbitrary thermal density matrix from the Eq. (5.2) as follows:

$$\hat{\rho} = \frac{e^{-\beta\hat{H}}}{Z} = \frac{1}{Z}e^{-\frac{\beta}{2}\hat{H}}\mathbb{1}e^{-\frac{\beta}{2}\hat{H}} = \frac{N}{Z}e^{-\frac{\beta}{2}\hat{H}}\hat{\rho}_\infty e^{-\frac{\beta}{2}\hat{H}} = \frac{N}{Z}e^{-\frac{\beta}{2}\hat{H}}\hat{\rho}_\infty(e^{-\frac{\beta}{2}\hat{H}})^\dagger. \tag{5.4}$$

In the last expression from Eq. (5.4), we recognize the form of a unitary time evolution of the density matrix operator, $e^{-\frac{\mathrm{i}t}{\hbar}\hat{H}}\hat{\rho}(0)(e^{-\frac{\mathrm{i}t}{\hbar}\hat{H}})^\dagger$, with the substitution $\mathrm{i}t/\hbar \to \beta/2$. Therefore, to obtain a density matrix at an arbitrary temperature, we can evolve the maximally mixed density matrix using the ordinary time evolution algorithms and apply the appropriate substitution. The procedure is called the *imaginary time evolution*. From now on, we choose the units $k_B = 1$ and $\hbar = 1$.

However, in the case of many-body systems, performing the time evolution is not a trivial operation. In this thesis, we are concerned with the local nearest-neighbour interactions. We consider the time-independent Hamiltonian of the form:

$$\hat{H} = \sum_{j=1}^{N}\hat{A}_i + \sum_{j=1}^{N-1}\hat{B}_j\hat{C}_{j+1}, \tag{5.5}$$

where $\hat{A}_j$, $\hat{B}_j$, $\hat{C}_j$ are some arbitrary local operators acting on the physical site j. The terms in the second sum in Eq. (5.5) represent the interactions between the nearest-neighbour sites.

To perform the time evolution, we exploit the LPTN form of the density matrix, and use the time-evolving block-decimation algorithm [32, 47]. As every tensor in each of the sides of the LPTN represents a physical site, the local operator acting on the j-th site can be applied directly to the j-th tensor, by contracting the corresponding leg. The operation is shown in Fig 5.1.

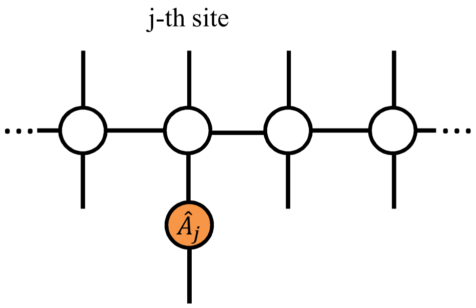

Figure 5.1: Applying the local operator on one side of the LPTN density matrix. The operator acting on the j-th site is applied directly to the j-th tensor.

As all of the $\hat{A}_j$ terms from Eq. (5.5) belong to different local Hilbert spaces, they mutually commute. Therefore, if a Hamiltonian in Eq. (5.5) contained only the $\hat{A}_j$ terms, the unitary time evolution operator $e^{-\frac{it}{\hbar}\hat{H}}$ could be decomposed as:

$$e^{-\mathrm{i}t\sum_j \hat{A}_j} = \prod_j e^{-\mathrm{i}t\hat{A}_j}, \tag{5.6}$$

and evolving the density matrix to the time t would simply be achieved by applying each of the local operators $e^{-\mathrm{i}t\hat{A}_j}$ to the corresponding sites (shown in Fig. 5.2).

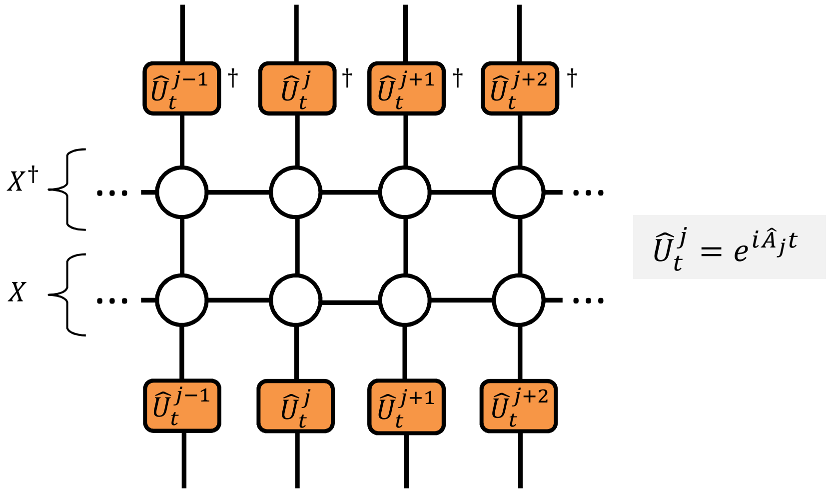

Figure 5.2: Density matrix time evolution for time-independent Hamiltonian which can be written as a sum of local, mutually commuting operators $\hat{A}_i$.

Nevertheless, when the particle interactions are present, the terms in Eq. (5.5) in general do not commute. However, the problem of the non-commutation occurs only for the neighbouring two-site terms, which act on the same local Hilbert space. Thus, we can decompose the Hamiltonian as the sum of the two parts, $\hat{H} = \hat{H}_1 + \hat{H}_2$,

$[\hat{H}_1, \hat{H}_2] \neq 0$, so that each of the two parts contains only the mutually commuting terms:

$$\hat{H} = \sum_{k=0}^{2k+1\leq N} \left(\hat{A}_{2k+1} + \hat{B}_{2k+1}\hat{C}_{2k+2}\right) + \sum_{k=1}^{2k\leq N} \left(\hat{A}_{2k} + \hat{B}_{2k}\hat{C}_{2k+1}\right) = \hat{H}_1 + \hat{H}_2. \tag{5.7}$$

The statement that terms within each $\hat{H}_{i=1,2}$ commute can be seen more clearly when switching to the graphical notation. In Fig. 5.3, we show the operators $\hat{H}_1$ and $\hat{H}_2$ applied to one of the sides of the LPTN. We can see that $\hat{H}_1$ contains all the two-site operators acting on odd sites and their right neighbours, and $\hat{H}_2$ contains all the two-site operators acting on even sites and their right neighbours. There is no overlap between the Hilbert spaces of any of the operators in each $\hat{H}_{i=1,2}$.

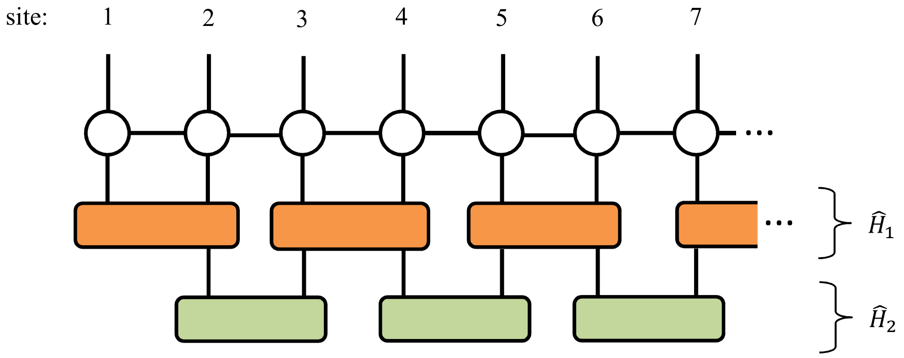

Figure 5.3: Applying $\hat{H}_1$ and $\hat{H}_2$ on one side of the locally purified tensor network. Here, $\hat{H}_1$ is composed of local operators acting on odd sites and their right neighbours, and $\hat{H}_2$ is composed of local operators acting on even sites and their right neighbours.

This simplification allows us to approximate the time evolution operator by exploiting the first order Trotter decomposition of the exponential operator:

$$e^{O_1+O_2} = \lim_{n\to\infty} \left(e^{\frac{O_1}{n}} e^{\frac{O_2}{n}}\right)^n . \tag{5.8}$$

Taking $t = n \cdot dt$, we may write the unitary time operator as:

$$e^{(-\mathrm{i}t\hat{H})} = e^{(-\mathrm{i}t\hat{H}_1)+(-\mathrm{i}t\hat{H}_2)} = \lim_{n\to\infty} \left(e^{-\mathrm{i}dt\hat{H}_1} \cdot e^{-\mathrm{i}dt\hat{H}_2}\right)^n . \tag{5.9}$$

It can be shown [50] that Eq. (5.9) is equivalent to:

$$e^{(-\mathrm{i}dt\hat{H}_1)+(-\mathrm{i}dt\hat{H}_1)} = e^{(-\mathrm{i}dt\hat{H}_1)} \cdot e^{(-\mathrm{i}dt\hat{H}_1)} + \mathcal{O}(dt^2). \tag{5.10}$$

Therefore, by choosing a small enough dt, we can approximate:

$$e^{-\mathrm{i}dt\hat{H}} \approx e^{(-\mathrm{i}dt\hat{H}_1)} \cdot e^{(-\mathrm{i}dt\hat{H}_1)}. \tag{5.11}$$

Thus, evolving a density matrix for one time step dt for the first-order Trotter decomposition is given with:

$$\hat{\rho}(t_0 + dt) = e^{-\mathrm{i}dt\hat{H}_1} \cdot e^{-\mathrm{i}dt\hat{H}_2}\ \hat{\rho}(t_0)\ (e^{-\mathrm{i}dt\hat{H}_1} \cdot e^{-\mathrm{i}dt\hat{H}_2})^{\dagger}. \tag{5.12}$$

The operation in Eq. (5.12) is depicted in Fig. 5.4.

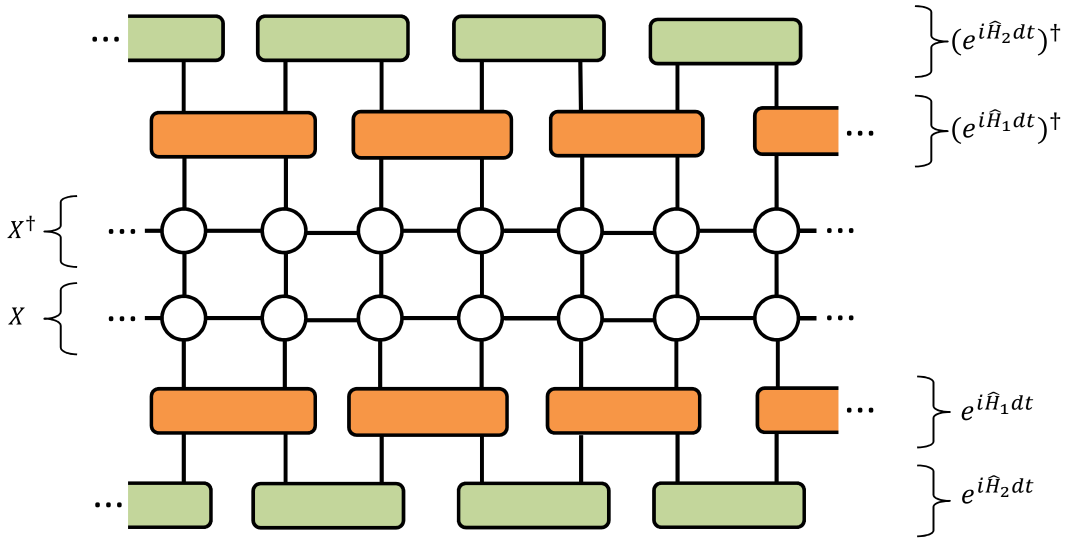

Figure 5.4: One time-step dt iteration in the density matrix time evolution for the first-order Trotter decomposition.

We evolve the density matrix operator to the time $t = ndt$ by applying the approximated time evolution operator from Eq. (5.11) consecutively n times.

Back to the temperature evolution, performing n time steps of size dt is equivalent to cooling down the density matrix to the temperature:

$$T = \frac{1}{2\ n\ dt}. \tag{5.13}$$

Throughout the imaginary time evolution procedure, the time step is not fixed to a constant value. This is due to the fact that the substitution mapping time to temperature is not linear in dt, hence one has to constantly adapt the time step in order to reach the points in the arbitrarily defined temperature grid. To keep the error within control, we fix the maximal allowed time step dt.

We point out that, while the exponent in the real-time evolution is imaginary and keeps the norm constant throughout the iterations, the exponent in the imaginary time evolution is real, thus the density matrix needs to be renormalized after the application of every two-site propagator.

There are two types of errors present during the imaginary time evolution. The first error comes from the Trotter decomposition and the discretization of the time grid. The second error is the consequence of the SVD truncation over the legs between the sites, performed in each time step in order to keep the tensor dimension reasonably low. We choose the maximal bond dimension m_{LPTN} so that only the first m_{LPTN} largest singular values are kept during the truncation. Therefore, the time step dt and the maximal bond dimension m_{LPTN} are the two parameters controlling the accuracy of the imaginary time evolution method.

5.2.2 LPTN to TTN conversion

With the imaginary time evolution we obtain the LPTN density matrix. However, for measuring the entanglement properties, we need our density matrix in the TTO form for computing the entanglement measures. In Chapter 4, we have shown how the state vector and a matrix version of the density matrix operator can be converted into different TN forms. Of course, by combining the elementary tensor transformations, we can also cross between the TN forms. In this section, we demonstrate how to convert a density matrix from the LPTN to the TTO form.

The conversion steps on example of $N = 4$ are shown in Fig. 5.5. Again, it is sufficient to work with only one side of the LPTN (or TTO), because the other one is simply the Hermitian conjugate. First, as in Fig. 5.5a we divide the LPTN's tensors in pairs and contract over the inner link between the paired tensors. Green dashed rectangles denote the tensors which are contracted. Then, we fuse each of the tensors' legs to obtain a matrix. Lower legs go to one matrix leg, and connecting link and upper legs go to the other leg, as indicated with the red dashed line in Fig. 5.5b. Next, we perform the SVD on each of the matrices and truncate the bond dimensions, split all of the legs, and obtain a TN in Fig. 5.5c. The lower tensors represent the bottom layer of the TTO. To create a base for building the next layer, we reshape all of the upper tensors into matrices again as indicated with the red dashed line, so that lower leg and connecting link belong to one matrix leg, and the upper legs belong to the other one. We SVD such reshaped matrices, truncate the bond dimensions, and arrive to the form depicted in Fig. 5.5d. We multiply the diagonal matrix with the lower tensors. By definition of SVD, the upper matrix is unitary. Since the total density matrix contains as well the Hermitian conjugate part contracted over the upper bonds, we can ignore these upper unitary matrices because they will contract with its Hermitian conjugate and yield the identity matrix. Therefore, we obtain the TN form on the Fig. 5.5e. The obtained tensors on upper layer in Fig. 5.5e have a form of an LPTN of a half as many particles. Therefore, we iterate the procedure to build the rest of the TTO layers and obtain Fig. 5.5f.

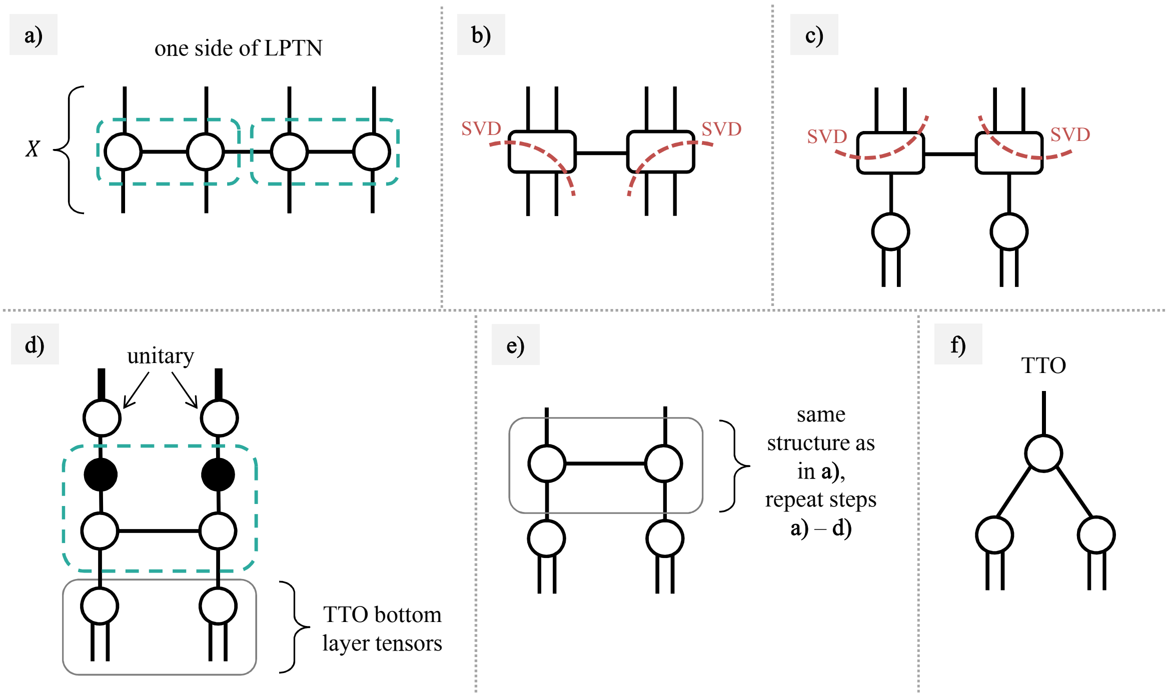

Figure 5.5: Conversion from locally purified tensor network to tree tensor network for the example of $N = 4$ physical sites. Green dashed rectangles denote the contraction of the enclosed tensors. Red dashed line defines reshaping of tensor into matrix: the tensor legs above the red dashed line are fused into one matrix leg, and the tensor legs below the red dashed line are fused into the other matrix leg.

The error introduced in the LPTN to the TTO conversion procedure depends on maximal bond dimension m_{TTO} chosen for the SVD truncations performed during the conversion. The different choices of m_{LPTN} and m_{TTO}, and their impact on the results, are discussed in Chapter 6.

5.3 *Measuring the density matrix properties*

Now one may ask, what is the practical advantage of the TTO density matrix in comparison to the LPTN? The answer is in the combination of the two TTO benefits- the middle connecting link and the root tensor as the isometry center.

The first point was already discussed in Chapter 4. A TTO density matrix contains the connecting link representing the sum over the states and corresponding probabilities in the density matrix (recall Fig. 4.18). In a general case, as the sum goes over a complete set of states, the connecting link dimension grows exponentially with the system size, $K_0 = d^N$. This is a drawback, as the initial idea of the TNM is to avoid working with the objects of the exponentially scaling dimensions. However, in the finite temperature systems, the probabilities decay exponentially with the state's energy. Therefore, TTO form allows us to directly gain the algorithm efficiency in the low-temperature range by discarding the high energy states, making the finite temperature simulations possible.

The second point is discussed in the following section, where the concept of the isometry center is introduced. For the sake of simplicity, we do not go through all the technical procedures of installing and shifting the isometry center in TN, but rather explain the main idea and discuss the simplifications that follow (for more details, see e.g. [51]).

5.3.1 Isometry center

Before providing the definition of the isometry center, it is useful to discuss the operation of trace in the TN context. Mathematically, trace of an arbitrary matrix **A** is defined as:

$$\mathrm{Tr}(A) = \sum_n A_{nn}. \tag{5.14}$$

To get the TN operator in any form, the matrix structure is expanded, and the original indices of the matrix are split into the multiple indices, each of them corresponding to a physical site. The generalization of the trace operation on the arbitrary TN operator form is thus defined as the contraction over all of the free indices belonging to the same physical site. The trace operation for the LPTN and TTO form is shown in Fig. 5.6.

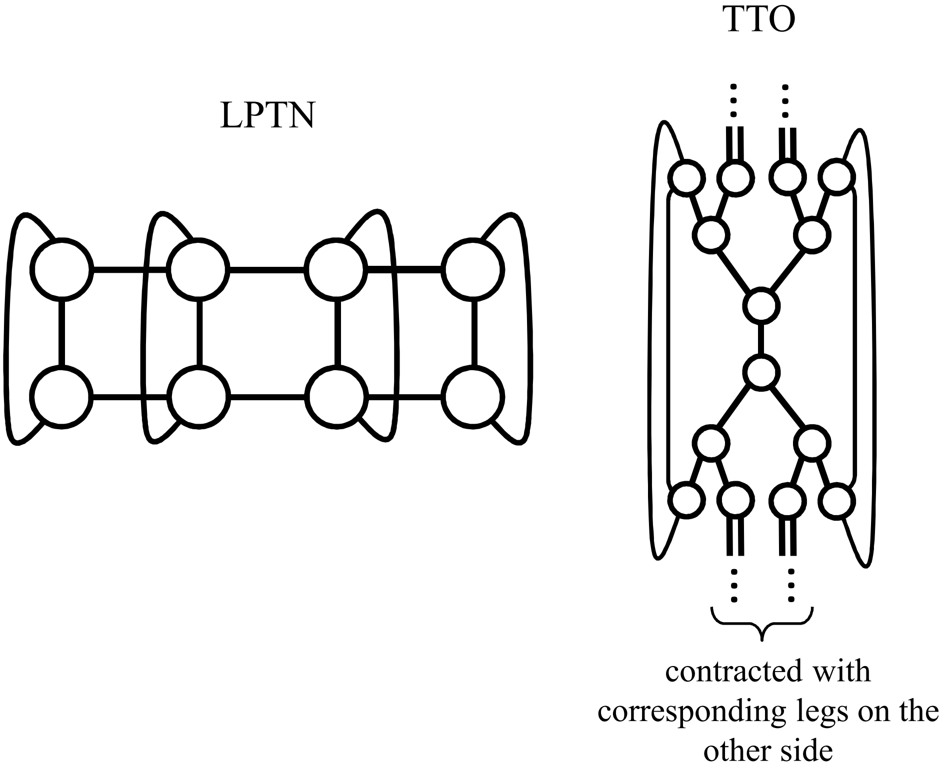

Figure 5.6: Trace operation in the cases of locally purified tensor network (left) and tree tensor network (right). The trace operation corresponds to contracting the free indices which belong to the same physical sites.

Now, we take a look at the following scenario: in each side of the TN operator, all of the tensors in a TN are unitary, except one. The term *unitary tensor* is here used as the extension of the concept of the unitary matrix. A unitary matrix $\mathcal{U}$ is the matrix with a property $\mathcal{U}\mathcal{U}^\dagger = \mathcal{U}^\dagger\mathcal{U} = \mathbb{1}$. The unitary tensor U is the one for which it holds:

$$\begin{aligned} \sum_{\beta 1\beta_2\dots} U_{\alpha_1\alpha_2\dots\beta_1\beta_2\dots}(U_{\beta_1\beta_2\dots\gamma_1\gamma_2\dots})^* =& I_{\alpha_1\alpha_2\dots\gamma_1\gamma_2\dots}, \\ \text{such that} \quad I_{\alpha\gamma} =& \mathbb{1}, \end{aligned} \tag{5.15}$$

where α and γ denote the fused indices $\alpha_1\alpha_2\dots$ and $\gamma_1\gamma_2\dots$ respectively. Therefore, a tensor is unitary if his corresponding matrix is unitary (Fig. 5.7). Note that, given a tensor with multiple legs, there are multiple ways of combining the legs into the matrix. Matrix and the unitary tensor refers always to one specific bipartition of legs.

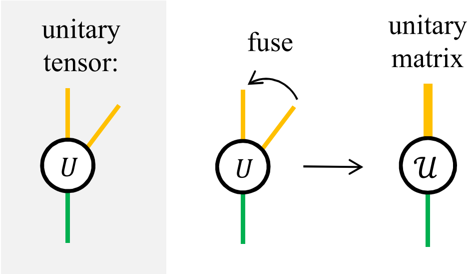

Figure 5.7: Unitary tensor and unitary matrix correspondence. Although the tensor legs can be combined into the matrix in multiple ways, the tensor is unitary over the one specific bipartition of legs.

Back to the TN operator, suppose we have an LPTN where all but one tensor (per side) are unitary in a way that a free leg of each of the tensors belongs to one matrix leg, and the rest belong to the other one (5.8a). Since the two sides of the LPTN are Hermitian conjugates of each other, performing a trace over such operator is trivial, as the contractions over all the unitaries yield the identity matrix (Fig. 5.8b). The only operation which needs to be computed is thus the contraction over the two remaining non-unitary tensors (Fig. 5.8c).

When a TN operator has all but one (or two, if we are talking about both sides of the operator) unitary tensors, such that when traced out each of them cancels out with its Hermitian conjugate into the identity, we say that the TN is *isometrized*. The non-unitary tensor is called the *isometry center*.

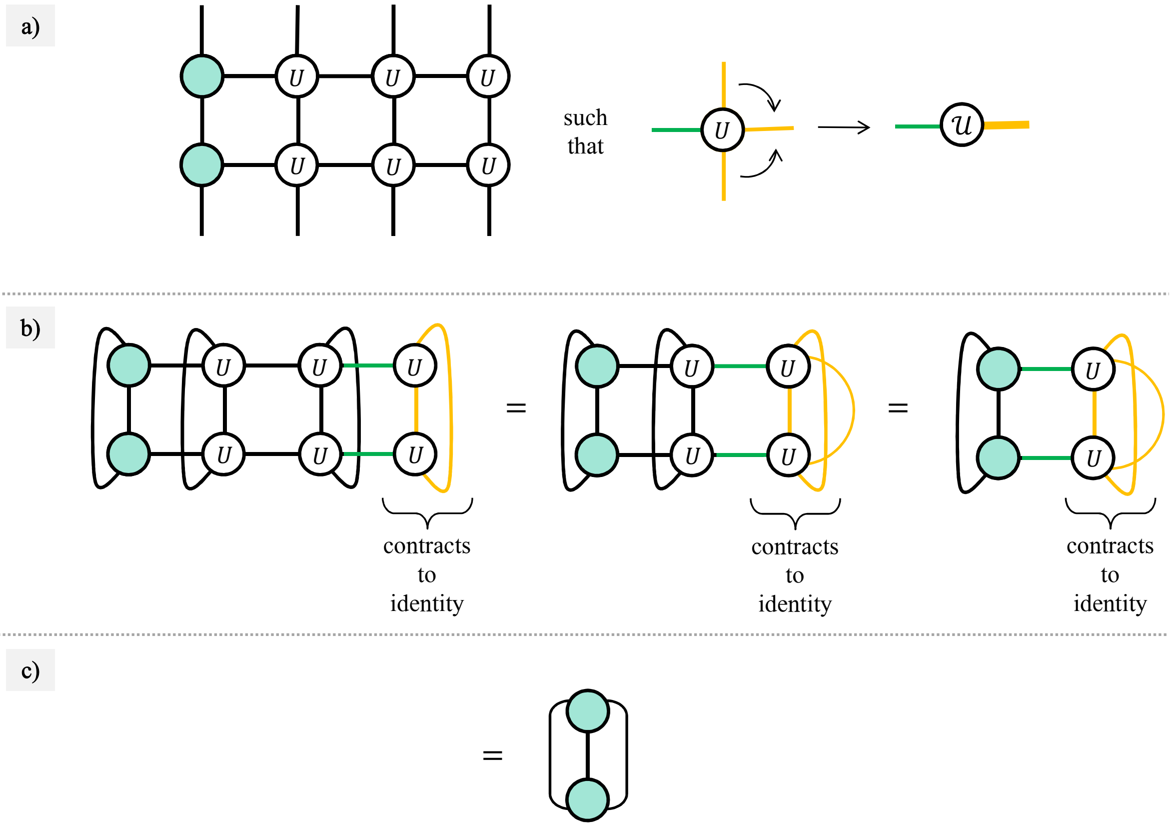

Figure 5.8: Trace operation of the isometrised locally purified tensor network. The isometry center, i.e. non-unitary tensor, is represented with a blue circle. The green and yellow color of the tensor legs indicate the bipartition of legs which yields the unitary matrix. Performing a trace reduces to contracting the isometry center tensors.

At first sight it may seem that isometrised TN is a very specific, rare scenario. However, there is a way of manipulating a TN so that the isometry center is installed exactly at the position we want. To do so, we exploit either SVD or the QR decomposition of the matrix:

$$A = QR, \tag{5.16}$$

where **Q** is unitary, and **R** is upper triangular. On the Fig. 5.9, it is shown now how to install the isometry center between the two tensors. With the same trick, we can install or shift the isometry center of the more complex TNs with the arbitrary number of sites.

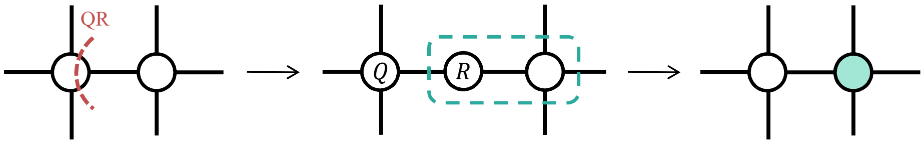

Figure 5.9: Installing the isometry center between the two tensors by performing the QR decomposition. The installed isometry center is represented with a blue circle.

Having an isometrized TN yields some major simplifications. What can be shown is that performing the SVD truncation over the isometry center preserves the most information about the system as possible. This means that, in order to introduce the smallest possible error when truncating, we can shift the isometry center to the tensor over which we are performing the SVD.

Using the fact that the TN conversions are based on SVD decompositions, where resulting matrices **S** and **D** are unitaries, the LPTN to TTO conversion described in Section 5.2.2 is constructed in a way that a resulting TTO contains the isometry center positioned in the uppermost tensor. The uppermost tensor is further reffered to as the root tensor. Having the isometry center in the root tensor is convenient for multiple reasons. First, it enables the efficient extraction of the mixed state probabilities. For any density matrix in a matrix form, the mixed state probabilities represent its eigenvalues. In a similar way, the mixed state probabilities can be extracted from the TTO. It can be shown that, if the root tensor is an isometry center, the singular values of root tensor's matrix form correspond to the square root of the probabilities. Moreover, all of the properties we compute in this thesis can be extracted directly from a root tensor (we show this on the example of EoF in the next section). Therefore, we effectively reduced handling the entire TTO by concentrating the important information into one tensor of controllable dimensions.

5.3.2 Entanglement of formation computation

In this section, we explain the technique used to estimate the EoF of a given TTO density matrix [30]. As defined in Section 3.4.2, the EoF represents the minimal value of the weighted sum over the pure state entanglement entropies, minimized over all possible decompositions of $\hat{\rho}$:

$$E_F(\hat{\rho}) = \inf_{\psi_j, p_j} \Big\{ \sum_j p_j \mathcal{S}_E(|\psi_j\rangle) \quad : \quad \hat{\rho} = \sum_j p_j \left|\psi_j\right\rangle \left\langle\psi_j\right| \Big\}. \tag{5.17}$$

EoF is a bipartite entanglement measure, and in this thesis we are concerned with the entanglement between the two halves of the particle chain.

A set of the possible decompositions over the discrete ensemble of states can be obtained from a set of semi-unitary matrix $\mathcal{U}^{K_0 \times K}$, $K \geq K_0$. An arbitrary decomposition is given with [52]:

$$\hat{\rho}' = \hat{\rho}\,\mathcal{U}. \tag{5.18}$$

Recalling the Section 4.3, a density matrix can be rewritten as:

$$\hat{\rho} = XX^{\dagger}, \quad X = \sum_j \sqrt{p_j}, \left|\psi_j\right\rangle \left\langle j\right|, \tag{5.19}$$

and X represents one side of the TTO. Thus, Eq. (5.17) can be recast as:

$$E_F(R) = \min_{K \geq K_0} \inf_{\mathcal{U}} \Big\{ \sum_j p'_j \mathcal{S}_E(|\psi'_j\rangle) \quad : \quad X' = X\mathcal{U} \Big\}. \tag{5.20}$$

The normalized columns of X' represent the new pure states:

$$|\psi'_j\rangle = \frac{1}{\sqrt{p'_j}} X' \left|j\right\rangle, \tag{5.21}$$

where $p'_j = \langle j|\, X'^{\dagger} X' \,|j\rangle$ are the new probabilities.

Our TTO density matrix is isometrized, with the isometry center positioned at the root tensor. In this case, the matrix X in Eq. (5.19) can be replaced with the matrix form of the root tensor R, and we justify this statement by considering the following: the EoF depends on the entanglement entropy of the columns of X (or any X'). The entanglement entropy, $\mathcal{S}_E = \mathcal{S}(\hat{\rho}_A)$, depends on the reduced density matrix, A being one half of the system. Reduced density matrix $\hat{\rho}_A$ implies tracing out the density matrix over the other half of the system. In the TTO language, tracing over half of the system implies contracting over half of the free links (Fig. 5.10 left). Since all tensors, except the root one, are unitary, a TTO reduces to the TN in Fig. 5.10 right. Now, we look at the definition of the Von Neumann entropy, $\mathcal{S}(\hat{\rho}_A) = \mathrm{Tr}(\hat{\rho}_A \log \hat{\rho}_A)$. As the logarithm of the matrix is given by its Taylor expansion, the Von Neumann entropy is obtained by tracing out the sum of powers of $\hat{\rho}_A$. Therefore, as depicted in Fig 5.11 on the example of $\mathrm{Tr}(\hat{\rho}_A^2)$, all of the unitary tensors again cancel out to the identities, allowing us to work only with the root tensor. The generalization of operation in Fig 5.11 to the higher powers of $\hat{\rho}_A$ is straightforward. In the computation of the EoF, we can thus replace the matrix X with the matrix form of the root tensor R. Another way to prove this statement is by noticing that contractions of unitary tensors with the root tensor represent the unitary transformations. Since unitary transformations are LOCC operations, they cannot change the entanglement, and therefore, we can compute all the entanglement information only from the root tensor.

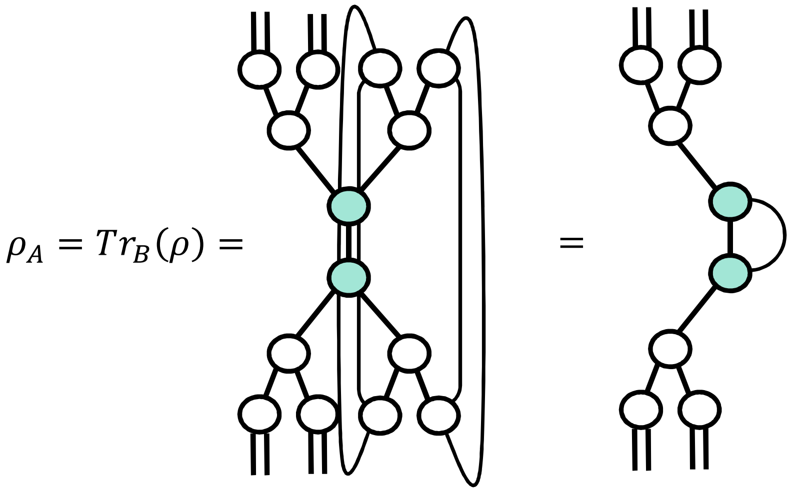

Figure 5.10: Obtaining the reduced density matrix of one half of the system in the tree tensor operator representation. The isometry center is positioned in the root tensor and is represented with a blue circle.

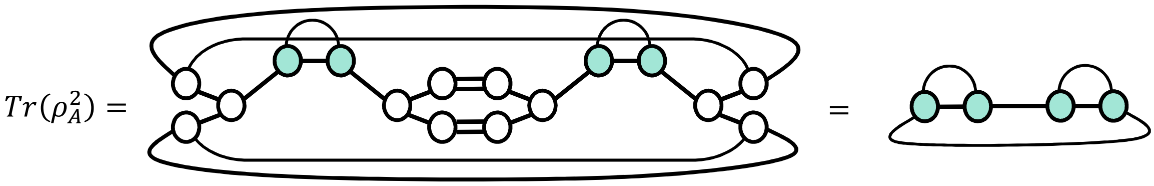

Figure 5.11: Computing the square of the reduced density matrix in the tree tensor operator representation. The isometry center is positioned in the root tensor and is represented with a blue circle. The operation reduces to contracting over the isometry centers.

To perform the minimization in Eq. (5.20), we need to evaluate the decomposition over different unitary matrices. We obtain the set of $K_0 \times K$ unitary matrices by parametrizing the $K \times K$ Hermitian matrix, $M = M^\dagger$. The corresponding $K \times K$ unitary matrix is obtained as $\mathcal{U}_M^{K\times K} = e^{iM}$. To get the $\mathcal{U}^{K_0\times K}$, we simply take random K_0 rows of $\mathcal{U}^{K\times K}$ and keep them fixed for the following optimization iterations. Once we have $\mathcal{U}^{K_0\times K}$, we apply it to the root tensor to obtain R'. However, even taking $K = K_0$ is shown to be enough to achieve a very good estimate for the EoF (see the supplemental material in [30]). Therefore, for the simplicity, we use $K = K_0$ in our simulations. After obtaining R', we find the new probabilities p'_j and use them to renormalize the columns of R'. The renormalized columns represent the new pure states $|\psi'_j\rangle$, and for each of them, we compute the entanglement entropy. The minimization over all decompositions is performed by using the Nelder-Mead solver implemented within the SCIPY library.

Similarly to the example of EoF, it can be proved that computing the other properties as well can be simplified to working only with the root tensor. In this thesis, we implement the functions for computing purity, Von Neumann entropy, Rényi entropy, negativity and EoF from the TTO density matrix. Apart from the EoF, which requires the additional effort for the minimization, the purity (Eq. (2.12)), Von Neumann entropy (Eq. (3.10)), and Rényi entropies (Eq. (3.14)) are computed directly using the thermal probabilities, where the thermal probabilities are equal to the root tensor's singular values squared. The negativity is obtained by its definition in Eq. (3.28), replacing the X matrix with R.

6 Physical models

This Chapter is dedicated to the results of our numerical method, tested on two one-dimensional physical models - the quantum Ising model and Rydberg atom model. We simulate the systems of $N = 8$, 16, and 32 particles. While obtaining the density matrix in the case of $N = 8$ is still possible via the exact diagonalization of the Hamiltonian, computing the $N = 16$ exact density matrix is computationally extremely expensive and requires large-scale computational resources. For $N = 32$ particles, the exact density matrix computation is out of scope for any method or HPC system.

In this thesis, we compute the density matrix using the method described in Section 5.2, and use it to compute the purity, Von Neumann entropy, Rényi entropies, negativity, and EoF. All the simulations were run on Cineca's Marconi100 HPC cluster. In order to gain an insight to the qualitative energy spectrum properties of the Ising and Rydberg atom physical models, we exactly diagonalize the $N = 8$ Hamiltonian.

6.1 Ising model

Ising model is a well-known model describing the ferromagnetic and paramagnetic behaviour of the locally interacting quantum spins in external magnetic field. The model was first introduced by W. Lenz [53] in 1920, who proposed it as a theoretical problem to his student E. Ising. Ising [54] analytically examined the one-dimensional case within his PhD thesis and proved there was no classical phase transition present at any temperature. His discovery lead him to generalize the conclusion and to state that the model does not exhibit classical phase transitions even in the higher-dimensional cases. This incorrect induction suppressed the research on Ising model for the next two decades. However, a big breakthrough happened in 1944, when Onsager [55] published his analytical calculations on the square lattice case, proving the existence of the finite temperature order-disorder phase transition in two dimensions. Since then, the Ising model has become one of the most thoroughly examined quantum many-body models.

Nevertheless, even the one-dimensional case of the model is interesting to study, as it manifests a different kind of phase transition - the quantum phase transition. Similarly to a classical phase transition, where a small change of the parameter, such as temperature, induces a sudden change of the system's properties, a quantum phase transition implies that a small variation of the parameter results in a drastic change of the ground state properties.

In this thesis, we consider the nearest-neighbour quantum Ising model with the open boundary conditions described with the Hamiltonian:

$$\hat{H} = -J\Big(\sum_{i=1}^{N-1} \sigma_x^i \sigma_x^{i+1} + \lambda \sum_{i=1}^{N} \sigma_z^i\Big). \tag{6.1}$$

The Hamiltonian consists of two terms: the product of Pauli matrices $\sigma_x^i \sigma_x^{i+1}$, which describes the dipole-dipole interparticle interactions, and the local term σ_z^i, which represents the interaction with the external field. The trade-off between the two contributions is parametrized with the parameter λ, which plays a role of the external field strength. The parameter J defines the Hamiltonian energyscale.

6.1.1 Energy spectrum properties

Observing the Hamiltonian in Eq. (6.1), one can predict the existence of two regimes in the Ising model. On the one hand, for the weak external field, the leading contribution is the interacting part, and we expect the system to favour the alignment of nearest-neighbour spins in the same direction along the x-axis. On the other hand, when the external field is strong, we expect it to align the spins along the z-axis.

The two regimes can indeed be observed in the system's energy spectrum and, as we show shortly, they represent the two distinguishable quantum phases. The energy spectrum with 50 lowest eigenenergies plotted for three different λ for a system of $N = 8$ particles is shown in Fig 6.1. The spectrum was obtained by the exact Hamiltonian matrix diagonalization using Python.

We consider the zero-temperature case first. At the zero temperature, the system is in the ground state. The energy gap between the first two energy levels as a function of parameter λ is plotted for different system sizes in Fig. 6.2 left. We can see that, for $\lambda \ll 1$, the ground state is degenerate. The right plot on Fig. 6.2 shows the first three energy levels divided by the ground state energy, and it reveals that the ground state is two-fold degenerate in the limit $\lambda \ll 1$. The two states correspond to the superpositions of the states with all the spins aligned along each of the two directions of the x-axis. Since the spin alignment is a consequence of the interparticle interactions, the system is in the ferromagnetic phase. Around $\lambda \approx 1$, the ground state symmetry breaking occurs, and the system passes through a quantum phase transition from a ferromagnetic to a paramagnetic phase. We refer to a phase as paramagnetic when a system is polarized, with all spins aligned in the same direction. For the Ising model, a paramagnetic phase occurs in the case of strong external field λ, where the ground state corresponds to a system with all spins aligned in the z-direction. In the thermodynamical limit, the quantum phase transition occurs at exactly $\lambda = 1$. In the left frame of Fig. 6.2, we observe that as the system size increases, the ground state degeneracy breaking shifts towards $\lambda = 1$.

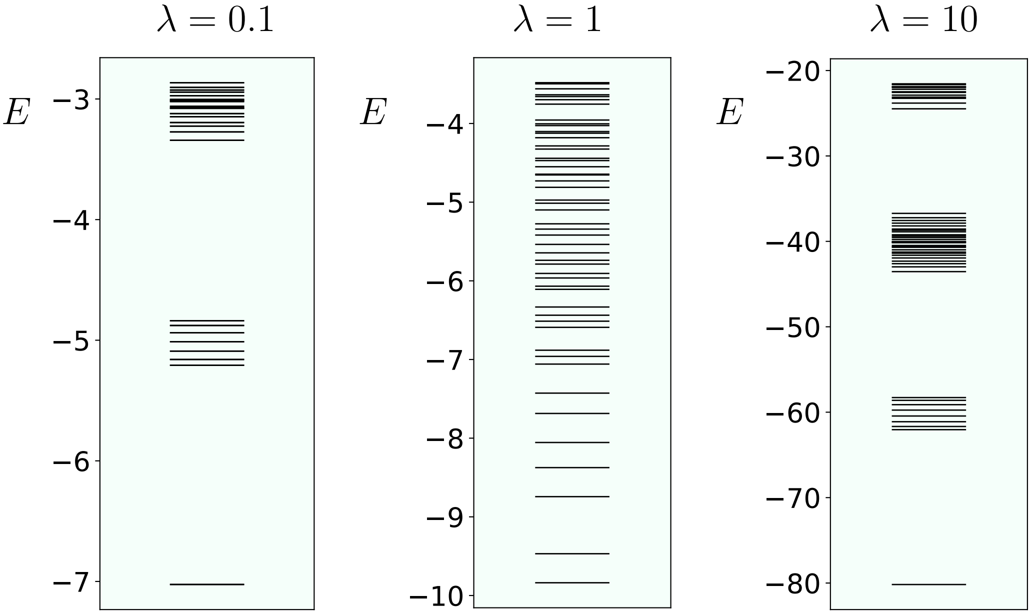

Figure 6.1: Energy spectrum of $N = 8$ particle Ising model for $\lambda = 0.1$ (left), $\lambda = 1$ (middle), and $\lambda = 10$ (right). The first 50 energy states are plotted. Energy is expressed in the units of Hamiltonian energyscale J.

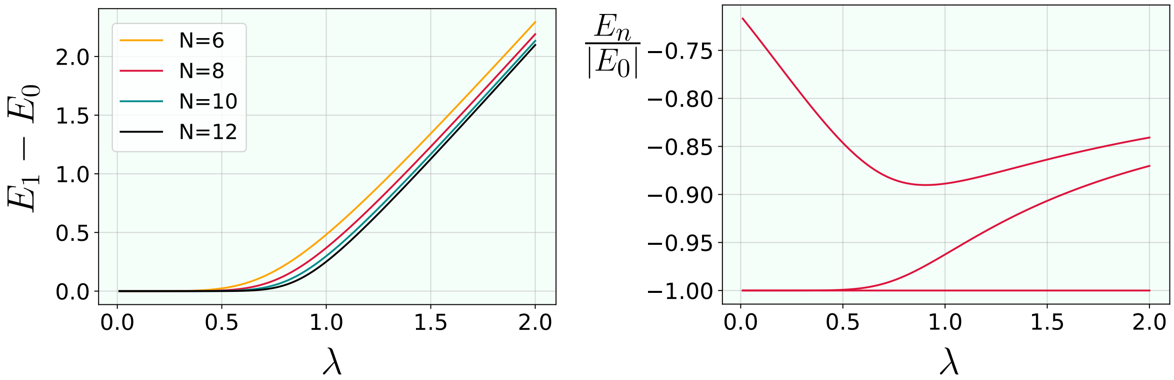

Figure 6.2: Left: the energy gap between the first two energy levels in the Ising model for different system sizes, plotted as a function of parameter λ. As the system size increases, the ground state degeneracy breaking shifts towards $\lambda = 1$. Right: the first three Ising model energy levels E_n divided by the ground state energy $|E_0|$, computed as a function of parameter λ for $N = 8$. Energy is expressed in the units of Hamiltonian energyscale J.

When the finite temperature is introduced to the system, the excited states start contributing to its density matrix, i.e. the system becomes a mixture. Therefore, in order to make predictions about the system's behaviour, the higher energy states need to be considered as well. Since our numerical algorithm's efficiency decreases with the number of contributing states, we focus on the low-temperature range.

The physical interpretation of the Ising model's low-energy states in the limits of the very small and very large λ are depicted in Fig 6.3 on the example $N = 3$. In the first excited state for the weak external field, there exists one pair in which the first-neighbour particles are oriented in the opposite directions along the x axis, leading to the existence of two spin domains. Since there are $N - 1$ positions in the chain at which this pair can be positioned and two possible directions along the x-axis, the first excited state is $2(N - 1)$-fold degenerate. Similarly, the next excited state corresponds to the chain in which the two nearest-neighbour spin pairs are aligned in the opposite directions. For the strong external field, the first excited state corresponds to the chain with all the spins aligned along the z-axis, except one. There are N possible positions at which the opposite oriented spin can be, and the external field direction defines the direction of his alignment with the z-axis. Therefore, the first excited state is N-fold degenerate. Analogously, the next excited state has two spins aligned in the opposite direction. The degeneracy of the states breaks as we approach the quantum critical point $\lambda = 1$ and, as seen in Fig. 6.1, the energy gaps are the smallest at $\lambda = 1$.

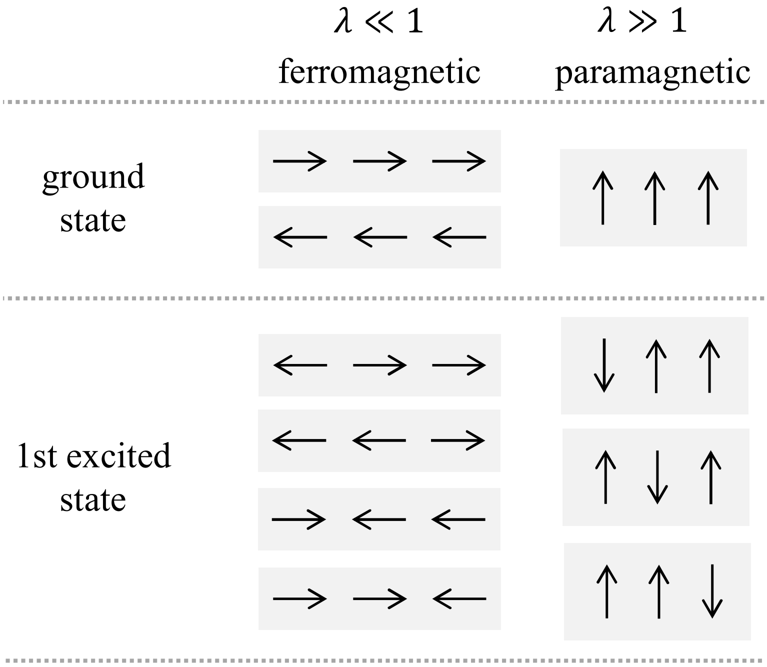

Figure 6.3: Physical interpretation of the ground and the first excited states of the Ising model for $N = 3$ particles. The alignment of the spins is indicated with the arrow. The direction of the x-axis is taken to be along the horizontal axis, and the direction of the z-axis is taken to be along the vertical axis.

Recalling the Eq. (5.1), the mixed state probabilities decay exponentially with the energy. Therefore, the gaps between the energy levels directly influence the probability distribution, and the system's ground state contribution is more robust with the temperature when there is a large gap between the ground state and the first excited state. As the gap closes, the probabilities of the ground and the first excited states become more similar. Quantitatively, the increase of the system's mixture with the increase of temperature is dictated with the ratio T/Δ, where Δ is the energy gap. Applied to the Ising model, by observing Fig. 6.1 we expect that increasing temperature will increase the system's degree of mixture most quickly around the critical point, as that is the point where the energy gap Δ between the ground and the first excited state is the smallest.

6.1.2 On the choice of convergence parameters

Before we present the results, we analyze how the accuracy of our method depends on the convergence parameters, temperature, and system size. As discussed in the previous chapter, the accuracy is controlled with the four convergence parameters:

the imaginary time evolution time step dt, maximal LPTN bond dimension m_{LPTN}, maximal TTO bond dimension m_{TTO} and the number of states kept in a density matrix, i.e., the TTO root tensor's link dimension K_0. In this chapter, we discuss the error introduced by m_{LPTN}, m_{TTO}, and K_0. Imaginary time evolution error is discussed in Appendix A.

We analyze the convergence of the results depending on the bond dimensions m_{LPTN}, m_{TTO} and K_0. Since, for large values of bond dimensions, the simulations become computationally very exhaustive, the balance between the satisfying accuracy and computational time had to be found. The values of the maximal bond dimensions chosen for the simulations are shown in Table 6.1.

	$N = 8$	$N = 16$	$N = 32$
m_{LPTN}	256	50	35
m_{TTO}	256	50	35
K_0	256	100	85

Table 6.1: Maximal bond dimensions used for the Ising model simulations.

The main operation limiting us from choosing a larger bond dimensions is the SVD in the LPTN to TTO conversion procedure, with the computational complexity $\leq \mathcal{O}(m_{LPTN}^2 m_{TTO}^6)$. This expression represents the upper bound because m_{LPTN} and m_{TTO} are the maximal bond dimensions, thus the tensor dimensions are not exactly determined, but only limited by the convergence parameters. The maximal tensor size allowed by m_{LPTN} and m_{TTO} is not necessarily reached through the LPTN to TTO conversion. In fact, examining the conversion procedure reveals that, in the range of system sizes we are working with, the maximal dimension of the tensor actually reached through the conversion grows with the number of particles. For this reason, the simulations of $N = 8$ and $N = 16$ particles have much shorter execution time in comparison to the $N = 32$ case. Therefore, smaller system sizes allow choosing larger maximal bond dimensions. For $N = 8$, we can choose the maximum possible values for the bond dimension, $m_{LPTN} = m_{TTO} = K_0 = 256$. This choice enables us to verify the accuracy of the imaginary time evolution algorithm. Since, for $N = 8$, there are no truncation errors introduced, only the error induced by the finite-sized time step dt is present. The analysis of the imaginary time evolution error is presented in Appendix A.

As the bond dimension K_0 is controlled in the final step of the LPTN to TTO conversion, it does not influence the computational time of obtaining the density matrix. However, as K_0 dictates the root tensor's dimension, it does effect the time required for computing the properties.

As a measure of accuracy of the results, we tracked the norm loss due to the SVD truncation during the LPTN to TTO conversion procedure. The results for the critical external field parameter value $\lambda_c = 1$ are shown in Fig. 6.4 for $N = 16$ case, and in Fig. 6.5 for $N = 32$. Each of the plots show the norm loss $|1 - \|\hat{\rho}\||$ for multiple values of a certain convergence parameter (left - m_{LPTN}, middle - m_{TTO}, right - K_0), while the remaining convergence parameters are kept constant, with the values indicated in Table 6.1. Moreover, in Fig. 6.6 the norm loss for $\lambda_c = 1$ is plotted as a function of temperature.

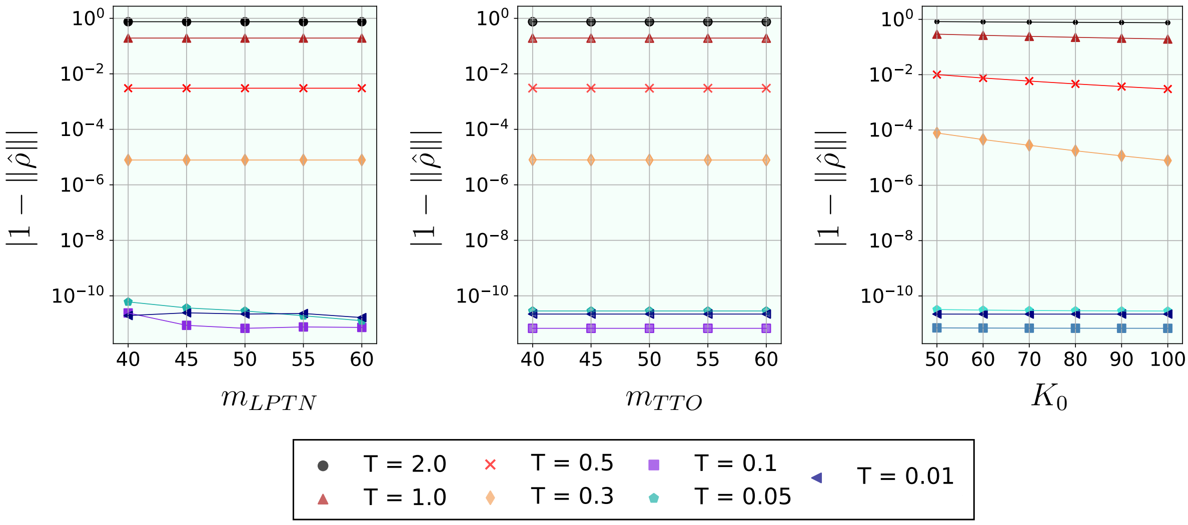

Figure 6.4: Density matrix norm loss $|1 - \|\hat{\rho}\||$ for Ising model with $N = 16$ particles, plotted as a function of one of the convergence parameters (left - m_{LPTN}, middle - m_{TTO}, right - K_0), while the remaining convergence parameters are kept constant, with the values $m_{LPTN} = 50$, $m_{TTO} = 50$, $K_0 = 100$. Different color curves correspond to different temperatures indicated in legend. Temperature T is expressed in units of J/k_B.

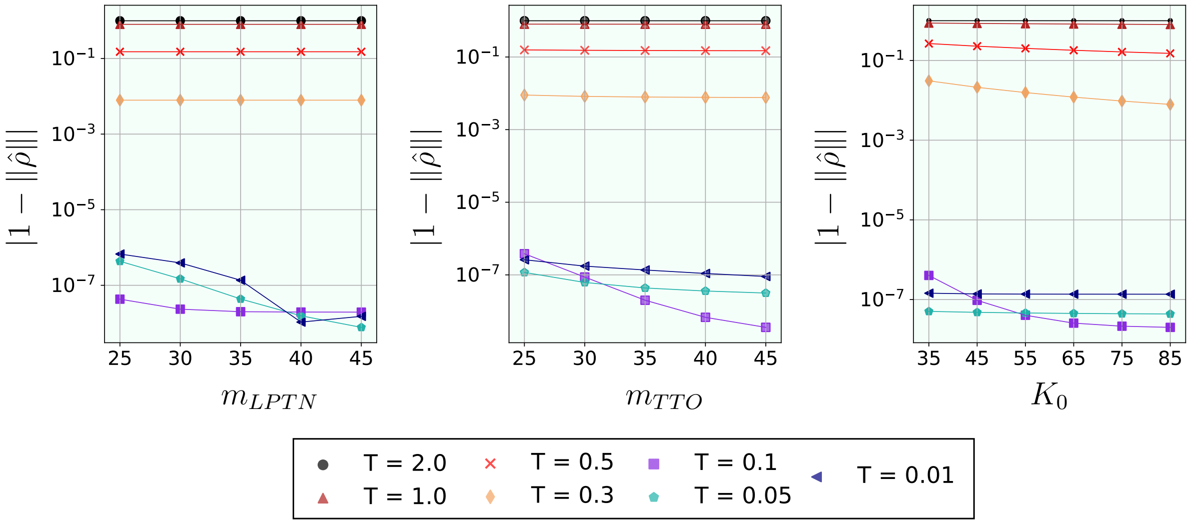

Figure 6.5: Density matrix norm loss $|1-\|\hat{\rho}\||$ for Ising model with $N = 32$ particles, plotted as a function of one of the convergence parameters (left - m_{LPTN}, middle - m_{TTO}, right - K_0), while the remaining convergence parameters are kept constant, with the values $m_{LPTN} = 35$, $m_{TTO} = 35$, $K_0 = 85$. Different color curves correspond to different temperatures indicated in legend. Temperature T is expressed in units of J/k_B.

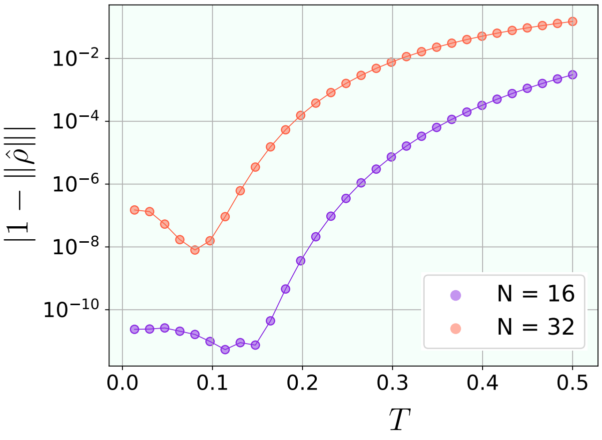

Figure 6.6: Density matrix norm loss $|1-\|\hat{\rho}\||$ for Ising model for $N = 16$ and $N = 32$ particles, plotted as a function of temperature T. The convergence parameters are chosen as indicated in Table 6.1. Temperature T is expressed in units of J/k_B.

First to notice in Figs. 6.4 to 6.6, the norm loss in most cases increases with increasing the temperature. This is, of course, expected, as larger temperature entails the larger number of excited states contributing to the density matrix, and the accuracy of our method depends directly on the number of states taken into account. Considering Fig. 6.6, we see that, at $\lambda_c = 1$, the norm loss is smaller than 10^{-2} up to the temperature of $T \approx 0.5$ for $N = 16$, and up to $T \approx 0.3$ for $N = 32$ (in units of the Hamiltonian energyscale, J/k_B). Therefore, we consider the results to be accurate for the temperatures below these values. Continuing on the discussion from the previous section, the temperature is expected to affect the results the most around the critical point, where the gap between the low-energy states is the smallest. Therefore, we expect the data in Fig. 6.4 and Fig. 6.5 to show the worst-case scenario for the accuracy of the results.

Next, from Fig. 6.4 and Fig. 6.5 we notice that the norm is changing with varying the K_0 bond dimension, and stays approximately constant throughout the variations of m_{LPTN} and m_{TTO}. This behaviour is, firstly, due to the relatively small range of the bond dimensions plotted. Taking a much smaller bond dimension would surely increase the norm loss. Secondly, the different bond dimensions have a different physical interpretation. K_0 is a parameter controlling the number of states in the density matrix, and therefore, it is reasonable that it influences the accuracy the most. We can notice that the effect of changing K_0 is the largest around $T = 0.3$. This is also expected because, on the one hand, in the lower temperature range, the probability to find the system in a ground state is large enough to discard the other states as negligible. On the other hand, in the higher temperature range, the equal contribution comes from a very large number of states, making each of their probabilities equally small, thus discarding or including five states less or more does not make a big difference. The bond dimensions restricted by m_{LPTN} and m_{TTO} represent the amount of entanglement in the system. Notice, for example, the middle plot on Fig 6.5. For the first three low temperatures the norm loss increases with decreasing the temperatures, regardless of the maximal bond dimension. This means we truncated more information in the lower temperature states, contradicting our previous assumption that the accuracy is dictated by the number of contributing states. However, the factor which is limited with the maximal bond dimension restriction in the low-temperature regime is not the number of contributing states, but the entanglement content. Therefore, the norm loss can be attributed to discarding the entanglement present in the system. As will be shown in the next section, the entanglement around the critical point decreases with temperature, therefore the error introduced by m_{LPTN} and m_{TTO} is larger at the point of the larger entanglement, i.e. the lower temperature. The same behaviour can be observed in Fig. 6.4, but the effect is smaller because the maximal bond dimensions are higher than in $N = 32$ case. The increasing norm loss due to the entanglement truncation for $T < 0.1$ can be observed in Fig. 6.6 as well. Altogether, we observe the two regimes in the norm loss: in the low temperature range, the norm loss occurs due to discarding the entanglement, while in the higher temperature range the norm loss occurs due to discarding the excited states in the density matrix.

6.1.3 Finite temperature properties

In this section, we present the results of our simulations for the Ising model. First, to qualitatively observe the finite temperature effects, we show the purity, entropy, and negativity in dependence of the external field λ and temperature T. Then, we focus on the critical point $\lambda_c = 1$ for which we compute the purity, negativity, entropy, Rényi entropy, and EoF.

Fig. 6.7 shows the $\lambda - T$ grid for the purity. Since purity directly tells us about the mixedness of the system, it gives us the information about the number of states contributing to the density matrix. Therefore, for the ferromagnetic phase, when the state is a mixture of the two degenerate ground states, the purity is $\gamma(\hat{\rho}) = 0.5^2 + 0.5^2 = 0.5$. In the paramagnetic phase, the state is pure, thus the purity is equal to 1. The two phases are clearly visible in Fig. 6.7. As predicted, the further the parameter λ is away from the critical point $\lambda_c = 1$, these phases stay more robust with temperature. In between the ferromagnetic and paramagnetic phase, we observe a disordered finite temperature phase.

Fig. 6.8 shows the $\lambda - T$ grid for the Von Neumann entropy. The same phases can again be distinguished, and the entropy increases as the system becomes more mixed. Fig. 6.9 shows the negativity, as a measure of entanglement. It can be observed that the entanglement is the largest around the critical point, and that it decreases with temperature. As the system size is increased, the entanglement becomes more concentrated toward the critical point at the zero temperature.

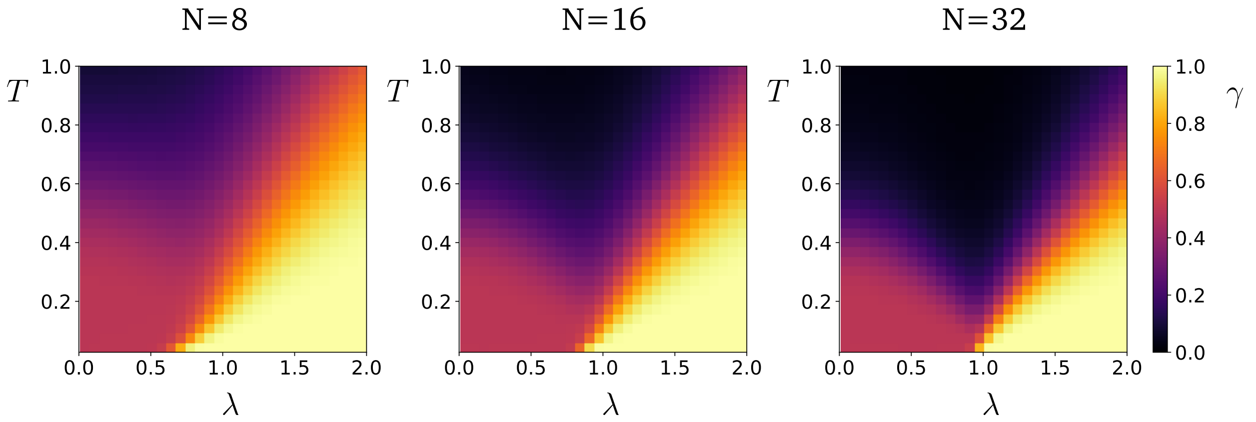

Figure 6.7: Purity γ for the Ising model as a function of parameter λ and temperature T, computed for different system sizes. Temperature T is expressed in units of J/k_B.

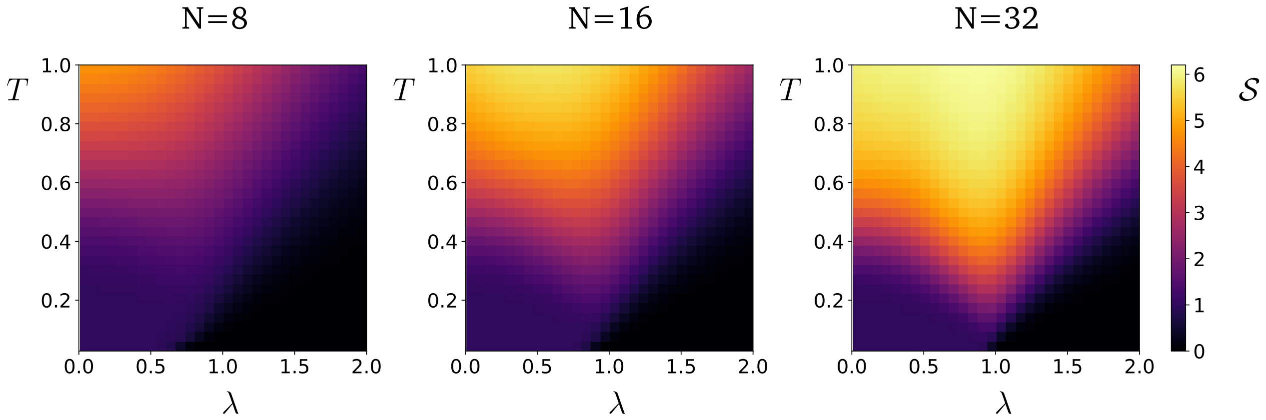

Figure 6.8: Von Neumann entropy $\mathcal{S}$ for the Ising model as a function of parameter λ and temperature T, computed for different system sizes. Temperature T is expressed in units of J/k_B.

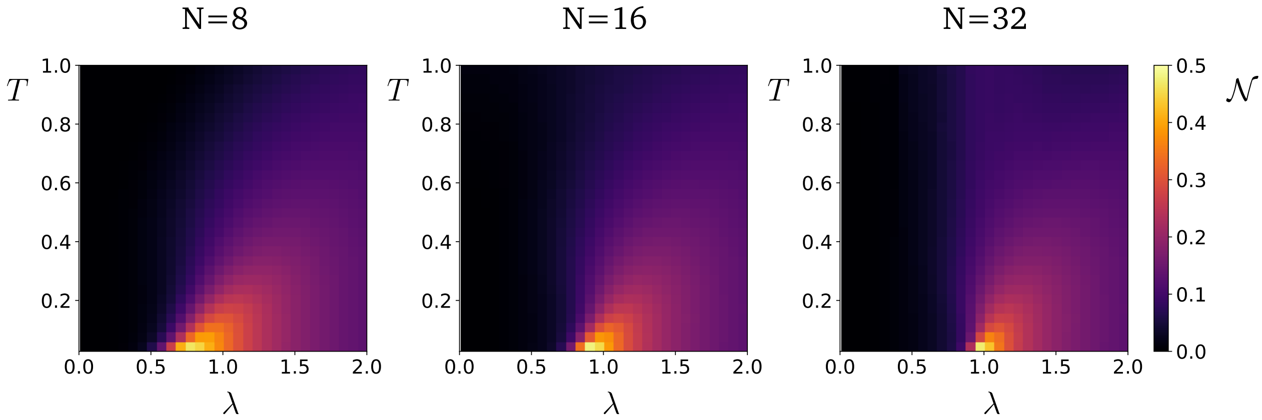

Figure 6.9: Negativity $\mathcal{N}$ for the Ising model as a function of parameter λ and temperature T, computed for different system sizes. Temperature T is expressed in units of J/k_B.

Another finite-effect observed is the change in the position of the critical point for different system sizes. As the system size increases, i.e. the system approaches the thermodynamical limit, the critical point moves towards $\lambda = 1$.

Note that, although the convergence analysis carried out in the previous section showed that the accurate results can be expected for the temperatures up to $T \approx 0.5$ for $N = 16$ and $T \approx 0.3$ for $N = 32$, the data computed for the higher temperatures is still a valuable insight to the qualitative description of the system's behaviour. Moreover, the accuracy is expected to be extended to a larger temperature range for external field parameter values away from the critical point.

Now, we focus to the critical point, as the point with the largest entanglement. Fig. 6.10 shows the purity computed for different system sizes. We see that, as the system size increases, the purity curve becomes steeper, i.e. the system is less robust with the temperature. The Von Neumann entropy is shown on Fig. 6.11 left, and the Von Neumann entropy scaled with system size is shown on Fig. 6.11 right. We observe the increase of Von Neumann entropy with the temperature, again with the steepest curve belonging to the system of the largest size. When scaled with system size, the Von Neumann entropies for different system sizes are aligned in the region $0.15 < T < 0.3$. The misalignment of $N = 8$ curve in the lower temperature range is expected to be due to the system size being far away from thermodynamical limit. Furthermore, we observe the increasing deviation of the $N = 32$ curve starting at approximately $T \approx 0.3$, which exactly coincides to the temperature point after which the truncation error becomes large.

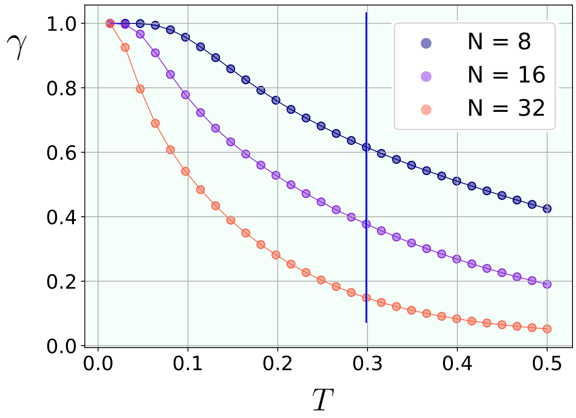

Figure 6.10: Purity γ for Ising model at the critical point $\lambda_c = 1$, computed as a function of temperature T for different system sizes. As a consequence of truncation error, for $N = 32$ we expect the accurate results up to $T \approx 0.3$, indicated with blue line. Temperature T is expressed in units of J/k_B.

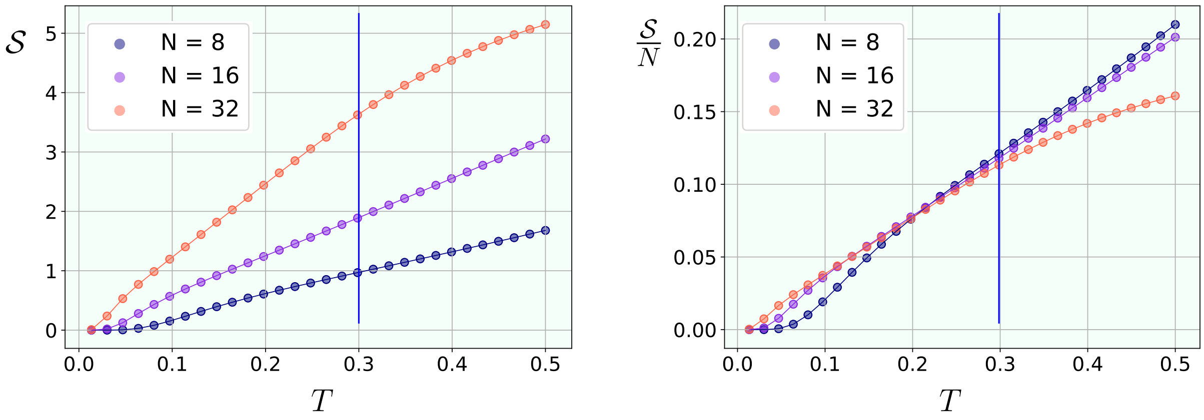

Figure 6.11: Von Neumann entropy $\mathcal{S}$ (left) and scaled Von Neumann entropy $\mathcal{S}/N$ (right) as a function of temperature T, computed for Ising model at the critical point $\lambda_c = 1$ for different system sizes. As a consequence of truncation error, for $N = 32$ we expect the accurate results up to $T \approx 0.3$, indicated with blue line. Temperature T is expressed in units of J/k_B.

The computed Rényi entropies for several values of α and different system sizes are shown in Fig. 6.12. The Von Neumann entropy is as well plotted in Fig. 6.12, to confirm that it coincides with the Rényi entropy in the limit $\alpha \longrightarrow 1$. Specifically in the case of $N = 32$ particles and $\alpha = 0.01$, we notice that Rényi entropy for $T < 0.1$ does not monotonically decrease. We expect this behaviour to be the consequence of error induced by the entanglement truncation, observed in same temperature range on Fig. 6.6.

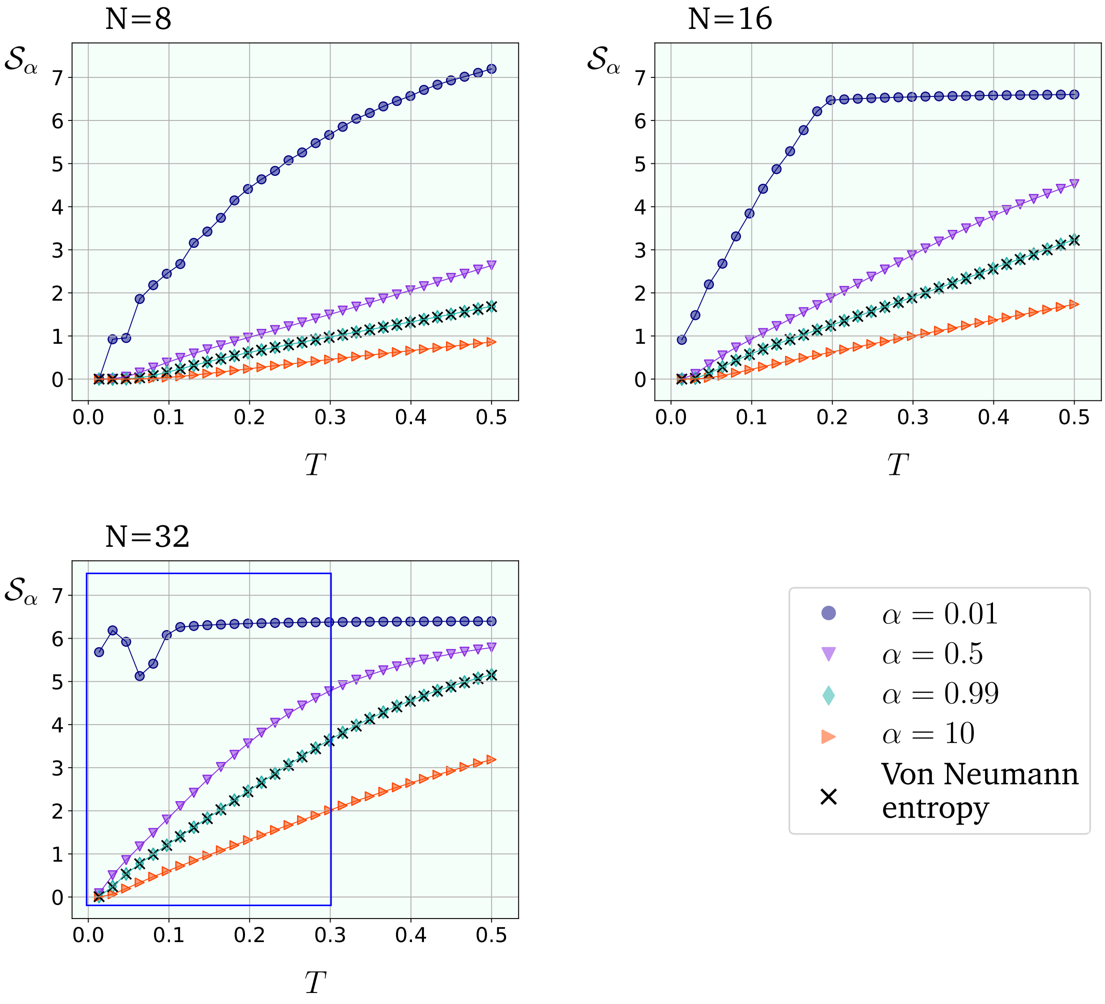

Figure 6.12: Rényi entropies S_α as a function of temperature T computed for Ising model for different values of parameter α. Data at the critical point $\lambda_c = 1$. Figures for system sizes $N = 8$ (up left), $N = 16$ (up right) and $N = 32$ (down left). In addition, the Von Neumann entropy is plotted to confirm the alignment with the Rényi entropy in the limit $\alpha \longrightarrow 1$. As a consequence of truncation error, for $N = 32$ we expect the accurate results up to $T \approx 0.3$, indicated with blue rectangle. Temperature T is expressed in units of J/k_B.

Furthermore, the computed entanglement measures are shown on Fig 6.13. The plot on the left corresponds to negativity, and the plot on the left corresponds to EoF. Since computing the entanglement of formation requires minimizing the expression in Eq. (5.20) over K_0^2 parameters, in order to reach the convergence of the solution, the K_0 bond dimension was further reduced. We reduced K_0 by setting its maximal value of 20 and further discarded all the finite temperature states $|\psi_j\rangle$ with corresponding probabilities p_j such that $p_j/p_0 < 10^{-4}$, p_0 being the ground state probability. Since restricting the density matrix to less than 20 states would introduce a large error in the region where $T > 0.1$, we computed the EoF for the low-temperature region, up to $T = 0.1$. To further improve the convergence, we performed the minimization using Nelder-Mead for 20 different random initial combinations of the input parameters, and kept the smallest obtained EoF value as the final result.

It is again possible to observe that the largest system is affected by the finite temperature the most. Moreover, both measures show that the entanglement at the temperature $T \approx 0$ increases with the system size. It should be mentioned that the comparison of the negativity and EoF serves as one of the checks of the code correctness - since they are the entanglement measures, if one state is less entangled than the other one, both negativity and EoF must show the decrease in value. In other words, if negativity monotonically decreases with temperature, the EoF must monotonically decrease as well. The monotonic decrease with the temperature is observed in both entanglement measures.

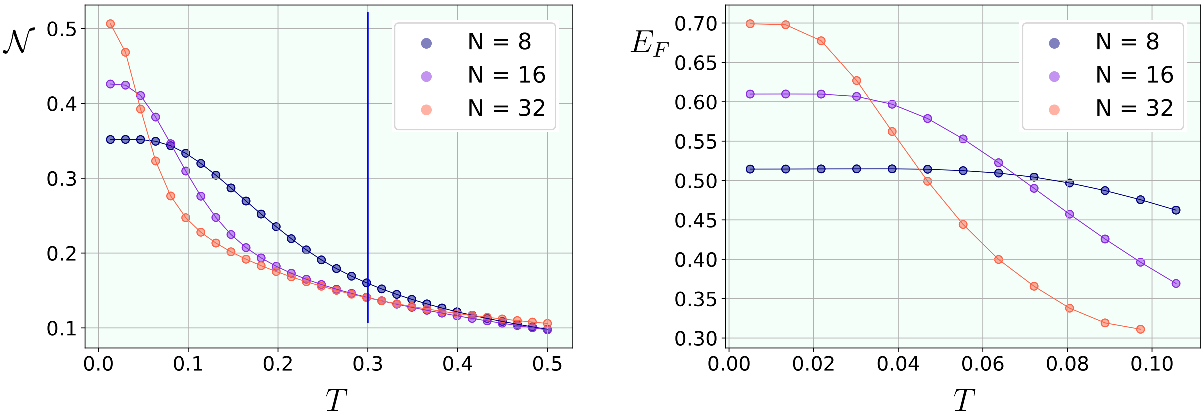

Figure 6.13: Negativity $\mathcal{N}$ (left) and entanglement of formation E_F (right), computed as a function of temperature T for different system sizes. As a consequence of truncation error, for $N = 32$ we expect the accurate results up to $T \approx 0.3$, indicated with blue line.

Moreover, we show that the low-temperature EoF follows the logarithmic conformal scaling law. For open boundary conditions, the appropriate scaling expression is [56]:

$$E_F(T, N) = \frac{c}{6} \log N + g(TN^z), \tag{6.2}$$

where c is the central charge, and z is a critical exponent. For critical Ising model $c = 1/2$ and $z = 1$. The scaling is shown on Fig. 6.14, and the alignment of the rescaled EoF values for different system sizes is clear.

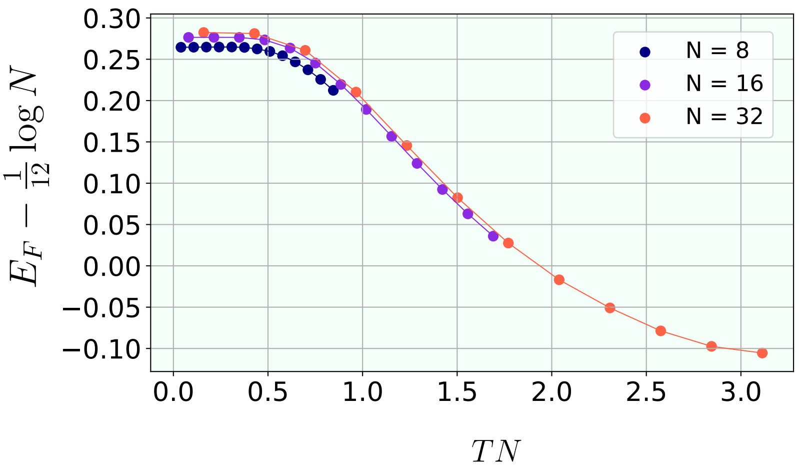

Figure 6.14: Scaling of entanglement of formation computed for Ising model at critical point $\lambda_c = 1$. The agreement is very good. Temperature T is expressed in units of J/k_B.

6.2 Rydberg atom systems

After analyzing the Ising model, we use our numerical method to examine the systems of neutral Rydberg atoms trapped in the optical tweezer arrays. We first provide a short overview of the Rydberg atom physics, and then motivate our interest in studying Rydberg atoms by introducing them in a context of quantum computing technologies. Furthermore, we present a way of modeling these systems by encoding the highly excited Rydberg state and the atomic ground state into the spin $1/2$ states.

6.2.1 Introduction to the Rydberg atoms

Rydberg atoms are highly excited neutral atoms with the principal quantum number $n \geq 10$. With one or more electrons excited in a high energy state very far from the atomic core, Rydberg atoms are huge - their diameter can be up to the μm order of magnitude, making them 10^4 times larger than the neutral atom in the ground state. As a consequence, they exhibit the exaggerated properties compared to the low-energy neutral atoms.

The property we are particularly interested in is the very strong dipole moment, scaling as n^2 [10], induced by an electron being very far away from the core. Of course, the existence of the dipole moment results in interparticle dipole-dipole interactions. The interaction potential is given with:

$$V_{dd} = \frac{e^2}{4\pi\varepsilon_0 R^3}\left(\vec{d_1}\vec{d_2} - \frac{3(\vec{d_1}\cdot\vec{R})(\vec{d_2}\cdot\vec{R})}{R^2}\right), \tag{6.3}$$

where $\vec{d_1}$ and $\vec{d_2}$ are the dipole moments of the atoms, and $\vec{R}$ is their relative coordinate. We can consider the two-atom transition channel $|ab\rangle \longrightarrow |rr\rangle$, where $|r\rangle$ is the Rydberg state and $|a\rangle$ and $|b\rangle$ are some intermediate atom states with the individual energies E_r, E_a, E_b, respectively. Analyzing the interaction potential, it can be shown [10, 70] that in the regime of the large energy difference $\delta = (E_r + E_r) - (E_a + E_b)$, the dipole-dipole interaction shifts the $|rr\rangle$ energy level for $\Delta E_{|rr\rangle} = C_6/R^6$, with the coefficient C_6 scaling as n^{11}. This dipole-dipole interaction corresponds to the Van der Waals interaction.

To summarize the above discussion, when the atoms are near each other, their dipole moments induce the mutually repulsive interactions, shifting the $|rr\rangle$ energy level upwards. The induced shift scales as $1/R^6$, with the multiplying coefficient scaling as n^{11}. Thus, having the two atoms in the excited Rydberg state very close to each other is energetically extremely unfavourable and effectively disabled. The described mechanism is called the Rydberg blockade, and it occurs within the certain blockade radius around the atom excited to the Rydberg state. Experiments have shown that the blockade radius can span to the several μm distance around the excited atom [13].

Since the Rydberg blockade prevents the excitation of the two spatially close atoms in the Rydberg state, by exciting the one atom to the Rydberg state, we in a way control the states of the other atoms. These controllable interactions are the key feature making Rydberg atoms good candidates for the physical realizations of qubits [59]. The appealing quality of the Rydberg atoms as a physical quantum computing platform is their scalability to the large system sizes. Since they are identical neutral atoms whose only interaction comes from the Van der Waals interactions, the simplicity of their structure enables us to pack a large number of neutral atoms on the precisely defined positions using optical tweezers [60, 61]. Rydberg atoms are easily experimentally manipulated with the external fields, and demonstrate the long coherence times, which can be exploited to realize the high-fidelity quantum logic gates [62–64]. Moreover, they are shown to be the very successful tools for the quantum simulator platforms [65–68].

6.2.2 Mapping to spin systems

Writing the complete Hamiltonian for the system of Rydberg atoms would require taking into account various contributions. However, in a simplified picture, the system can be mapped to the spin-$1/2$ model with state $|\downarrow\rangle$ representing the low-energy state, and state $|\uparrow\rangle$ representing the highly excited Rydberg state [69–71]. The Rydberg blockade mechanism and the laser excitation can be encoded through the local Pauli matrix operators, and, in the rotating wave approximation, the Hamiltonian reads:

$$\hat{H} = \sum_{i} \frac{\hbar\Omega}{2}\sigma_x^i + \frac{1}{2}\sum_{i\neq j} U_{ij} n_z^i n_z^j, \tag{6.4}$$

where $n_z = \frac{1}{2}(\sigma_z + 1)$. Here, Ω is the Rabi frequency, and the term σ_x^i describes the laser excitation. The interaction term $n_z^i n_z^{i+1}$ describes the Rydberg blockade with Van der Waals potential $U_{ij} = C_6/R^6$ - when one of the particles in a pair is in the state $|\downarrow\rangle$, the interaction vanishes. When both particles are in the state $|\uparrow\rangle$, the interaction shifts the energy upwards. This model corresponds to Ising model in transversal and longitudinal field. In the more realistic scenario, the laser detuning contribution $\hat{H}_\delta = -\delta\sum_{i=1}^{N}\sigma_z^i$ is also taken into account.

In this thesis, we analyze the nearest-neighbour Rydberg model, and regroup the coefficients in Eq. (6.4) as following:

$$\hat{H} = J\Big(\sum_{i=1}^{N-1} n_z^i n_z^{i+1} + \tilde{\Omega}\sum_{i=1}^{N}\sigma_x^i\Big) = J\Big(\sum_{i=1}^{N-1}\frac{1}{2}(1+\sigma_z^i)\frac{1}{2}(1+\sigma_z^{i+1}) + \tilde{\Omega}\sum_{i=1}^{N}\sigma_x^i\Big), \tag{6.5}$$

The parameter $\tilde{\Omega}$ is proportional to the Rabi frequency, and the energyscale is again expressed in the units of $J = 1$.

For the Rydberg model study, we follow the same workflow as for the Ising model. We first discuss the energy spectrum on the example of the exactly solved $N = 8$ system, and give the physical interpretation of the ground and the first excited state in terms of spin orientations. Then, we provide the convergence parameter analysis, and finally, present the results of our simulations.

6.2.3 Energy spectrum properties

Similarly as in the case of the Ising model, we expect the Rydberg model to manifest two regimes, depending on the laser excitation parameter $\tilde{\Omega}$. When $\tilde{\Omega}$ is large, the σ_x represents the main contribution in the Hamiltonian, and therefore the system favours the alignment of the spins along the x-axis. This is analogous to the Ising's $\lambda \gg 1$ scenario. When $\tilde{\Omega}$ is small, the leading contribution is due to the Rydberg blockade. This regime favours any combination of spin orientations in which the two nearest-neighbour spins are not both in a state $|\uparrow\rangle$. Therefore, for $\tilde{\Omega} = 0$, we expect the multiple degeneration of the ground state.

The first 100 lowest energy levels of the Rydberg model spectrum obtained by the exact diagonalization of the $N = 8$ Hamiltonian are plotted in Fig. 6.15. The left plot shows the regime of the small $\tilde{\Omega}$, where the gaps between the states are small, i.e. the low-energy states are close to the degenerate. Moving to the middle and right plot, the ground state degeneracy breaks with increasing $\tilde{\Omega}$, and we can observe that the states start to regroup.

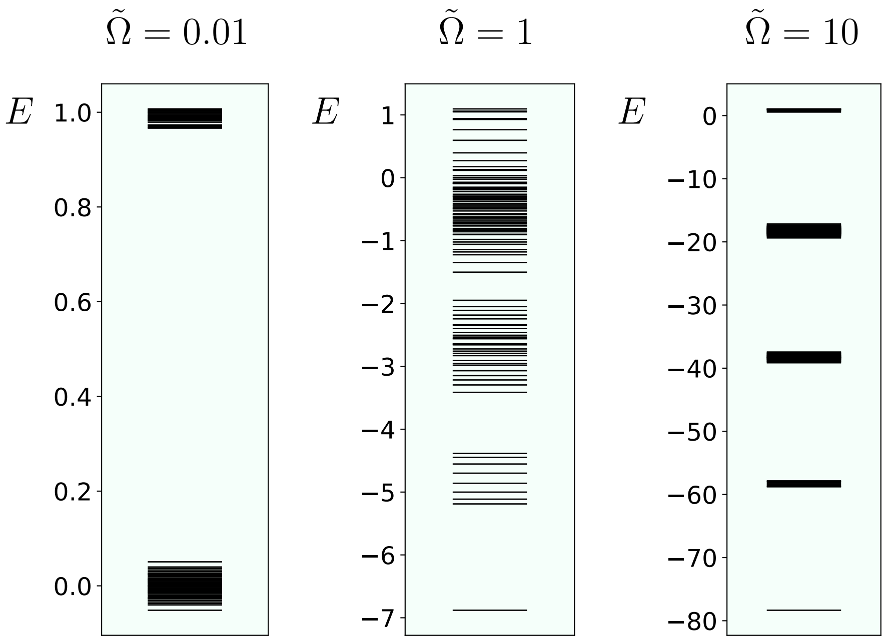

Figure 6.15: Energy spectrum for $N = 8$ particle Rydberg atom model for $\tilde{\Omega} = 0.01$ (left), $\tilde{\Omega} = 1$ (middle), and $\tilde{\Omega} = 10$ (right). The first 100 energy states are plotted. Energy is expressed in the units of Hamiltonian energyscale J.

In the limit of vanishing $\tilde{\Omega}$, a more detailed analysis shows that the number of degenerated states in dependence of the number of particles follows the Fibonacci sequence. For $N = 8$, the ground state is 55-fold degenerate, for $N = 16$, it is 2584-fold degenerate, and for $N = 32$ it is 2178309-fold degenerate. The degeneracy occurs because the ground state is represented by any spin orientation in which the two nearest-neighbour spins are not aligned in the same direction along the z-axis. At this point, we can already suspect that such large ground state degeneracy will greatly decrease the accuracy of our method in the low-$\tilde{\Omega}$ region.

Moving to the higher values of $\tilde{\Omega}$, the degeneracy breaks, and the ground state corresponds to the state with all the spins aligned along the x-axis. The physical interpretation of the low-energy states in the limits of small $\tilde{\Omega}$ and large $\tilde{\Omega}$ are depicted in Fig. 6.16. Unlike for the Ising model, there is no evidence of a quantum phase transition in the parameter range we tested for Rydberg atom model in Eq. (6.5) (further supported with Fig. 6.23). However, there are phase transitions present when the detuning term is included in the Hamiltonian [72].

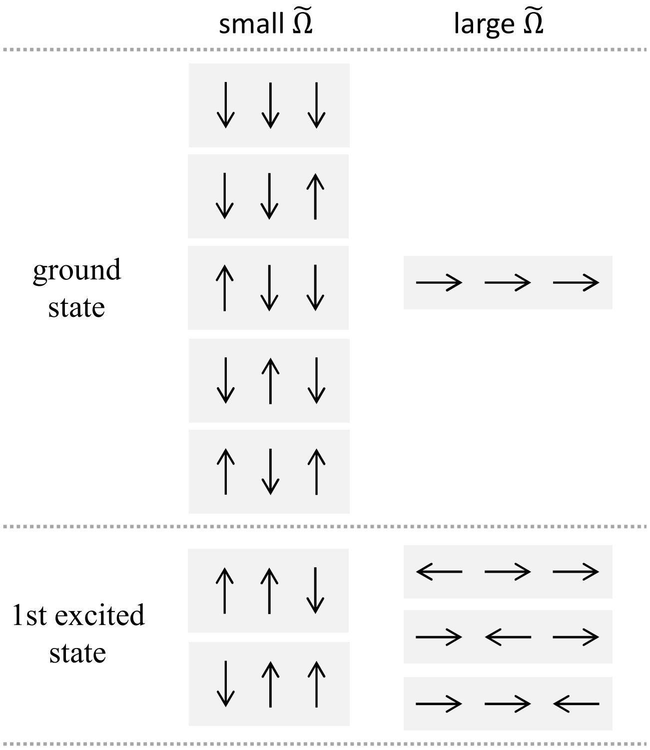

Figure 6.16: Physical interpretation of the ground and the first excited states of the Rydberg atom model. The alignment of the spin is indicated with the arrow. The direction of x-axis is taken to be along the horizontal axis, and the direction of z-axis is taken to be along the vertical axis.

6.2.4 Convergence parameters

In this section, we examine how the convergence parameters m_{LPTN}, m_{TTO}, and K_0 influence the accuracy of the results for the Rydberg model. The error introduced by the finite-sized maximal dt is discussed in Appendix A.

The values for the convergence parameters m_{LPTN}, m_{TTO}, and K_0 are chosen as in the case of the Ising model and are shown in Table 6.2. For the Rydberg model, we analyze the norm loss at the point $\tilde{\Omega} = 0.05$, where the largest entanglement was observed (shown in the results in the next section). The norm loss dependence on convergence parameters m_{LPTN}, m_{TTO}, and K_0 is shown in Fig. 6.17 for $N = 16$, and in Fig. 6.18 for $N = 32$. The norm loss as a function of temperature for $\tilde{\Omega} = 0.05$ is plotted in Fig. 6.19. As it can be seen from the plots in Fig. 6.17, Fig. 6.18, and Fig. 6.19, the norm is preserved only for a very low temperature. This is expected, since the point $\tilde{\Omega} = 0.05$ is very close to $\tilde{\Omega} = 0$, where the ground state is extremely degenerate, thus a very large number of excited states starts contributing very quickly with increasing the temperature. As observed from Fig. 6.19, the temperature range within which the norm loss is smaller than 10^{-2} is up to $T \approx 0.03$ for $N = 16$ and up to $T \approx 0.02$ for $N = 32$. Hence, the results are considered accurate for temperatures below these values.

	$N = 8$	$N = 16$	$N = 32$
m_{LPTN}	256	50	35
m_{TTO}	256	50	35
K_0	256	100	85

Table 6.2: Maximal bond dimensions used for the Rydberg atom model simulations.

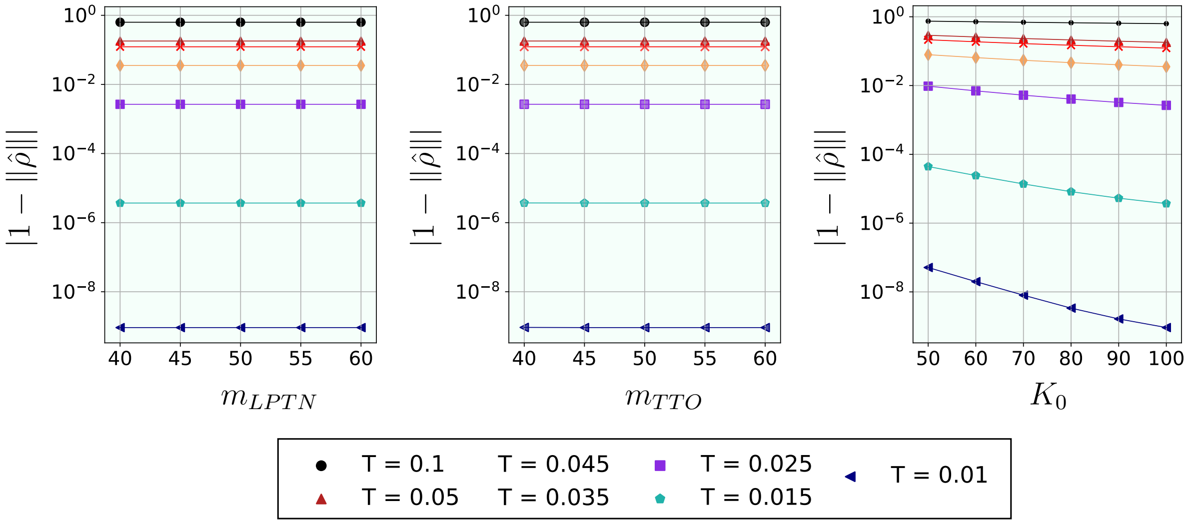

Figure 6.17: Density matrix norm loss $|1 - \|\hat{\rho}\||$ for Rydberg atom model with $N = 16$ particles, plotted as a function of one of the convergence parameters (left - m_{LPTN}, middle - m_{TTO}, right - K_0), while the remaining convergence parameters are kept constant, with the values $m_{LPTN} = 50$, $m_{TTO} = 50$, $K_0 = 100$. Different color curves correspond to different temperatures indicated in legend. Temperature T is expressed in units of J/k_B.

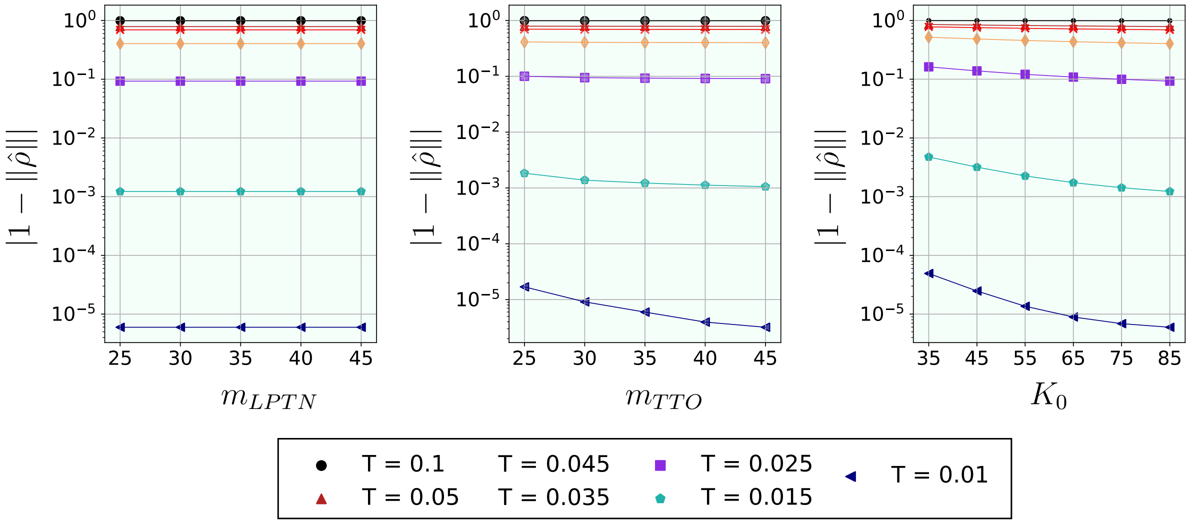

Figure 6.18: Density matrix norm loss $|1 - \|\hat{\rho}\||$ for the Rydberg atom model with $N = 32$ particles, plotted as a function of one of the convergence parameters (left - m_{LPTN}, middle - m_{TTO}, right - K_0), while the remaining convergence parameters are kept constant, with the values $m_{LPTN} = 35$, $m_{TTO} = 35$, $K_0 = 85$. Different color curves correspond to different temperatures indicated in legend. Temperature T is expressed in units of J/k_B.

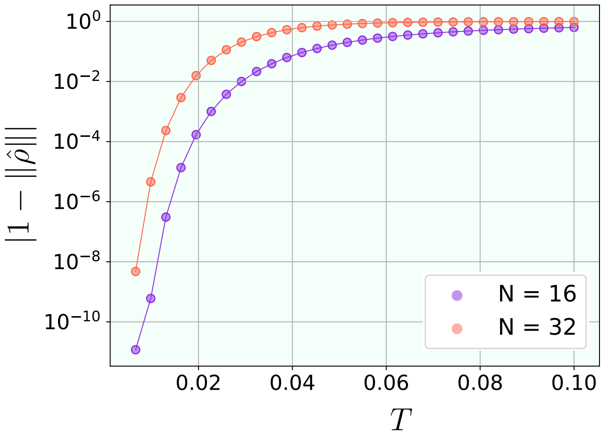

Figure 6.19: Density matrixnorm loss $|1 - ||\hat{\rho}|||$ for Rydberg atom model for $N = 16$ and $N = 32$ particles, plotted as a function of temperature T. The convergence parameters are chosen as indicated in Table 6.2. Temperature T is expressed in units of J/k_B.

6.2.5 Finite temperature properties

The results for the Rydberg atom model are presented in this section. First, to capture the qualitative features of the model, the $\tilde{\Omega} - T$ grids are computed for the purity, Von Neumann entropy, and negativity. The grid with the purity is shown in Fig. 6.20. We can observe two distinguishable regions. In the region approximately below the diagonal, the system is dominantly in the ground state, i.e. the state of all spins aligned in the x direction. This configuration stays more robust with the temperature in the large $\tilde{\Omega}$ zone because increasing $\tilde{\Omega}$ increases the energy gap between the ground and excited states. In other region, above the diagonal, the purity is very close to zero. Increasing the system size makes the boundary between these regions more clear. The same two regions can be distinguished by observing the Von Neumann entropy (Fig 6.21).

By looking at the negativity in Fig. 6.22, we identify the point of the largest entanglement around $\tilde{\Omega} = 0.05$. In analogy with the Ising model, where the most entanglement was present at the ground state degeneracy breaking point $\lambda_c = 1$, in the Rydberg spectrum for $N = 8$, at $\tilde{\Omega} = 0.05$ we spot that the degeneracy breaking occurs for one of the excited states. Fig. 6.23 shows the $N = 8$ Rydberg model energy levels divided by the ground state energy, as a function of $\tilde{\Omega}$. The point of the maximal entanglement is marked with a red vertical line.

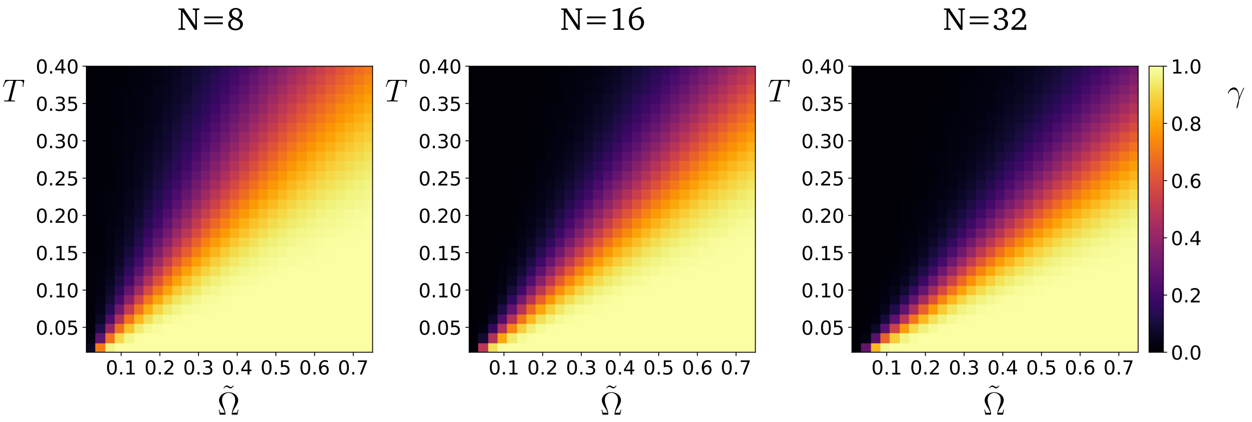

Figure 6.20: Purity γ for the Rydberg atom model as a function of parameter $\tilde{\Omega}$ and temperature T computed for different system sizes. Temperature T is expressed in units of J/k_B.

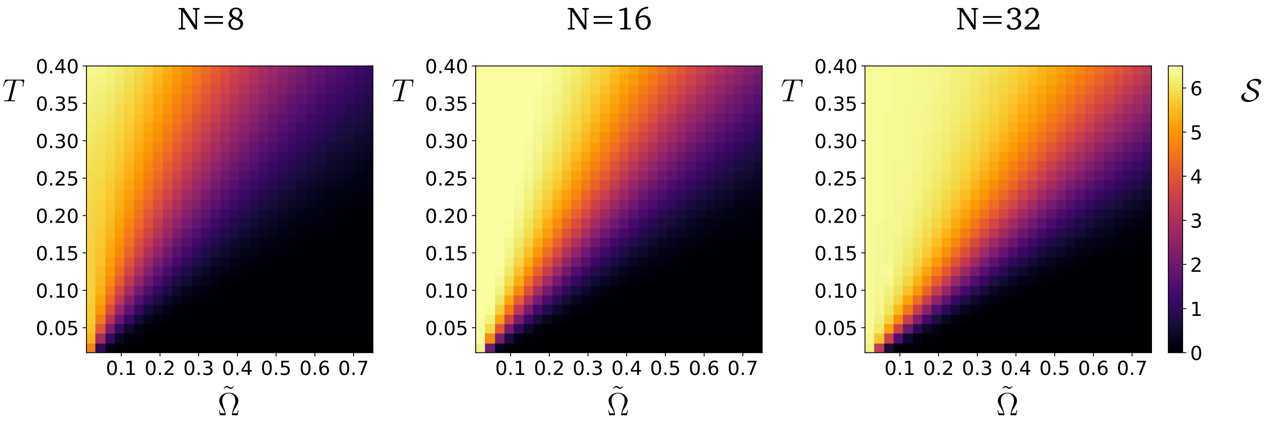

Figure 6.21: Von Neumann entropy $\mathcal{S}$ for the Rydberg atom model as a function of parameter $\tilde{\Omega}$ and temperature T computed for different system sizes. Temperature T is expressed in units of J/k_B.

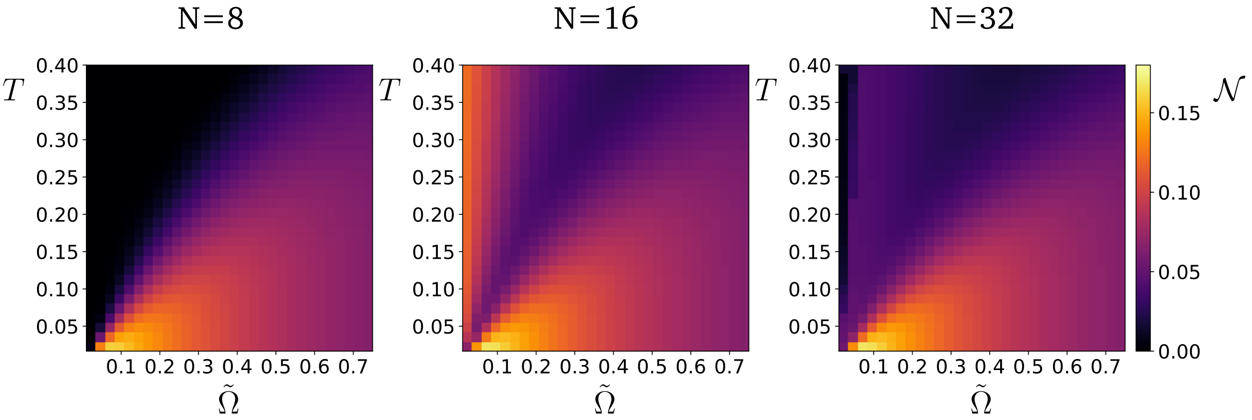

Figure 6.22: Negativity $\mathcal{N}$ of the Rydberg atom model as a function of parameter $\tilde{\Omega}$ and temperature T computed for different system sizes. Temperature T is expressed in units of J/k_B.

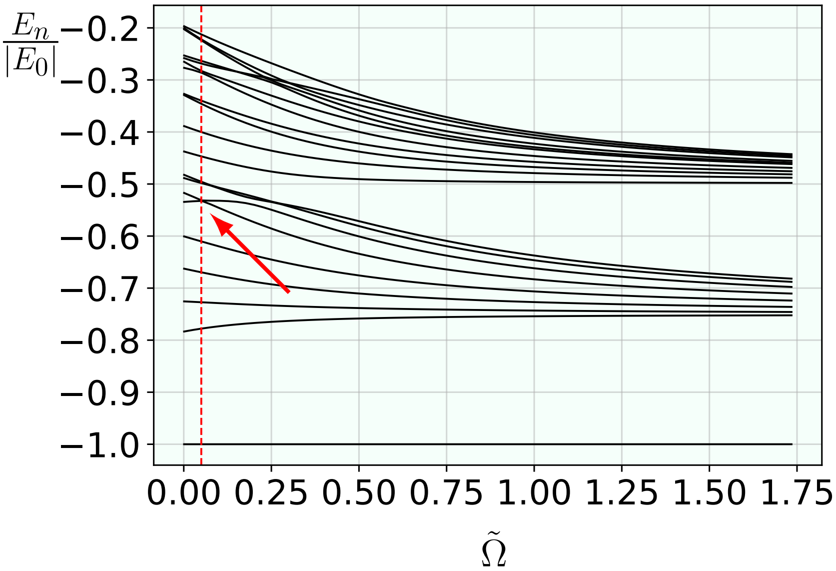

Figure 6.23: Rydberg model energy levels E_n divided by the ground state energy $|E_0|$ as a function of parameter $\tilde{\Omega}$, computed for $N = 8$. The vertical red line is positioned at $\tilde{\Omega} = 0.05$ and indicates the point of the largest entanglement. The red arrow points at the point where the degeneracy of the excited energy levels breaks.

Another effect to notice in Fig. 6.22 is that, in the case of $N = 16$, for low $\tilde{\Omega}$ values, the negativity is increasing with temperature. We expect this to be the consequence of the error emerging from truncating the K_0 bond dimension. The same effect cannot be observed for $N = 8$, where the bond dimensions were not truncated.

Altogether, the plots in Fig. 6.20, Fig. 6.21, and Fig. 6.22 are useful for the qualitative analysis of the system's robustness with temperature. In the mixed-state region above the diagonal, we cannot account on the accuracy of the values of the results in the case of $N = 16$ and $N = 32$.

We now focus on the largest entanglement point, $\tilde{\Omega} = 0.05$. The computed purity for different system sizes are shown in Fig. 6.24. Again, for $N = 16$ and $N = 32$, the values can be considered accurate only for the low-temperature range, up to $T \approx 0.03$ for $N = 16$ (indicated with red line) and up to $T \approx 0.02$ for $N = 32$ (indicated with blue line). The property values in higher temperature region serve as a qualitative insight. The scaled and unscaled Von Neumann entropy and Von Neumann entropies are shown in Fig. 6.25. From the right plot in Fig. 6.25, it is clearly visible that the scaled Von Neumann entropy curves coincide for the temperature range in which the results are expected to be accurate, indicated with red line for $N = 16$ and blue line for $N = 32$. The Rényi entropies of different order α are shown in Fig. 6.26, with the Von Neumann entropy again plotted to confirm that it coincides with the Rényi entropy of the order $\alpha \longrightarrow 1$.

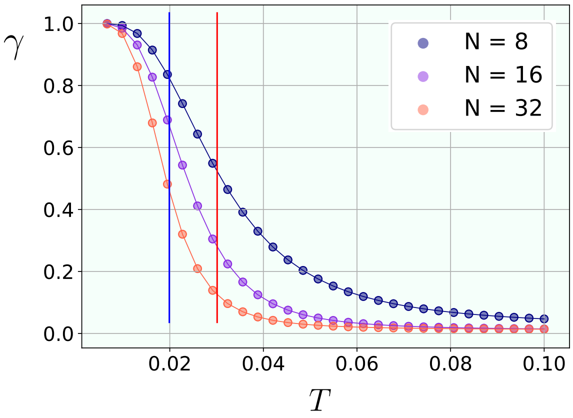

Figure 6.24: Purity γ for Rydberg atom model at the point of maximal entanglement $\tilde{\Omega} = 0.05$, computed as a function of temperature T for different system sizes. As a consequence of truncation error, for $N = 16$ we expect the accurate results up to $T \approx 0.03$ (red line), and for $N = 32$ up to $T \approx 0.02$ (blue line). The values plotted in higher temperature region serve as a qualitative insight. For $N = 8$ there is no truncation error. Temperature T is expressed in units of J/k_B.

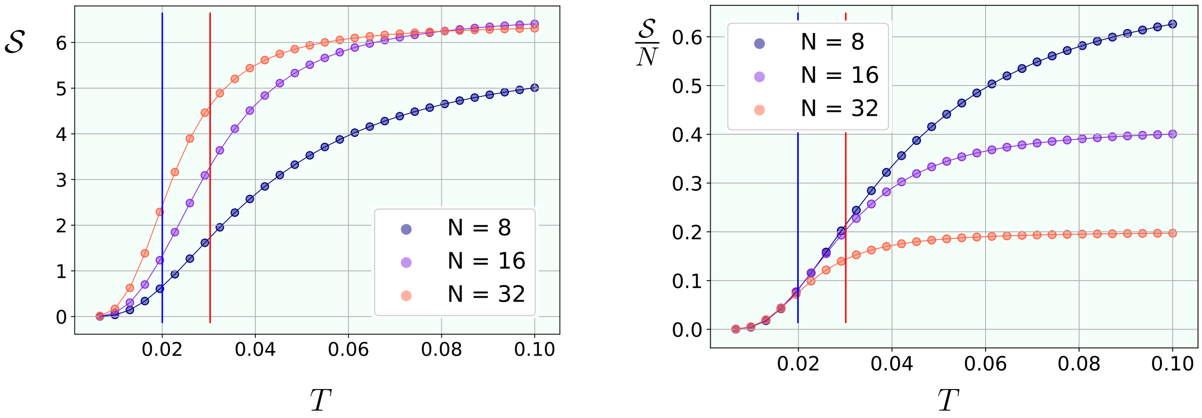

Figure 6.25: Von Neumann entropy $\mathcal{S}$ (left) and scaled Von Neumann entropy $\mathcal{S}/N$ (right) as a function of temperature T, computed for Rydberg atom model model at the point of maximal entanglement $\tilde{\Omega} = 0.05$ for different system sizes. As a consequence of truncation error, for $N = 16$ we expect the accurate results up to $T \approx 0.03$ (red line), and for $N = 32$ up to $T \approx 0.02$ (blue line). We observe the agreement of the scaled Von Neumann curves up to the temperature of the predicted accuracy decrease. For $N = 8$ there is no truncation error. Temperature T is expressed in units of J/k_B.

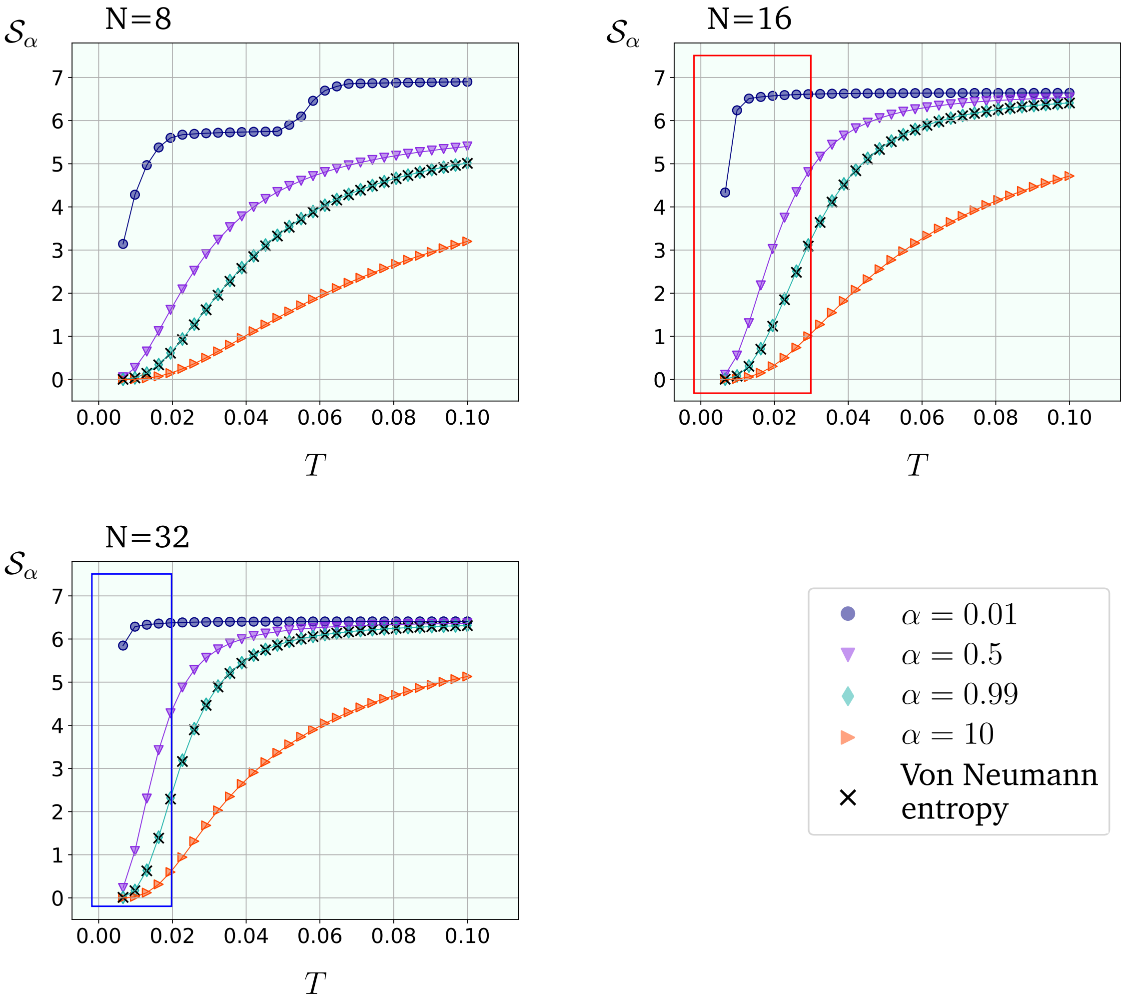

Figure 6.26: Rényi entropies $\mathcal{S}_\alpha$ as a function of temperature T, computed for Rydberg atom model for different values of parameter α. Data at the maximal entanglement point $\Omega = 0.05$. Figures for system sizes $N = 8$ (up left), $N = 16$ (up right) and $N = 32$ (down left). In addition, the Von Neumann entropy is plotted to confirm the alignment with the Rényi entropy in the limit $\alpha \longrightarrow 1$. As a consequence of truncation error, the regions in which the results are considered accurate are enclosed with the rectangles. The values plotted in higher temperature region serve as a qualitative insight. For $N = 8$ there is no truncation error. Temperature T is expressed in units of J/k_B.

Fig. 6.27 shows the computed entanglement measures, negativity and EoF, for different system sizes. Note that, although the crossing of the negativity curves for $N = 16$ and $N = 32$ can be observed, these effects are within the temperature range in which the results cannot taken as accurate. For computing the EoF, as in the case of the Ising model, the further reduction of the K_0 bond dimension had to be made. The criterion taken for K_0 reduction in the case of the Rydberg model is the same as for the Ising model: the maximal value of K_0 is set to 20, and all the states with probabilities p_j such that $p_j/p_0 < 10^{-4}$, where p_0 is the ground state probability, were discarded. The EoF was computed for the temperature range up to $T = 0.01$.

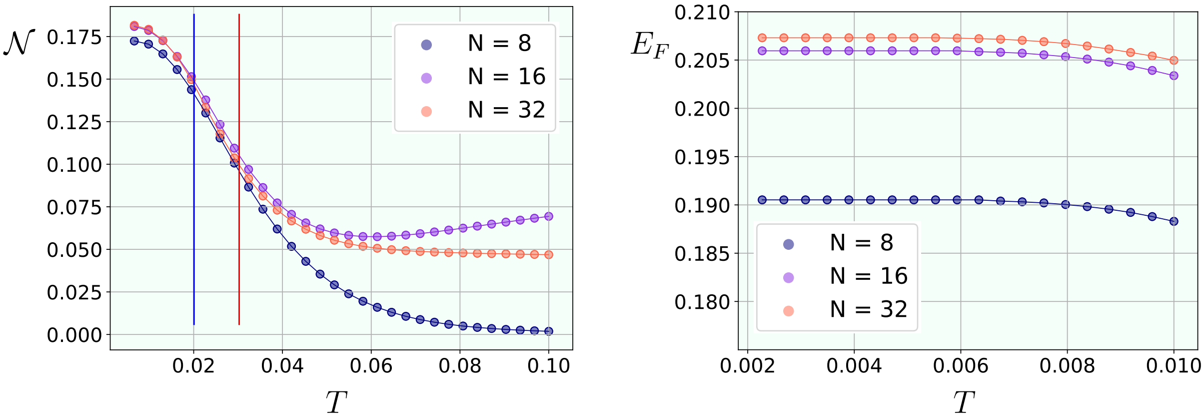

Figure 6.27: Negativity $\mathcal{N}$ (left) and entanglement of formation E_F (right) as a function of temperature T, computed for Rydberg atom model at the point of maximal entanglement $\tilde{\Omega} = 0.05$ for different system sizes. For negativity: as a consequence of truncation error, for $N = 16$ we expect the accurate results up to $T \approx 0.03$ (red line), and for $N = 32$ up to $T \approx 0.02$ (blue line). The values plotted in higher temperature region serve as a qualitative insight. For $N = 8$ there is no truncation error. The values of EoF are expected to be the good estimate in entire temperature range plotted. Temperature T is expressed in units of J/k_B.

7 Summary and outlook

In this thesis, we have developed and implemented the numerical method based on Tensor Network Methods (TNM) for computing the finite temperature density matrix of the many-body quantum systems. In particular, we obtain the density matrix in a Tree Tensor Operator (TTO) form. TTO form compresses the information about the thermal probabilities and states into a single root tensor, where the root tensor's dimension is dictated by the number of thermal states contributing to the density matrix. In the finite-temperature scenario thermal probabilities decay exponentially with the state's energy, thus we reduce the root tensor's dimension by discarding the high-energy states. By reducing a density matrix to the single tensor of controllable dimensions, we escape the problem of exponential scaling of the quantum many-body Hilbert space. Therefore, we are gaining algorithmic efficiency and enabling the computation of the bipartite entanglement measures, otherwise intractable in the case of large number of particles. We employ our method to study one-dimensional systems composed of $N = 8$, 16, and 32 particles. We examine the nearest-neighbour quantum Ising model and a Rydberg atom model.

Obtaining a TTO density matrix is a two-step procedure. We first evolve the Locally Purified Tensor Network (LPTN) form of the density matrix from infinite temperature to some arbitrary temperature using the imaginary time evolution algorithm. Once we have the LPTN form, we transform it to the TTO form by the procedure introduced in this thesis using tensor operations. To keep the tensor dimensions reasonably low, we truncate the singular values after each singular value decomposition (SVD) in the LPTN to TTO conversion procedure. We implement the functions for computing purity, Von Neumann entropy, Rényi entropies of any order, and entanglement of formation (EoF) from the TTO density matrix.

Applying the method to the Ising model, we correctly described the quantum phase transition and furthermore distinguished three quantum phases at the finite temperature: feromagnetic, paramagnetic, and the disordered finite temperature phase. The point of largest entanglement was observed at the critical point of the Ising model, $\lambda_c = 1$. By analyzing the norm loss acquired due to the SVD throughout the LPTN to TTO conversion procedure, we determine the temperature range in which we expect our results to be accurate. The error is mostly a consequence of truncating the number of thermal states contributing to the density matrix. Therefore, the error increases with increasing the temperature, as higher temperature entails the larger probability of finding a system in an excited energy state.

Moreover, we analyzed a system of Rydberg atoms trapped in the optical tweezer arrays. We used the model in which the highly excited Rydberg state and ground state are mapped onto the spin-$1/2$ states. The laser excitation in the rotating wave approximation and the Rydberg blockade mechanism are encoded using the Pauli matrix operators. We observe two different regimes at finite temperature: the regime in which the system is dominantly in the ground state, corresponding to the state with all spins aligned in the x direction, and the finite temperature disordered phase. The point of largest entanglement was observed at the value of the rescaled Rabi frequency parameter $\tilde{\Omega} = 0.05$. At the point of the maximal entanglement, the accurate simulations of the Rydberg atom model are accessible in a smaller temperature range compared to the Ising model. We show that the accessible temperature range depends on properties of the system's energy spectrum. As our method aims to describing the mixed state with the low-energy states, the gaps in the low-energy part of the energy spectrum decrease the higher-energy state thermal probabilities and preserve the accuracy of the results. The model we used for modeling Rydberg atoms contains an extreme ground state degeneracy in the limit of $\tilde{\Omega} \longrightarrow 0$, thus, for $\tilde{\Omega} \approx 0$ the accuracy of the results decreases very quickly with the temperature.

Since the systems of neutral atoms trapped in the optical tweezers are shown to be the promising candidates for realistic quantum computing and simulation platforms, the insight in their finite-temperature properties is of great importance. The model used in this thesis has a drawback of the multi-fold ground state degeneracy. However, this degeneracy can be broken by including other contributions to the system's Hamiltonian. Since the important feature of the Rydberg atoms are their long-range interactions, for the future work, we propose including the next-nearest, or even further neighbours in the algorithm. Including the next-nearest-neighbour interactions requires upgrading the imaginary time evolution algorithm. However, the LPTN to TTO conversion would remain unchanged. The long range interactions would surely give rise to the ground state degeneracy breaking. Moreover, even including the laser detuning contribution influences the system's spectrum, and possibly expands the temperature range reachable to our method.

Another possibility our method offers is testing the EoF's additivity property for quantum many-body systems at finite temperatures (and mixed-states in general). As discussed in Section 3.4.2, showing that EoF is additive makes this entanglement monotone equivalent to the entanglement cost. The additivity testing requires performing two operations - tensor product of the two density matrices, and computing its EoF. Since the tensor product can be performed in the LPTN representation simply by concatenating the two LPTN's along their left or right boundary, by converting it to a TTO, we have the access to computing the EoF for the tensor product of the two mixed states.

Appendices

Appendix A Imaginary time evolution error

To test the error induced by the finite-sized dt, we compute the purity and negativity from the exact $N = 8$ density matrix, and compare it to the same properties extracted from the TTO obtained with our method without any truncation of the singular values. By computing the non-truncated TTO, we remove all the other sources of error apart from the imaginary time evolution. For $N = 8$, the non-truncated TN have the maximal bond dimension equal to the dimension of the total Hilbert space, i.e. $d^N = 2^8 = 256$. Therefore, we set $m_{LPTN} = m_{TTO} = 256$. For the simulations, we chose the maximal time step $dt = 0.05$.

A.1 Ising model

The comparison of the exact solution and the solution obtained by imaginary time evolution without truncation for $N = 8$ Ising model is shown on Fig. A.1 for purity and Fig. A.2 for negativity. On both Fig. A.1 and Fig. A.2 we observe there exists an area of the particularly large error in the region around $\lambda \approx 0.7$ and small temperature T. This area corresponds to the boundary of the quantum paramagnetic phase, meaning that the finite dt error manifests as the slight shift of the quantum phase position in the $\lambda - T$ diagram. Besides the phase boundaries, the error stays reasonably low. Nevertheless, the error can be reduced by choosing a smaller value of dt, with a roughly linear increase of the simulation time.

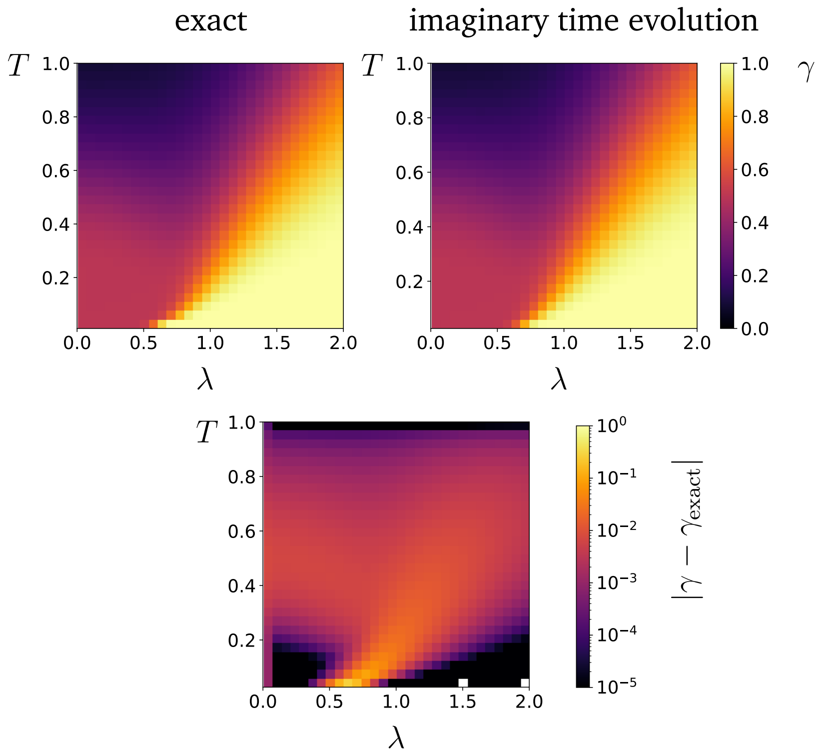

Figure A.1: Comparison of $N = 8$ Ising model purity γ for density matrix obtained by exact diagonalization of Hamiltonian (top left) and density matrix evolved by imaginary time evolution without truncation (top right). The bottom plot shows the absolute difference between purities computed in these two ways. Temperature T is expressed in units of J/k_B.

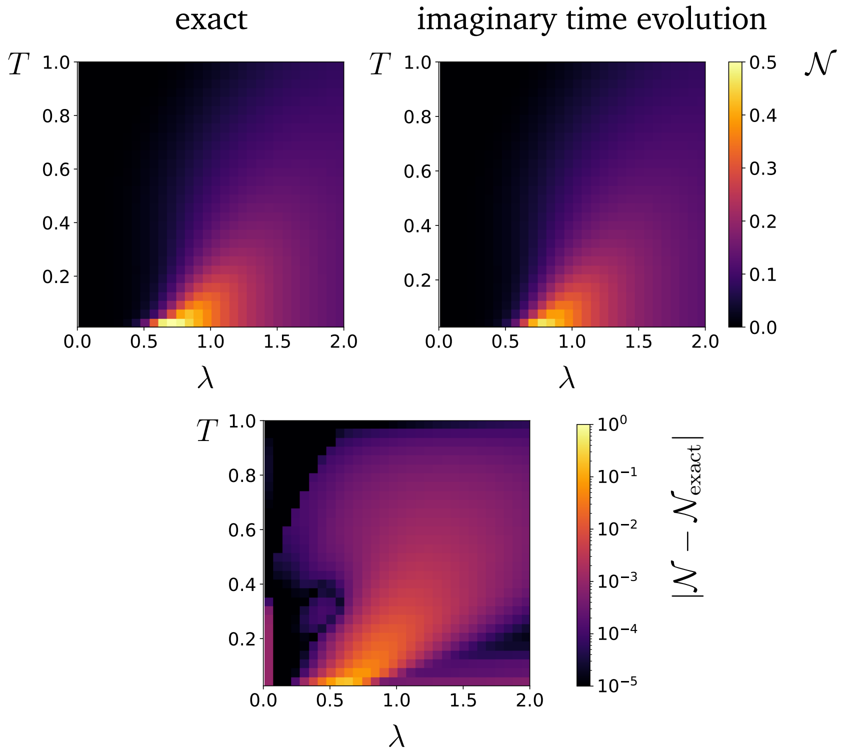

Figure A.2: Comparison of $N = 8$ Ising model negativity $\mathcal{N}$ for density matrix obtained by exact diagonalization of Hamiltonian (top left) and density matrix evolved by imaginary time evolution without truncation (top right). The bottom plot shows the absolute difference between negativities computed in these two ways. Temperature T is expressed in units of J/k_B.

A.2 *Rydberg atom model*

The comparison of the exact solution and the solution obtained by imaginary time evolution without truncation for $N = 8$ Rydberg atom model is shown on Fig. A.3 for purity and Fig. A.4 for negativity. In both figures, we see that the error is largest in the low-temperature and small-$\tilde{\Omega}$ area of the diagram. As discussed in Section 6.2, the area around small $\tilde{\Omega}$ is the part of the diagram influenced by the finite temperature the most. Moreover, similarly to the Ising model, for the purity the zone of the large error represents represents the boundary between the region in which the main contribution comes from the ground state, and the temperature-influenced region in which many states contribute to the density matrix.

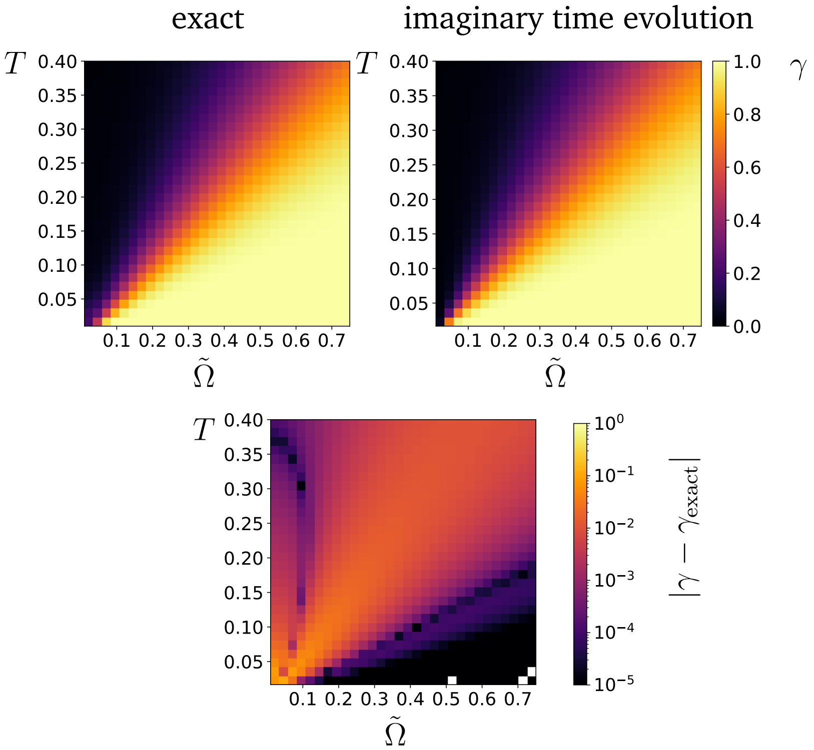

Figure A.3: Comparison of $N = 8$ Rydberg atom model purity γ for density matrix obtained by exact diagonalization of Hamiltonian (top left) and density matrix evolved by imaginary time evolution without truncation (top right). The bottom plot shows the absolute difference between purities computed in these two ways. Temperature T is expressed in units of J/k_B.

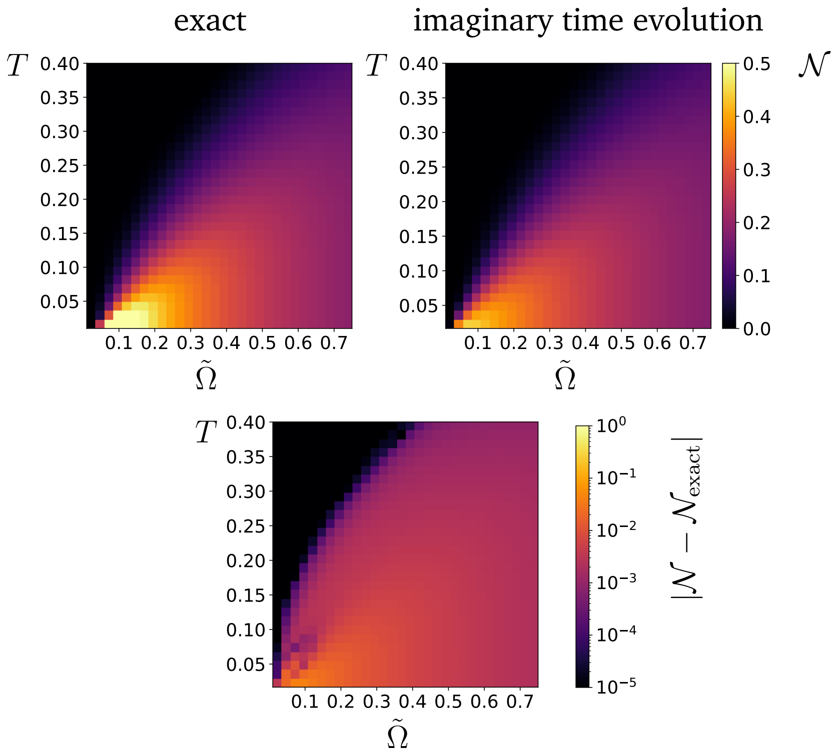

Figure A.4: Comparison of $N = 8$ Rydberg atom model negativity for density matrix obtained by exact diagonalization of Hamiltonian (top left) and density matrix evolved by imaginary time evolution without truncation (top right). The bottom plot shows the absolute difference between negativities computed in these two ways. Temperature T is expressed in units of J/k_B.

8 Prošireni sažetak

8.1 Uvod

Nadilazeći klasične zakone, uspon kvantne mehanike početkom dvadesetog stoljeća doveo je do ponovnog uspostavljanja temeljnih koncepata fizikalne stvarnosti. Probabilistički pristup, koji se nekada koristio samo kao alat za tretiranje našeg nedostatka znanja o sustavima, pokazao se kao istinska priroda fizikalnih zakona na mikroskopskim skalama. Ideja o iskorištavanju fundamentalnih principa kvantne fizike u svrhu konstrukcije računalnog uređaja pojavila se 1982. godine kao odgovor na ograničenja prisutna pri klasičnim simulacijama višečestičnih kvantnih sustava. Feynman je predložio, želimo li simulirati kvantne sustave, trebamo stvoriti računalo čiji elementi slijede kvantne zakone [1]. Feynmannov prijedlog otvorio je vrata velikom broju novih mogućnosti koje bi kvantne tehnologije mogle ponuditi. Iskorištavanjem superpozicije, interferencije i isprepletenosti, uspostavljeni su teorijski i eksperimentalni temelji koji omogućuju konstrukciju kvantnih qubita i njihovih elementarnih operacija [4]. Potencijalne primjene danas nadilaze simulaciju fizičkih sustava, šireći se, primjerice, na kvantnu kriptografiju i razvoj sigurnijih komunikacijskih protokola [2], ili čak upotrebu za obnovljive izvore energije [3]. Međutim, tehnološka prepreka s kojom se trenutno suočavamo je da, iako su eksperimentalne izvedbe kvantnih logičkih vrata moguće u kvantnim sustavima malog broja konstituenata, potpuna kontrola skalabilnog, pouzdanog kvantnog procesora još uvijek je otvoren izazov.

Do sada, nekoliko se eksperimentalnih platformi pokazalo prikladnim fizikalnim predstavnicima kvantnih računala, primjerice, zarobljeni ioni [5–7] i supravodiči [8, 9]. Posljednjih godina, značajan napredak postignut je u kvantnom računarstvu s neutralnim Rydbergovim atomima, otvarajući vrata još jednom obećavajućem pristupu [10–12]. Rydbergovi atomi su visoko pobuđeni atomi, s vanjskim elektronom daleko od atomskog kationa. Zbog njihovog iznimno velikog električnog dipolnog momenta, pokazuju jake, lako upravljive interakcije, kako međusobno tako i s vanjskim poljem [13], što ih čini izvrsnim kandidatima za programabilne kvantne uređaje.

Budući da se u eksperimentalnim realizacijama ovi uređaji nikada ne mogu potpuno ohladiti na temperaturu apsolutne nule, postoji osobita potreba za ispitivanjem njihovih svojstava na konačnim temperaturama. S ciljem stjecanja boljeg razumijevanja temeljnih, kolektivnih fizikalnih fenomena te poboljšanja precizne kontrole kvantnih računalnih platformi, u ovom radu numerički proučavamo fiziku više tijela snažno koreliranih kvantnih sustava na konačnim temperaturama.

Iako postoje brojne teorije posvećene opisivanju fizike pojedinačnih čestica, proširenje analize na sustave velikog broja konstituenata te hvatanje njihovog kolektivnog ponašanja iznimno je težak zadatak, čak i u slučaju najjednostavnijih modela. Iako, u načelu, znamo postaviti vodeće matematičke jednadžbe, problem kvantne fizike više tijela leži u činjenici da broj stupnjeva slobode raste eksponencijalno s brojem čestica u sustavu. Stoga složenost jednadžbi za velike sustave zahtijeva korištenje prikladnih aproksimacija.

S analitičkog gledišta, standardni pristup razumijevanju sustava više tijela polazi od uvođenja pojednostavljenja modela, na primjer Hartree-Fockova aproksimacija ili aproksimacija slučajnih faza. Konstruiramo efektivni Hamiltonijan i testiramo prikazuje li ključna svojstva izvornog Hamiltonijana. Međutim, usprkos moćnim matematičkim tehnikama i dosjetljivom iskorištavanju specifičnih svojstava sustava, za većinu Hamiltonjana su potpuno analitička rješenja još uvijek nedostižna. Stoga je nužna integracija analitičkih pojednostavljenja s numeričkim alatima i metodama.

Svejedno, čak su i numeričke tehnike uvelike ograničene eksponencijalno rastućim Hilbertovim prostorom višečestičnih kvantnih sustava. Kao primjer, možemo pogledati sustav N čestica spina $1/2$. Ovakav sustav nalazi se u Hilbertovom prostoru dimenzije 2^N. S gledišta računarstva, može se izračunati da pohranjivanje matrice Hamiltonijana s *float* elementima u slučaju $N = 8$ spinova zahtijeva $2 \cdot 8 \cdot 2^8 \cdot 2^8 \approx 1,05$ megabajta memorije. Međutim, eksponencijalno skaliranje implicira da ova količina eskalira vrlo brzo s povećanjem broja čestica. Za sustav od $N = 32$ spinova, pohranjivanje Hamiltonijana kao matrice zahtijeva $2 \cdot 8 \cdot 2^{32} \cdot 2^{32} \approx 2,95 \cdot 10^5$ petabajta memorije, što je potpuno izvan dosega bilo koje egzaktne metode dijagonalizacije. Stoga, egzaktan tretman sustava ograničen je na sustave malih veličina, vrlo daleko od termodinamičke granice.

Srećom, iako postoji vrlo velik broj mogućih stanja u kojima sustav može biti, nisu sva stanja jednako relevantna. S obzirom da u prirodi čestice vrlo često stupaju u interakciju samo sa svojih nekoliko najbližih susjeda, većina Hilbertovog prostora zapravo ostaje nenaseljena. Može se pokazati da niskoenergetska stanja nekritičnih Hamiltonijana s lokalnim međudjelovanjima slijede zakon površine entropije prepletenosti [14, 15]. Zakon površine nam govori da se entropija prepletenosti podregije prostora skalira kao površina granice ove podregije, umjesto kao njezin volumen. Samo stanja koja su u skladu sa zakonom površine su kandidati za niskoenergetska svojstvena stanja, efektivno reducirajući enormno veliki Hilbertov prostor na mnogo manji podprostor.

Stoga, postavljanjem ograničenja i razlikovanjem relevantnih od nerelevantnih stanja, možemo izbjeći baratanje cijelim Hilbertovim prostorom i drastično uštedjeti računalne resurse. Sa svrhom prepoznavanja relevantnih stanja i relevantnih stupnjeva slobode, razvijena je skupina numeričkih metoda, nazvanih metode mreža tenzora (eng. *Tensor Network Methods*, TNM). Unutar okvira TNM-a, kvantni objekti parametrizirani su skupom tenzora, razlažući čista kvantna stanja na lokalne strukture čija geometrija prati strukturu prepletenosti tih stanja. Stoga, složenost pisanja stanja u formalizmu mreža tenzora izravno se skalira s količinom njihove prepletenosti. TNM su začete razvitkom algoritama [16] stanja matričnog produkta (eng. *matrix product states*, MPS), koji su dokazano ekvivalentni [17, 18] renormalizacijske grupe matrice gustoće (eng. *density matrix renormalization group*, DMRG) koju je prethodno uveo White [20] 1992. godine kao metodu pronalaženja osnovnoga stanja kvantnih rešetki. Nakon uspjeha MPS-a, konstruiran je velik broj novih oblika mreža tenzora prikladnih za proučavanje sustava različitih veličina i u različitim režimima [21–24].

U ovom diplomskom radu razvili smo i implementirali algoritam temeljen na TNM prikladan za opisivanje svojstava sustava na konačnim temperaturama. Konkretno, analiziramo čistoću stanja, Von Neumannovu entropiju, Rényijeve entropije [25] te dva svojstva povezana s prepletenošću - negativnost [27, 28] i prepletenost formacije [26]. Međutim, iako su kvantne korelacije dobro proučene kod čistih stanja, analiza pri konačnim temperaturama, tj. kada su u pitanju miješana stanja, traži kompleksniji pristup. Za razliku od slučaja kada je sustav opisan vektorom stanja, kao pri temperaturi apsolutne nule, informacije o sustavu na konačnoj temperaturi sadržane su u matrici gustoće. Stoga, proučavanje takvih sustava zahtijeva drugačiji, složeniji skup alata. Kako bismo prevladali problem kvantificiranja prepletenosti na konačnim temperaturama, koristimo se posebno pogodnim oblikom mreža tenzora, nazvanim operatorima stablastih mreža tenzora (eng. *Tree Tensor Op-*

erators, TTO) [29]. Učinkovitim sažimanjem informacije sadržane u matrici gustoće miješanih kvantnih stanja, ovaj pristup omogućuje izračun bipartitnih mjera prepletenosti [30], koje su vrlo korisne za karakterizaciju kvantnih korelacija sustava u toplinskoj ravnoteži, ali i općenitije, za sva miješana kvantna stanja.

Kako bismo analizirali sustav, suočeni smo s netrivijalnim zadatkom pronalaska TTO oblika matrice gustoće. U ovom radu konstruirali smo obilazak koji koristi analogon MPS-a za miješana stanja - lokalno pročišćene mreže tenzora (eng. *locally purified tensor networks*, LPTN) [31]. Kako bismo stekli pristup svojstvima sustava na proizvoljnoj temperaturi, evoluirali smo LPTN oblik matrice gustoće na beskonačnoj temperaturi putem imaginarne vremenske evolucije [32]. Nakon što smo izračunali LPTN matricu gustoće na proizvoljnoj temperaturi, koristeći niz transformacija i manipulacija tenzora pretvorili smo ju u TTO oblik putem postupka razvijenog u ovom radu.

Algoritme smo primjenili na dobro poznatom jednodimenzionalnom Isingovom modelu, te na modelu Rydbergovih atoma. Konkretno, ispitali smo lanac Rydbergovih atoma veličine do 32 kubita, gdje su dva stanja kubita predstavljena osnovnim stanjem atoma i visoko pobuđenim Rydbergovim stanjem.

Nakon uvoda, u Poglavlju 8.2 dan je kratak pregled formalizma matrice gustoće te je razmotren koncept prepletenosti i zbog čega ona predstavlja vrijedan resurs za kvantne tehnologije. Raspravljen je problem kvantificiranja prepletenosti te su predstavljene neke uobičajene mjere prepletenosti. U Poglavlju 8.3 pružen je uvod u TNM te je demonstrirano kako različiti oblici TN mogu predstavljati kvantna stanja i operatore. Zatim je u poglavlju 8.4 objašnjen matematički okvir u kojemu se tretiraju sustavi na konačnim temperaturama te je opisana numerička metoda računanja termalne matrice gustoće i svojstava kvantnih višečestičnih sustava. Na kraju, rezultati simulacija za Isingov model i model Rydbergovih atoma prikazani su u Poglavlju 8.5.

8.2 Matrica gustoće i prepletenost

Matrica gustoće, $\hat{\rho}$, je hermitska, pozitivno semidefinitna matrica koja predstavlja generalizaciju operatora projektora. Kada je sustav opisan vektorom stanja $|\psi\rangle$, matrica gustoće je jednaka projektoru na to stanje,

$$\hat{\rho} = |\psi\rangle \langle\psi| , \tag{8.1}$$

a za sustav se kaže da je u čistom stanju. S druge strane, ne može se svaki sustav povezati s dobro definiranim vektorom stanja. Pretpostavimo da imamo klasičnu distribuciju vjerojatnosti koja nam govori koliko je vjerojatno pronaći sustav u svakom od stanja $|\psi_j\rangle$. Za takav se sustav kaže da je u miješanom stanju. Odgovarajuću matricu gustoće definiramo kao:

$$\hat{\rho} = \sum_{j=1}^{D} p_j \, |\psi_j\rangle \langle\psi_j| , \tag{8.2}$$

gdje je p_j vjerojatnost dodijeljena stanju $|\psi_j\rangle$, s uvjetom normalizacije $\sum_{j=1}^{D} p_j = 1$. Treba primijetiti da se svako čisto stanje može napisati kao miješano stanje gdje su sve vjerojatnosti osim jedne jednake nuli: $p_i = 1, p_{j \neq i} = 0$. Maksimalno miješano stanje odgovara slučaju kada su sve vjerojatnosti jednake, $\forall p_j = 1/D$.

Matrica gustoće je prikladan način pohranjivanja svih dostupnih klasičnih i kvantnih informacija o sustavu. Može se pokazati da i za čista i za miješana stanja vrijedi:

$$\begin{aligned} \mathrm{Tr}(\hat{\rho}) &= 1, \\ \langle O \rangle &= \mathrm{Tr}(\hat{\rho}\hat{O}). \end{aligned} \tag{8.3}$$

Stoga je matrica gustoće matematički alat koji nam omogućuje računanje prosječnih veličina i svojstava sustava u miješanom stanju.

Za danu matrice gustoće, jednostavan način određivanja koliko je sustav blizu čistog stanja, jest izračunati njegovu čistoću, γ. Čistoća se definira kao:

$$\gamma(\hat{\rho}) = \mathrm{Tr}(\hat{\rho}^2). \tag{8.4}$$

Izraženo preko svojstvenih vrijednosti matrice gustoće, tj. vjerojatnosti p_j:

$$\gamma(\hat{\rho}) = \sum_{j=1}^{D} p_j^2. \tag{8.5}$$

Što je čistoća bliža 1, to je sustav bliži čistom stanju.

U ovome radu bavimo se proučavanjem bipartitnih mjera prepletenosti miješanih stanja. Prije nego uvedemo matematički formalizam prepletenosti i načina kojim ju možemo mjeriti, korisno je uvesti tzv. *reduciranu* matricu gustoće. Razmotrimo bipartitni sustav, tj. složeni sustav koji se sastoji od dva različita dijela A i B, opisanih matricom gustoće $\hat{\rho}_{AB}$. Pretpostavimo da nas ne zanima podsustav B i da želimo zadržati isključivo informacije dostupne o podsustavu A. Analogno integraciji zajedničke distribucije vjerojatnosti $P(x, y)$ preko jedne varijable koja nas ne zanima, reducirana matrica gustoće se dobiva kao parcijalni trag preko svih stanja podsustava B:

$$\hat{\rho}_A = \mathrm{Tr}_{\mathrm{B}}(\hat{\rho}_{AB}) = \sum_j \langle b_j| \, \hat{\rho}_{AB} \, |b_j\rangle \, , \tag{8.6}$$

gdje skup vektora $|b_j\rangle$ čini bazu Hilbertovog prostora podsustava B. Reducirana matrica gustoće $\hat{\rho}_A$ sadrži maksimalnu informaciju koju možemo imati o podsustavu A neovisno o B.

Koncept prepletenosti odnosi se na intrinzično kvantne korelacije između dvaju ili više fizikalnih sustava. Kao glavna briga poznatog EPR [34] paradoksa koji propituje potpunost kvantne teorije, isprepletenost je dugo vrijeme bila izvor čuđenja među znanstvenicima. Nakon što je odgovor na EPR paradoks stigao kroz Bellove nejednakosti [35], mnogi eksperimentalni i teorijski napori uloženi su u poboljšanje našeg razumijevanja kvantnih korelacija. No, prepletenost kao pojava koja određuje mikroskopsko ponašanje prirode nije samo neobična zanimljivost, štoviše - to je također i vrlo moćan resurs koji omogućuje konstruiranje novih, kvantnih tehnologija [36]. Danas nam eksperimentalni napredak omogućuje izolaciju, pripremu i kontrolu pojedinačnih kvantnih sustava, iskorištavajući njihovu prepletenost za razvoj algoritama i protokola sposobnih za rješavanje određenih zadataka mnogo brže od njihovih klasičnih analogona. Stoga je zadatak karakteriziranja i kvantificiranja prepletenosti od veoma velike važnosti.

Ako stanje nije prepleteno, kažemo da je separabilno. U slučaju složenog sustava u čistom stanju, ono je separabilno ako se može napisati kao tenzorski produkt stanja svakog od njegovih konstituenata. Dakle, separabilno stanje bipartitnog sustava AB

ima oblik:

$$|\psi\rangle = |\psi^A\rangle \otimes |\psi^B\rangle = (\sum_i A_i \, |a_i\rangle) \otimes (\sum_j B_j \, |b_j\rangle). \tag{8.7}$$

Gdje $|a_j\rangle$ i $|b_j\rangle$ čine bazu Hilbertovog prostora podsustava A, odnosno B. Pripadna matrica gustoće glasi:

$$\hat{\rho}_{AB} = |\psi^A\rangle \langle\psi^A| \otimes |\psi^B\rangle \langle\psi^B| \, . \tag{8.8}$$

Iz jednadžbe (8.8) može se zaključiti da, ako je čisto stanje dva sustava separabilno, pripadne reducirane matrice gustoće će također predstavljati čisto stanje. S druge strane, ako je stanje dva sustava prepleteno, pripadne reducirane matrice gustoće će odgovarati miješanim stanjima.

Definicija separabilnosti može se proširiti i na miješana stanja. Miješano stanje sistema AB je separabilno ako se njegova matrica gustoće može napisati kao:

$$\hat{\rho}_{AB} = \sum_j p_j \ |\psi_j^A\rangle \langle\psi_j^A| \otimes |\psi_j^B\rangle \langle\psi_j^B| = \sum_j p_j \ \hat{\rho}_j^A \otimes \hat{\rho}_j^B. \tag{8.9}$$

No, za proizvoljnu matricu gustoće $\hat{\rho}$ dekompozicija na skup (ne nužno ortonormiranih) stanja nije jedinstvena, a dokazivanje da dekompozicija kao u jednadžbi. (8.9) postoji ili ne postoji nije trivijalan zadatak. Zbog toga su nam za slučaj miješanih stanja potrebne kompleksnije mjere i kriteriji prepletenosti.

Prije definiranja nekih od mjera prepletenosti, potrebno je uvesti Von Neumannovu entropiju:

$$\mathcal{S}(\hat{\rho}) = -\mathrm{Tr}(\hat{\rho} \log \hat{\rho}) = -\sum_j p_j \log p_j. \tag{8.10}$$

Von Neumannova entropija predstavlja proširenje koncepta Gibbsove entropije iz klasične statističke mehanike, te je također i kvantni analogon Shannonove entropije iz teorije informacije. Von Neumannova entropija jednaka je nuli kada je stanje čisto, a maksimalna kada je stanje maksimalno miješano. Stoga, suprotno od čistoće (definirane u jednadžbi (8.4)), Von Neumannova entropija nam govori o stupnju miješanosti sustava.

Za složeni sustav AB u čistom stanju, entropije svakog od podsustava su jednake:

$$\mathcal{S}(\hat{\rho}_A) = \mathcal{S}(\hat{\rho}_B). \tag{8.11}$$

Za diskretnu raspodjelu vjerojatnosti $\{p_1, ..., p_n\}$, može se definirati i generalizacija entropije, tzv. Rényieva entropija reda α [25]:

$$\mathcal{S}_\alpha(\hat{\rho}) = \frac{1}{1-\alpha} \log \left(\sum_j p_j^\alpha \right). \tag{8.12}$$

U slučaju $\alpha \longrightarrow 1$, Rényieva entropija se podudara s Von Neumannovom entropijom. Pokazalo se da su Rényieve entropije korisne pri proučavanju termodinamike fraktalnih struktura [39].

Idući važan koncept su tzv. lokalne operacije i klasična komunikacija (eng. *local operations classical communication*, LOCC). Pretpostavimo da Alice i Bob dijele neki kvantni sustav, tako da se jedan dio sustava nalazi kod Alice, a drugi kod Boba. Lokalne operacije podrazumijevaju da Alice može izvoditi operacije (kao što su unitarne transformacije i mjerenja) samo na svom dijelu sustava, te Bob isto može raditi samo na svom. Klasična komunikacija implicira da Alice i Bob informacije mogu razmjenjivati isključivo na klasičan način. Na primjer, smiju međusobno razgovarati o rezultatima svojih mjerenja, ali ne smiju razmjenjivati kvantne sustave.

Važno ograničenje LOCC operacija je da one ne mogu stvoriti prepletenost u sustavu. Međutim, može se pokazati da koristeći LOCC jedno stanje sistema možemo transformirati u neko drugo proizvoljno stanje sistema. U slučaju da početno stanje odgovara jednom od maksimalno prepletenih stanja, tzv. Bellovih stanja, konverzija se može provesti sa stopostotnom sigurnošću. S druge strane, ukoliko je početno stanje proizvoljno, u većini slučajeva željenu konverziju ne možemo izvesti sa sigurnošću, već samo s određenom vjerojatnošću. Kako bi se prevladao ovaj problem, zgodno je proučiti malo općenitiju situaciju u kojoj se razmatra problem

$$\hat{\rho}^{\otimes n} \longrightarrow \hat{\sigma}^{\otimes m}, \tag{8.13}$$

odnosno transformiramo n kopija stanja $\hat{\rho}$ u m kopija stanja $\hat{\sigma}$. Najveći omjer m/n za koji se takva transformacija može postići govori nam o relativnom sadržaju isprepletenosti $\hat{\rho}$ i $\hat{\sigma}$. Ukoliko se odlučimo da je prihvatljivo dopustiti određeni stupanj neizvjesnosti, nesavršenosti konverzije se mogu proizvoljno smanjiti povećanjem n. Stoga je korisno razmotriti asimptotski režim u kojem $n \longrightarrow \infty$. Omjer m/n tada se može tumačiti kao asimptotski broj stanja $\hat{\sigma}$ koja se mogu pripremiti iz $\hat{\rho}$.

Uvodom u LOCC i transformacije stanja, postavili smo temelje za uvođenje nekih mogućih načina kvantificiranja isprepletenosti. Počinjemo s predstavljanjem tri aksioma [42], odnosno zahtjeva koje određena matematička veličina kojom predstavljamo prepletenost mora ispunjavati kako bi bila u skladu s fizikalnim konceptom prepletenosti. Ovi se aksiomi danas smatraju elementarnim uvjetima koje svaka mjera isprepletenosti, $E(\hat{\rho})$, mora zadovoljiti:

- $E(\hat{\rho}) = 0$ *za separabilna stanja,*
- $E(\hat{\rho})$ *se ne mijenja pri lokalnim unitarnim transformacijama,*

  jer lokalna unitarna transformacija predstavlja promjenu baze, a prepletenost ne ovisi o izboru baze.
- $E(\hat{\rho})$ *se ne može povećati pomoću LOCC.*

Postoji mnogo funkcija za koje je poznato da su u skladu s ovim zahtjevima, a u ovom radu uvodimo dvije od njih: prepletenost formacije, čija se fizička interpretacija nastavlja na priču o transformacijama stanja, i negativnost, kao strogo matematički pristup mjerenju isprepletenosti.

Međutim, preostaje još jedna fizikalna veličina, entropija prepletenosti, koju je potrebno objasniti prije definiranja prepletenost formacije i negativnosti. Entropija prepletenosti složenog sustava u čistom stanju AB definirana je kao:

$$\mathcal{S}_E(\hat{\rho}_{AB}) = \mathcal{S}(\hat{\rho}_A) = \mathcal{S}(\hat{\rho}_B), \tag{8.14}$$

gdje su $\hat{\rho}_A$ i $\hat{\rho}_B$ matrice reducirane gustoće podsustava A, odnosno B, a $\mathcal{S}(\hat{\rho})$ je Von Neumannova entropija. Jednostavna analiza jednadžbe (8.14) otkriva da $\mathcal{S}_E(\hat{\rho}_{AB})$

služi kao mjera prepletenosti između podsustava A i B za čista stanja: prisjećajući se rasprave o Von Neumannovoj entropiji, znamo da ona mjeri stupanj mješanosti matrice gustoće. Također znamo da, ako je čisto stanje separabilno, njegove reducirane matrice gustoće biti će čista stanja, a ako je stanje prepleteno, reducirane matrice gustoće biti će miješana stanja. Stoga slijedi da stupanj miješanosti reducirane matrice gustoće (a time i $\mathcal{S}_E(\hat{\rho}_{AB})$) izravno ukazuje na količinu prepletenosti u sustavu.

Međutim, iako entropija prepletenosti u potpunosti karakterizira bipartitne kvantne korelacije čistog stanja, slučaj miješanog stanja opet se razumije mnogo slabije i zahtijeva složenije metode. Ne postoji jedinstveni način karakterizacije prepletenosti miješanog stanja, već su konstruirane različite mjere s različitim fizikalnim interpretacijama.

Sada predstavljamo prepletenost formacije kao jedan pristup generalizaciji koncepta entropije prepletenosti na miješana stanja. Prepletenost formacije definira se kao:

$$E_F(\hat{\rho}) = \inf_{\psi_j, p_j} \Big\{ \sum_j p_j \mathcal{S}_E(|\psi_j\rangle) \quad : \quad \hat{\rho} = \sum_j p_j \left|\psi_j\right\rangle \left\langle\psi_j\right| \Big\}, \tag{8.15}$$

i predstavlja minimalnu prosječnu entropiju prepletenosti nad svim dekompozicijama stanja $\hat{\rho}$ [26]. Motivacija iza naziva ”prepletenost formacije” jest da se očekuje da je ova veličina usko povezana s tzv. troškom prepletenosti, odnosno asimptotskim brojem maksimalno prepletenih parova (Bellovih parova) potrebnih za pripremu određenog stanja. Izračunavanje prepletenosti formacije nije jednostavan zadatak, a analitička rješenja jednadžbe (8.15) pronađena su samo za nekoliko posebnih slučajeva (npr. za stanja dva kubita [44]). Stoga se iznosu prepletenosti formacije općenitog stanja može pristupiti isključivo putem numeričkih izračuna.

Iduća bipartitna mjera prepletenosti naziva se negativnost. Ona se temelji na Peres-Horodecki kriteriju, poznatom i pod nazivom kriterij pozitivnog parcijalnog transponata (eng. *positive partial transpose*, PPT). PPT kriterij glasi: ako je sustav $\hat{\rho}_{AB}$ separabilan, tada će matrica gustoće parcijalno transponirana u odnosu na jedan dio sustava, $\hat{\rho}^{T_A}$, imati sve nenegativne svojstvene vrijednosti. Stoga, ako je jedna ili više svojstvenih vrijednosti $\hat{\rho}^{T_A}$ negativna, stanje nije separabilno. Ovaj se uvjet koristi za konstruiranje mjere prepletenosti negativnosti, koja je definirana kao:

$$\mathcal{N}(\hat{\rho}) = \frac{\|\hat{\rho}^{T_A}\|_1 - 1}{2}, \tag{8.16}$$

gdje je $\|X\|_1$ norma traga, $\|X\|_1 = Tr(\sqrt{X^\dagger X})$. Treba napomenuti da vrijednost negativnosti ne ovisi izboru podsustava u odnosu na kojega je matrica gustoće transponirana, odnosno negativnost se može definirati i zamjenom $\hat{\rho}^{T_A} \longrightarrow \hat{\rho}^{T_B}$ u jednadžbi (8.16).

Opremljeni svim teorijskim preduvjetima, sada možemo nastaviti na problem numeričkih izračuna predstavljenih svojstava za višečestične kvantne sustava u miješanom stanju.

8.3 Mreže tenzora

U ovome poglavlju ukratko ćemo predstaviti metode mreža tenzora (eng. *Tensor Network Methods*, TNM) [21, 22] - klasu numeričkih metoda koje su se pokazale uspješnim u izbjegavanju (do neke mjere) prepreke eksponencijalnog skaliranja računalne složenosti kvantnih problema više tijela.

TNM se oslanjaju na dekompoziciju kvantnih objekata, kao što su vektori stanja i operatori, na mreže tenzora različitih oblika i struktura. Kako bi ukratko objasnili temeljnu ideju iza ovih metoda, počinjemo s definicijom tenzora i grafičke notacije. Tenzor ranga N je matematički objekt s N indeksa. Primjerice, skalar je tenzor ranga 0, vektor je tenzor ranga 1, a matrica je tenzor ranga 2. Mreža tenzora je skupina tenzora koji međusobno mogu biti povezani kontrakcijama indeksa. Kontrakcije indeksa podrazumijevaju sumaciju elememata tenzora po određenom indeksu, primjerice množenje dviju matrica, **A** i **B**, implicira kontrakciju s obzirom na unutarnji indeks: $C_{ij} = \sum_k A_{ik} B_{kj}$. S obzirom da iz matematičkih izraza tenzorskih mreža često nije jednostavno uočiti strukturu odnosa između tenzora u mreži, sa svrhom pojednostavljenja se uvodi prikladna grafička notacija. Unutar ove notacije, tenzor je označen određenim oblikom, primjerice krugom ili kockom, a njegovi indeksi su prikazani crtama, tzv. nogama, koje izlaze iz tog oblika. Kontrakcija određenih indeksa prikazuje se linijom koja spaja dva tenzora koji se kontrahiraju. Kao primjer, na Slici 8.5 prikazana je operacija množenja matrica. Na analogan način mogu se konstruirati i složenije mreže tenzora.

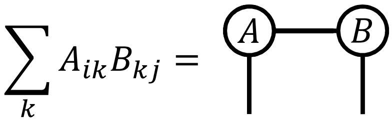

Slika 8.5: Grafički prikaz operacije množenja matrica **A** i **B**. Tenzor je označen krugom, a njegovi indeksi nogama koje izlaze iz kruga. Matrica sadrži dva indeksa te stoga pripadni tenzor ima dvije noge. Operacija množenja matrica podrazumijeva kontrakciju (sumaciju) po indeksu k, stoga noge tenzora koje odgovaraju indeksu k povezuju tenzore matrica **A** i **B**.

Nadalje, potrebno je objasniti elementarne manipulacije i operacije nad tenzorima: spajanje i razdvajanje indeksa te singularnu dekompoziciju matrica (eng. *singular value decomposition*, SVD). Multidimenzionalnost tenzora može se promatrati kao alat za organizaciju informacije na strukturiran način. Primjerice, elemente A_k vektora s četiri komponente može se reorganizirati u 2×2 matricu s elementima A_{ij}. Drugim riječima, jedan indeks tenzora možemo razdvojiti na dva indeksa bez ikakvog gubitka informacije. Općenitije, bilo koji tenzor ranga N i dimenzija $D_1 \times D_2 \times ... \times D_N$ može se preoblikovati u tenzor ranga N' i dimenzija $D'_1 \times D'_2 \times ... \times D'_{N'}$, uz uvjet da produkt dimenzija tenzora, tj. ukupni broj elemenata tenzora ostane nepromijenjen. U slučaju kada se dva ili više indeksa preoblikuju u jedan indeks, govorimo o spajanju indeksa, a u obrnutom slučaju, kada se jedan indeks razdvaja na dva ili više indeksa, govorimo o razdvajanju indeksa. Primjer razdvajanja i spajanja indeksa dan je na Slici 8.6.

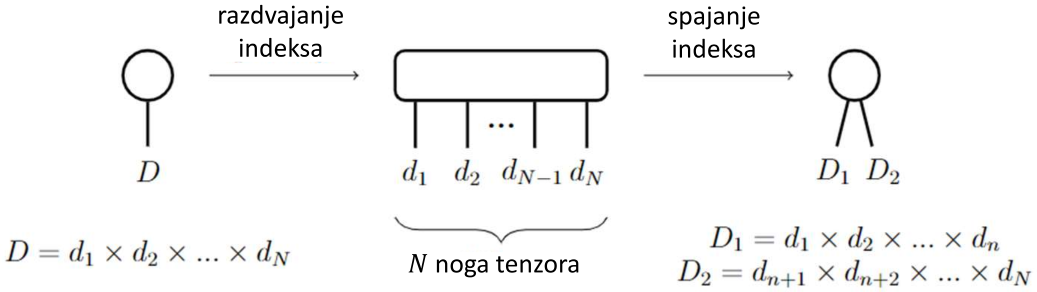

Slika 8.6: Primjer razdvajanja i spajanja indeksa.

SVD je faktorizacija matrice na produkt triju matrica:

$$A_{ij} = \sum_{k=1}^{K} S_{ik} V_{kk} D_{kj}, \qquad K = min(L, M), \tag{8.17}$$

gdje su **S** $\in \mathbb{C}^{L\times K}$ i **D** $\in \mathbb{C}^{K\times M}$ unitarne, a **V** $\in \mathbb{R}^{K\times K}$ dijagonalna, realna i pozitivna matrica. Vrijednosti na dijagonali matrice **V** nazivaju se singularne vrijednosti. SVD je važan alat iz dva razloga: prvo, s obzirom da omogućuje rastav jedne matrice na više matrica, koristi se za manipuliranje strukturom mreža tenzora. Bitno je primjetiti da, s obzirom da se svaki tenzor prikladnih dimenzija može razdvajanjem ili spajanjem indeksa preoblikovati u matricu, u praksi pomoću SVD možemo rastavljati i tenzore koji prvotno nisu bili matrice. Iduća važnost SVD-a proizlazi iz činjenice da ova dekompozicija omogućava kompresiju informacije, odnosno odbacivanje najmanje relevantnog dijela informacija sadržanih u matrici. Na singularne vrijednosti može se gledati kao na faktori težine koji određuju koja je informacija relevantna, a koja nije. Pretpostavimo da su vrijednosti na dijagonali matrice **V** poredane silazno po veličini. Zadržavanjem samo prvih m najvećih singularnih vrijednosti, matricu A aproksimiramo kao:

$$A_{ij} \approx \sum_{j=1}^{m} S_{ik} V_{kk} D_{kj}. \tag{8.18}$$

Na ovaj način, pogreška nastala odbacivanjem singularnih vrijednosti može se u potpunosti kontrolirati i pratiti, što u praksi omogućuje drastično smanjenje dimenzija matrica. S obzirom da najveći problem simulacija višečestičnih kvantnih sustava proizlazi iz prevelikih dimenzija objekata s kojima radimo, TNM koriste SVD kao glavni mehanizam za konstrukciju efikasnih algoritama.

Kvantna valna funkcija N čestica može se zapisati na sljedeći način:

$$|\psi\rangle = \sum_{\alpha_1\alpha_2\ldots\alpha_N} C_{\alpha_1\alpha_2\ldots\alpha_N} |\psi_{\alpha_1}\rangle \otimes |\psi_{\alpha_2}\rangle \otimes \ldots \otimes |\psi_{\alpha_N}\rangle, \tag{8.19}$$

gdje je $\alpha_n = 1, 2, \ldots, d_n$, a d_n je dimenzija lokalnog Hilbertovog prostora n-te čestice. Radi jednostavnosti, pretpostavljamo da se sve čestice nalaze u lokalnom Hilbertovom prostoru iste dimenzije d. Stoga, potrebno je d^N koeficijenata za opisivanje generičkog kvantnog stanja N-čestica.

Ukoliko je stanje separabilno, valna funkcija glasi:

$$\begin{aligned} |\psi\rangle &= |\Psi_1\rangle \otimes |\Psi_2\rangle \otimes \ldots \otimes |\Psi_N\rangle \\ &= \Big(\sum_{\alpha_1} C_{\alpha_1} |\psi_{\alpha_1}\rangle\Big) \otimes \Big(\sum_{\alpha_2} C_{\alpha_2} |\psi_{\alpha_2}\rangle\Big) \otimes \ldots \otimes \Big(\sum_{\alpha_N} C_{\alpha_N} |\psi_{\alpha_N}\rangle\Big). \end{aligned} \tag{8.20}$$

Umjesto d^N koeficijenata u slučaju općeg stanja, za opisivanje separabilnog stanja potrebno je $N \cdot d$ koeficijenata. Stoga, uz pretpostavku da ne postoje kvantne korelacije između čestica, skaliranje veličine objekta potrebnog za pohranjivanje informacija o stanju smanjuje se s eksponencijalne na linearnu ovisnost o broju čestica. Međutim, unatoč vrlo primamljivoj redukciji na linearno skaliranje, tretiranje fizičkog sustava kao potpuno separabilnog, tj. u aproksimaciji srednjeg polja, ima svoja ograničenja. Ideja mreže tenzora je prepoznavati i očuvati samo važne korelacije čestica i na taj način zadržati dimenzije kvantnih objekata razumno niskim.

Pomoću prethodno opisanih manipulacija i operacija nad tenzorima (spajanje i razdvajanje indeksa te SVD), vektor kvantnog stanja može se preoblikovati u razne oblike mreža tenzora. Bez ulaženja u previše detalja, sada ćemo predstaviti dva oblika mreža tenzora kojima možemo opisati vektore stanja: stanja matričnog produkta (eng. *matrix product states*, MPS) [16] i stablaste mreže tenzora (eng. *tree tensor networks*, TTN) [29]. Grafički, na Slici 8.7 na primjeru sustava s $N = 4$ čestice prikazani su vektor stanja iz jednadžbe (8.19) (Slika 8.7a), separabilni vektor stanja iz jednadžbe (8.20) (Slika 8.7b), te MPS oblik (Slika 8.7c) i TTN oblik (Slika 8.7d). Svaki od tenzora MPS vektora stanja odgovara jednoj čestici. Može se pokazati da linije koje povezuju različite čestice predstavljaju kvantne korelacije. Separabilno stanje je rubni slučaj MPS-a u kojemu kvantne korelacije ne postoje. Koristeći SVD kompresiju, dimenzije indeksa koji povezuju tenzora u MPS obliku ograniče se na određenu vrijednost m. S druge strane, u slučaju TTN vektora stanja, fizikalnim česticama odgovaraju tenzori u najdonjem sloju. Svaka od nogu tenzora u najdonjem sloju TTN-a odgovara jednoj čestici, odnosno svaki tenzor predstavlja dvije čestice. Kao i kod MPS-a, i linije između tenzora u TTN obliku predstavljaju kvantne korelacije. No, za razliku od MPS-a koji pruža uvid u kvantne korelacije među susjednim česticama, TTN nam daje informaciju o korelacijama između bipartitnih podjela sistema.

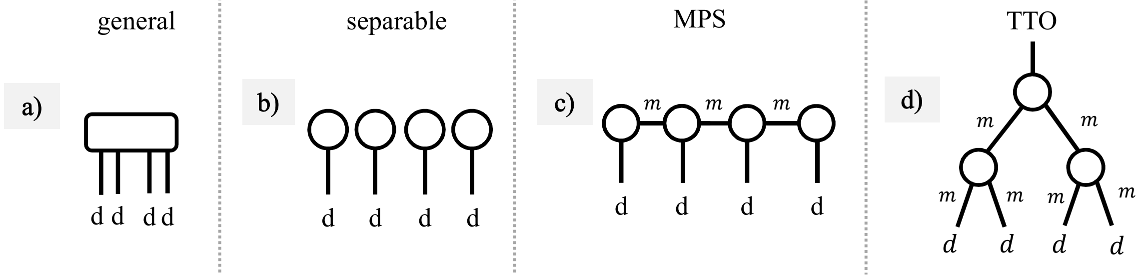

Slika 8.7: Različiti oblici vektora stanja za $N = 4$ čestica.

Međutim, MPS i TTN ovdje predstavljaju čista stanja. Za opis miješanih stanja potreban je operator matrice gustoće. U tu svrhu mogu se konstruirati operatori analogni MPS-u i TTN-u. U ovome radu istražujemo tzv. operatore stablastih mreža tenzora (eng. *tree tensor operators*, TTO), za koje ćemo pokazati da su veoma korisni pri izračunavanju svojstava kvantnih sustava na konačnim temperaturama. Osim TTO, u numeričkoj metodi koristit ćemo i lokalno pročišćene mreže tenzora (eng. *locally purified tensor networks*, LPTN). Prije nego predstavimo ova dva oblika, bitno je spomenuti da je matrica gustoće po definiciji pozitivno semidefinitni operator te se stoga može rastaviti kao:

$$\hat{\rho} = \sum_{j=1}^{K_0} p_j \left|\psi_j\right\rangle \left\langle\psi_j\right| = XX^\dagger, \tag{8.21}$$

pri čemu je X_j unitarna matrica sa stupcima jednakim $\sqrt{p_j}\left|\psi_j\right\rangle$. Broj stupaca, K_0, jednak je rangu ρ. Matrica gustoće rastavljena kao $XX^\dagger$, te LPTN i TTO oblik, su prikazani na Slici 8.8. Treba istaknuti da je kod LPTN i TTO svaka od strana, kao što je naznačeno na Slici 8.8, dobivena transformacijama matrice X, odnosno $X^\dagger$. Stoga je pri radu s ovim oblicima mreža tenzora dovoljno pohraniti tenzore samo jedne od strana, dok su elementi tenzora druge strane jednostavno kompleksni konjugati.

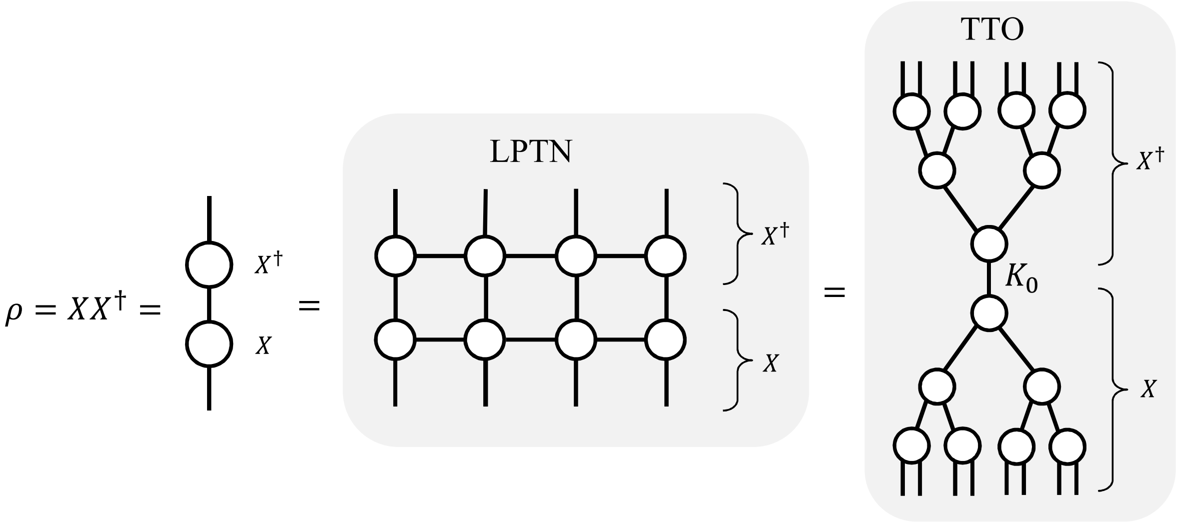

Slika 8.8: Operator matrice gustoće može se rastaviti na produkt matrica X i $X^\dagger$. Na slici je operator matrice gustoće grafički prikazan u obliku produkta matrica X i $X^\dagger$, u obliku lokalno pročišćene mreže tenzora (LPTN) i u obliku operatora stablastih mreža tenozra (TTO). Kao što je naznačeno, u LPTN i TTO obliku svaka od strana mreže tenzora odgovara transformiranim matricama X, odnosno $X^\dagger$. Linija (odnosno indeks) koja povezuje dvije strane TTO operatora matrice gustoće odgovara sumi po indeksu j iz jednadžbe (8.21) te je njezina dimenzija jednaka K_0.

U slučaju TTO oblika matrice gustoće, linija koja povezuje dvije strane operatora odgovara sumi po indeksu j iz jednadžbe (8.21). Stoga, imamo uvid u fizikalno značenje te linije, što će se pokazati ključnim pri tretiranju kvantnih sustava na konačnim temperaturama.

8.4 Algoritmi za kvantne sustave na konačnoj temperaturi

U ovome radu proučavamo sustave u termalnoj ravnoteži, što odgovara kanonskom ansamblu. Za kanonski ansambl može se izvesti odgovarajuća distribucija vjerojatnosti (vidi npr. [49]), te se svakoj konfiguraciji s ukupnom energijom E_j može dodijeliti vjerojatnost pronalaženja sustava u toj konfiguraciji, p_j:

$$p_j = \frac{1}{Z} e^{-\beta E_j}, \quad Z = \sum_i e^{-\beta E_i}, \quad \beta = \frac{1}{k_B T}. \tag{8.22}$$

Normalizacijski faktor Z naziva se particijska funkcija, a $k_B = 1,380649 \cdot 10^{-23}$ JK^{-1} je Boltzmannova konstanta. Temperatura je označena s T. U kvantnom slučaju, svaka energija E_j pripada određenom kvantnom stanju $|\psi_j\rangle$. Uzimajući u obzir da su p_j klasične vjerojatnosti pronalaska sustava u svakom od kvantnih stanja $|\psi_j\rangle$, možemo prepoznati da kanonski ansambl odgovara miješanom stanju s matricom gustoće:

$$\hat{\rho} = \sum_j \frac{e^{-\beta E_j}}{Z} |\psi_j\rangle \langle\psi_j| = \frac{e^{-\beta \hat{H}}}{Z}, \tag{8.23}$$

gdje je $\hat{H}$ Hamiltonijan sustava.

Treba primjetiti da vjerojatnosti opadaju eksponencijalno s energijom sustava, a brzina opadanja ovisi o temperaturi sustava. Pri niskim temperaturama, opadanje vjerojatnosti je vrlo brzo te su vjerojatnosti pronalaska sustava u visokoenergetskim stanjima zanemarive. Stoga, pri niskim temperaturama samo nekoliko prvih niskoenergetskih stanja doprinosi matrici gustoće. U limitu $T \longrightarrow 0$ sustav kolapsira u osnovno stanje. Ako je osnovno stanje nedegenerirano u energiji, sustav s nultom temperaturom bit će čisto stanje. Ako je osnovno stanje n-struko degenerirano, stanje će biti koherentna superpozicija prvih n stanja. Povećanje temperature povećava vjerojatnost pronalaska sustava u stanjima više energije. U granici $T \longrightarrow \infty$, sustav se približava maksimalno miješanom stanju, gdje sva stanja jednako doprinose s vjerojatnošću $1/d^N$.

Kvantni sustavi na konačnoj temperaturi u potpunosti su opisani svojim operatorom matrice gustoće. Jednom kada izračunamo ovaj operator za kvantni sustav, možemo ga koristiti za proučavanje različitih svojstava. Međutim, pronalaženje termalne matrice gustoće višečestičnog kvantnog sustava nije nimalo lak zadatak.

Osnovni cilj ovoga rada bio je razviti i testirati metodu temeljenu na TNM kojom možemo izračunati termalnu matricu gustoće višečestičnih kvantnih sustava u TTO obliku. Kao što ćemo pokazati, TTO oblik je veoma prikladan za smanjivanje računske kompleksnosti računanja svojstava sustava na konačnim temperaturama. Naša metoda za pronalaženje matrice gustoće sastoji se od dva koraka. Prvo računamo matricu gustoće u LPTN obliku razvijajući je prema imaginarnoj vremenskoj evoluciji, a zatim je pretvaramo u TTO.

Svi kodovi za nadalje opisane numeričke algoritme izrađeni su u sklopu ovog istraživanja i nalaze se u PY_API_QUANTUM_TEA_LEAVES Python biblioteci. Izuzetak je algoritam imaginarne vremenske evolucije, koji je već implementiran unutar Fortran biblioteke QUANTUM_GREEN_TEA. Obje su biblioteke razvijene unutar istraživačke grupe Quantum na Sveučilištu u Padovi i licencirane su pod licencom Apache, verzija 2.0.

Imaginarna vremenska evolucija oslanja se na činjenicu da, s obzirom da se sustav pri beskonačnoj temperaturi nalazi se u maksimalno miješanom stanju, njegova matrica gustoće je proporcionalna matrici identiteta. Stoga, uvijek ju možemo umetnuti u definiciju proizvoljne termalne matrice gustoće iz jednadžbe (8.23) na sljedeći način:

$$\hat{\rho} = \frac{e^{-\beta\hat{H}}}{Z} = \frac{1}{Z}e^{-\frac{\beta}{2}\hat{H}}\mathbb{1}e^{-\frac{\beta}{2}\hat{H}} = \frac{N}{Z}e^{-\frac{\beta}{2}\hat{H}}\hat{\rho}_{\infty}e^{-\frac{\beta}{2}\hat{H}} = \frac{N}{Z}e^{-\frac{\beta}{2}\hat{H}}\hat{\rho}_{\infty}(e^{-\frac{\beta}{2}\hat{H}})^{\dagger}. \tag{8.24}$$

U posljednjem izrazu iz jednadžbe (8.24) prepoznajemo oblik unitarne vremenske evolucije operatora matrice gustoće, $e^{-\frac{\mathrm{i}t}{\hbar}\hat{H}}\hat{\rho}(0)(e^{-\frac{\mathrm{i}t}{\hbar}\hat{H}})^{\dagger}$, sa zamjenom $\mathrm{i}t/\hbar \to \beta/2$. Stoga, da bismo dobili matricu gustoće na proizvoljnoj temperaturi, uz odgovarajuću supstituciju varijabli možemo razviti maksimalno miješanu matricu gustoće koristeći uobičajene algoritme za evoluciju operatora u vremenu. Postupak se naziva *imagi-*

narna vremenska evolucija. Biramo jedinice $k_B = 1$ i $\hbar = 1$.

Međutim, u slučaju višečestičnih kvantnih sustava, operacija vremenske evolucije nije trivijalna operacija. U ovome radu zanimaju nas lokalne interakcije između najbližih susjeda te razmatramo vremenski neovisan Hamiltonian oblika:

$$\hat{H} = \sum_{j=1}^{N} \hat{A}_i + \sum_{j=1}^{N-1} \hat{B}_j \hat{C}_{j+1}, \tag{8.25}$$

gdje su $\hat{A}_j$, $\hat{B}_j$, $\hat{C}_j$ proizvoljni lokalni operatori koji djeluju na česticu j. Članovi u drugoj sumi iz jednadžbe (8.25) predstavljaju interakcije između najbližih susjeda. Za izvođenje vremenske evolucije iskorištavamo LPTN oblik matrice gustoće i koristimo tzv. vremensko evoluirajući blok-decimalni algoritam (eng. *time evolving block decimation*, TEBD) opisan u [32,47]. Preciznost ove metode određena je parametrom diskretizacije vremena dt i maksimalnom dopuštenom dimenzijom indeksa u LPTN matrici gustoće, m_{LPTN}. Dimenzija m_{LPTN} predstavlja broj zadržanih singularnih vrijednosti u SVD tijekom čitavog postupka TEBD algoritma.

Kada dobijemo LPTN oblik matrice gustoće, pretvaramo ju u TTO. Postupak konverzije za slučaj $N = 4$ čestica prikazan je na Slici 8.9. Poopćenje na sustave većih veličina dobiva se iteracijom opisanog postupka.

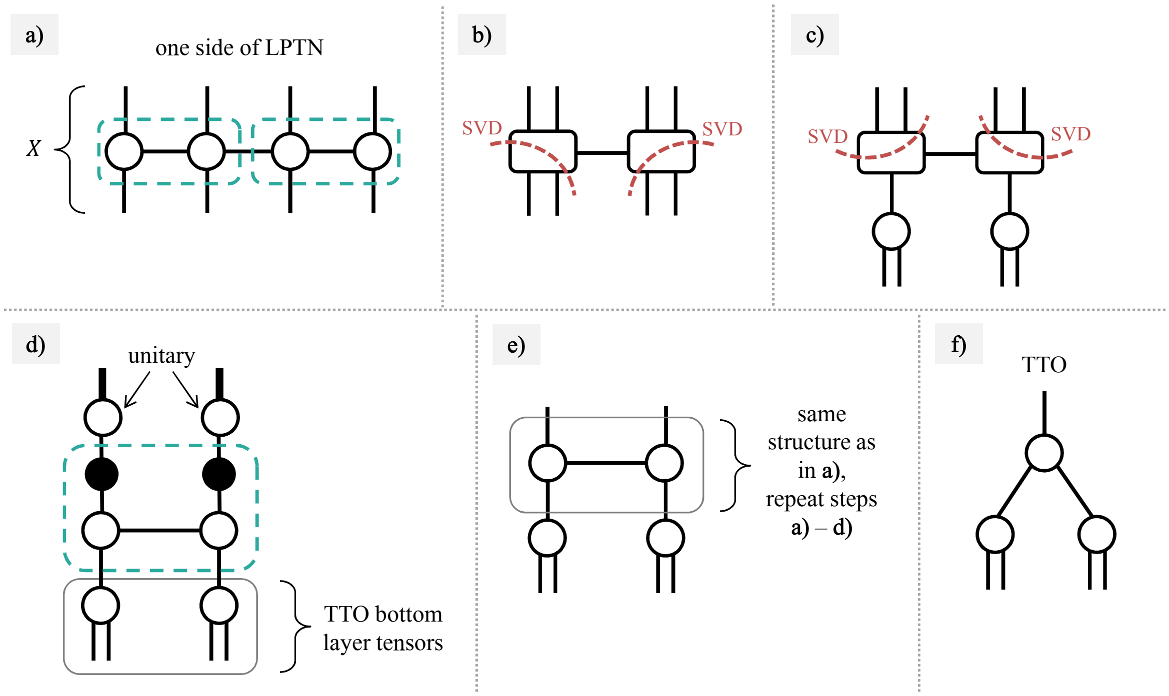

Slika 8.9: Pretvorba iz lokalno pročišćene mreže tenzora u operator stablaste mreže tenzora na primjeru $N = 4$ čestice. a) Dovoljno je raditi samo s jednom stranom LPTN (ili TTO), jer je druga strana njen hermitski konjugat. Tenzore LPTN-a dijelimo u parove i kontrahiramo preko unutarnje veze između sparenih tenzora. Tenzori koje kontrahiramo uokvireni su zelenom crtkanom linijom. Dobivamo mrežu tenzora kao na b). Idući korak je preoblikovati tenzor da dobijemo matricu. U jedan indeks matrice spajamo donje noge, a u drugi vezu koja povezuje različite parove i gornje noge, kao što je označeno crvenom crtkanom crtom. Zatim izvodimo SVD na svakoj od matrica i zadržavamo m_{TTO} najvećih singularnih vrijednosti, tj. reduciramo dimenzije dobivenih matrica. Dijagonalnu matricu kontrahiramo s gornjom unitarnom matricom. Ponovno razdijelimo sve noge tenzora te dobivamo mrežu tenzora kao na c). Donji tenzori predstavljaju donji sloj TTO-a. Da bismo stvorili temelj za izgradnju sljedećeg sloja, sve gornje tenzore ponovno preoblikujemo u matrice kao što je naznačeno crvenom crtom te izvodimo SVD dobivene matrice i skraćujemo dimenzije veze. Dolazimo do oblika prikazanog na d). Dijagonalnu matricu (označena crnom bojom) množimo s donjim tenzorima. Prema definiciji SVD, gornja matrica je unitarna. Budući da cjelokupna matrica gustoće sadrži i hermitski konjugirani dio kontrahiran preko gornjih veza, možemo zanemariti gornje unitarne matrice jer one kontrahine sa svojim hermitskim konjugatima daju matricu identiteta. Stoga dobivamo oblik kao e). Tenzori na gornjem sloju slike e) imaju oblik LPTN s upola manje čestica. Stoga ponavljamo postupak za izgradnju ostalih TTO slojeva te dobivamo f). Tijekom čitave procedure, određena je dimenzija m_{TTO} koja predstavlja broj zadržanih singularnih vrijednosti tijekom SVD. Izuzetak je posljednji SVD, koji određuje broj pobuđenih energetskih stanja zadržan u matrici gustoće. Za posljednji SVD, odabrana je zasebna dimenzija K_0.

Sada se nameće pitanje, koja je prednost TTO matrice gustoće u usporedbi s LPTN oblikom? Odgovor je u kombinaciji dviju značajki TTO-a - fizikalno značenje veze koja povezuje X i $X^\dagger$ strane TTO-a te najgornji tenzor kao centar izometrije.

O prvoj točki već je bilo riječi - TTO matrica gustoće sadrži vezu čija kontrakcija predstavlja zbroj stanja i odgovarajućih vjerojatnosti u matrici gustoće. U općenitom slučaju, s obzirom da ova suma ide preko kompletnog skupa stanja, dimenzija tog indeksa raste eksponencijalno s veličinom sustava, $K_0 = d^N$. To je prepreka, budući da je početna ideja TNM-a izbjegavanje rada s objektima eksponencijalno skalirajućih dimenzija. Međutim, u sustavima na konačnoj temperaturi, vjerojatnosti opadaju eksponencijalno s energijom stanja. Stoga nam TTO oblik omogućuje izravno poboljšanje učinkovitosti algoritma u niskotemperaturnom području odbacivanjem visokoenergetskih stanja, što čini simulacije na konačnim temperaturama moguće.

Što se tiče druge prednosti TTO-a, svaka mreža tenzora može biti izometrizirana, odnosno može se preoblikovati tako da su svi tenzori osim jednog, unitarni (vidi [51]). Kada je TTO matrica gustoće izometrizirana s centrom izometrije u najgornjem tenzoru strane X (i analogno, najdonjem tenzoru strane $X^\dagger$), sve informacije o vjerojatnostima p_j završavaju pohranjene unutar tog tenzora. Također, može se pokazati da će najgornji tenzor u tom slučaju sadržavati svu informaciju o bipartitnoj prepletenosti. Stoga, umjesto rukovanja matricom gustoće eksponencijalno skalirajućih dimenzija, relevantne informacije komprimirane su u jedan tenzor, R, čije dimenzije možemo kontrolirati (Slika 8.10). Vjerojatnosti p_j su jednake korijenu singularnih vrijednosti tenzora R preoblikovanog u matricu na način da donje noge (gledajući Sliku 8.10) pripadaju jednom indeksu, a gornja noga pripada drugom indeksu. Čistoća, Von Neumannova entropija, Rényijeve entropije i negativnost izračunavaju se koristeći dobivene vjerojatnosti p_j, a negativnost direktno iz definicije (8.16) zamjenom $X \longrightarrow R$. Račun prepletenosti formacije je kompliciraniji zbog toga što zahtijeva minimizaciju određene veličine nad različitim dekompozicijama matrice gustoće. Postupak kojim smo izračunali prepletenost formacije opisan je u [30].

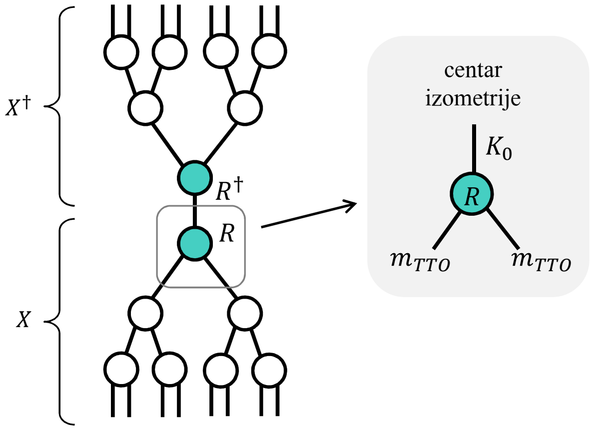

Slika 8.10: Izometrizirana TTO matrica gustoće. Tenzor centra izometrije je označen plavom bojom. S obzirom da se TTO matrica gustoće sastoji od dva međusobno Hermitski konjugirana dijela, X i $X^\dagger$, u izračunima je dovoljno raditi samo s jednom stranom. Sva informacija o termalnim vjerojatnostima i bipartitnoj prepletenosti pohranjena je u tenzoru R, čije dimenzije možemo kontrolirati. Dimenzije tenzora R naznačene su na slici desno.

8.5 *Fizikalni modeli*

Opisanu numeričku metodu testirali smo na dva jednodimenzionalna fizikalna modela - Isingov model i model Rydbergovih atoma. Prvo ćemo predstaviti rezultate za Isingov modela, a nakon toga rezultate za model Rydbergovih atoma. Simulacije su napravljene za sustave veličina $N = 8$, 16 i 32.

Isingov model je dobro poznati model koji opisuje feromagnetsko i paramagnetsko ponašanje kvantnih spinova u lokalnoj interakciji u vanjskom magnetskom polju. Jednodimenzionalni slučaj ovoga modela zanimljiv je jer manifestira kvantni fazni prijelaz. Slično klasičnom faznom prijelazu, gdje mala promjena parametra, kao što je temperatura, izaziva naglu promjenu svojstava sustava, kvantni fazni prijelaz podrazumijeva da mala varijacija parametra rezultira drastičnom promjenom svojstava osnovnog stanja. Razmatramo Isingov model najbližih susjeda s otvorenim rubnim uvjetima, opisan Hamiltonijanom:

$$\hat{H} = -J\Big(\sum_{i=1}^{N-1} \sigma_x^i \sigma_x^{i+1} + \lambda \sum_{i=1}^{N} \sigma_z^i\Big) \tag{8.26}$$

Hamiltonijan se sastoji od dva člana: $\sigma_x^i \sigma_x^{i+1}$, koji opisuje međučestične dipolne interakcije, i σ_z^i, koji predstavlja interakciju s vanjskim poljem. Odnos jačina ta dva doprinosa određen je parametrom λ, koji igra ulogu jakosti vanjskog polja. Parametar

J određuje energetsku skalu Hamiltonijana.

Promatranjem Hamiltonijana iz jednadžbe (8.26) može se predvidjeti postojanje dvaju režima u Isingovom modelu. S jedne strane, pri slabom vanjskom polju, vodeći doprinos dolazi od interakcijskog dijela Hamiltonijana te očekujemo da će sustav favorizirati poravnanje spinova najbližih susjeda u istom smjeru duž x-osi. S druge strane, kada je vanjsko polje jako, očekujemo poravnanje spinova u smjeru vanjskog polja duž z-osi.

Na temperaturi apsolutne nule, sustav je u osnovnom stanju. Za mali λ, osnovno stanje je dvostruko degenerirano. Dva stanja odgovaraju sustavu sa svim spinovima poredanim duž jednog od dva smjera x-osi. Budući da je poravnanje spina posljedica međučestičnih interakcija, sustav je u feromagnetskoj fazi. Oko $\lambda \approx 1$ dolazi do loma simetrije osnovnog stanja i sustav prolazi kroz kvantni fazni prijelaz iz feromagnetske u paramagnetsku fazu. U paramagnetskoj fazi, tj. slučaju velikog λ, osnovno stanje više nije degenerirano te ono odgovara sustavu sa svim spinovima usmjerenim u smjeru z-osi. U termodinamičkoj granici, kvantni fazni prijelaz događa se točno na $\lambda_c = 1$, te stoga ta točka predstavlja kritičnu točku sustava.

Pri konačnoj temperaturi, pobuđena energetska stanja počinju doprinositi matrici gustoće, tj. sustav postaje smjesa više kvantnih stanja. Stoga, za analizu o ponašanju sustava potrebno je uzeti u obzir i viša energetska stanja. Budući da se učinkovitost našeg numeričkog algoritma smanjuje s povećanjem brojem doprinosećih stanja, fokusiramo se na niskotemperaturni raspon.

Slika 8.11 ovisnost izračunate čistoće o parametru λ i temperaturi T. Budući da čistoća izravno govori o stupnju mješavine sustava, ona predstavlja informaciju o broju stanja koja doprinose matrici gustoće. U feromagnetskoj fazi, kada je stanje mješavina dvaju degeneriranih osnovnih stanja, čistoća je $\gamma(\hat{\rho}) = 0,5^2 + 0,5^2 = 0,5$. U paramagnetskoj fazi stanje je čisto, stoga je čistoća jednaka 1. Dvije su faze jasno vidljive na sl. 8.11. Zbog postojanja većeg energetskog procijepa između osnovnog i pobuđenih stanja u spektru Isingovog modela, ove faze ostaju robusnije s temperaturom što je vrijednost parametra λ dalje od $\lambda_c = 1$. Između feromagnetske i paramagnetske faze primjećujemo neuređenu fazu koja je posljedica konačne temperature. Također vidimo da s povećanjem broja čestica feromagnetska i paramagnetska faza postaju manje otporne na temperaturne učinke.

Slika 8.12 prikazuje $\lambda - T$ mrežu za Von Neumannovu entropiju. Opet se mogu razlikovati iste faze, a entropija raste kako sustav postaje mješovitiji. Slika 8.13 prikazuje mjeru prepletenosti negativnost. Može se primijetiti da je prepletenost najveća oko kritične točke te da opada s temperaturom. Kako se veličina sustava povećava, prepletenost postaje sve koncentriranija prema kritičnoj točki na nultoj temperaturi.

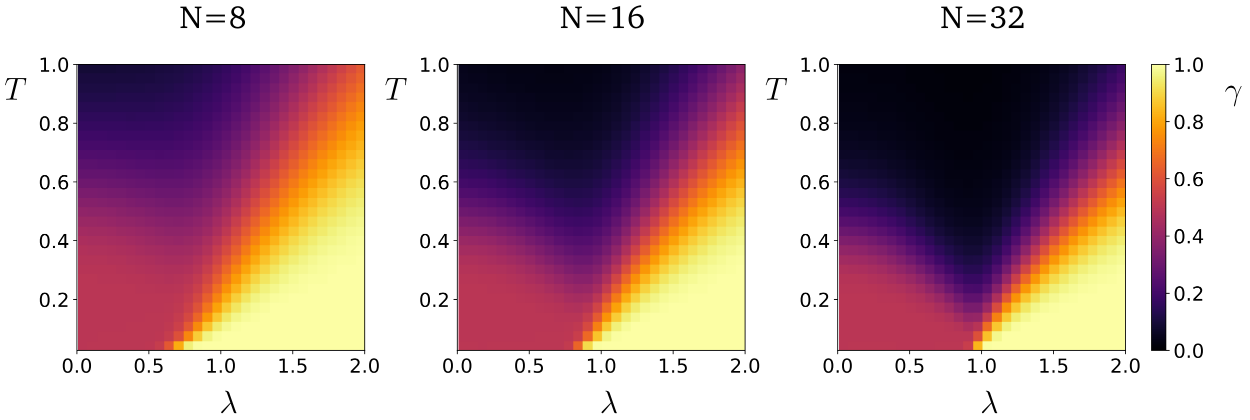

Slika 8.11: Čistoća γ za Isingov model kao funkcija parametra λ i temperature T, izračunata za različite veličine sustava. Temperatura T izražena je u jedinicama J/k_B.

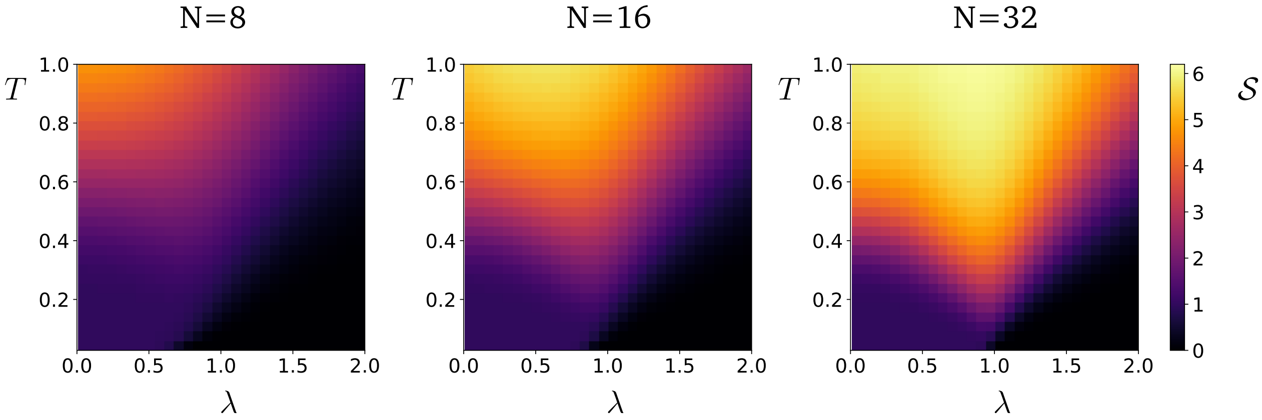

Slika 8.12: Von Neumannova entropija $\mathcal{S}$ za Isingov model kao funkcija parametra λ i temperature T, izračunata za različite veličine sustava. Temperatura T izražena je u jedinicama J/k_B.

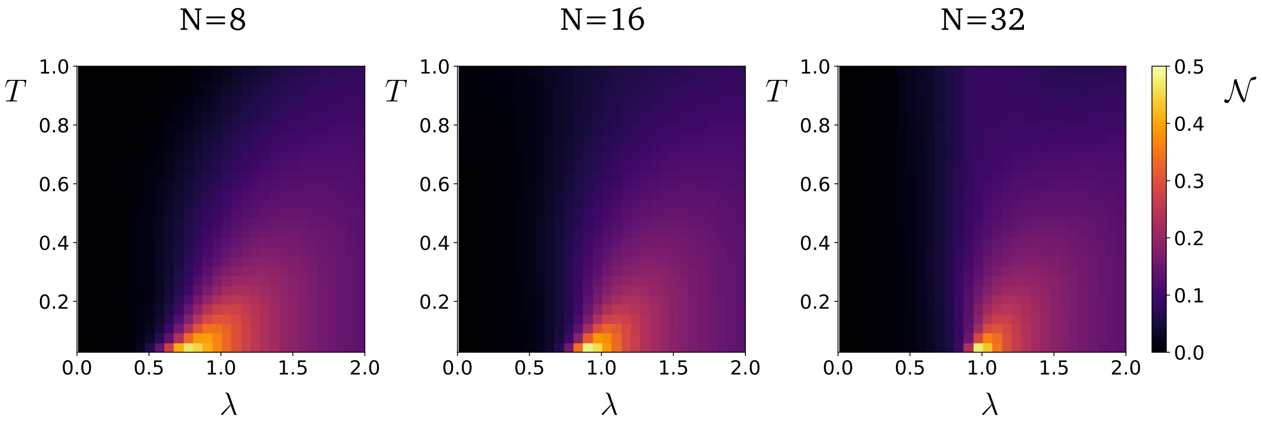

Slika 8.13: Negativnost $\mathcal{N}$ za Isingov model kao funkcija parametra λ i temperature T, izračunata za različite veličine sustava. Temperatura T izražena je u jedinicama J/k_B.

U slučaju $N = 16$, zadržano je $K_0 = 100$ stanja u matrici gustoće, a u slučaju $N = 32$ zadržano je $K_0 = 85$ stanja. U slučaju $N = 8$, dimenzije tenzora su dovoljno male da se tijekom SVD ne moraju skraćivati. Praćenjem iznosa norme matrice gustoće imamo uvid u veličinu pogreške inducirane SVD-om tijekom konverzije LPTN u TTO. Došli smo do zaključka da se u kritičnoj točki $\lambda_c = 1$ mogu očekivati točni rezultati do temperature do $T \approx 0.5$ za $N = 16$ i do $T \approx 0.3$ za $N = 32$. Očekivano je da greška raste s temperaturom, zbog toga što viša temperatura implicira veći broj pobuđenih stanja koja pridonose matrici gustoće. Također, očekuje se da je ova greška manja za vrijednosti parametra λ dalje od kritične točke, gdje je zbog većih procijepa u energetskom spektru Isingovog modela doprinos osnovnog stanja otporniji na temperaturu. U području kritične točke energetski procijep između osnovnog i prvog pobuđenog stanja je najmanji, stoga se u tom režimu pobuđena stanja pojavljuju s većim vjerojatnostima, što zahtijeva veći broj stanja uključen u matricu gustoće. Za $N = 8$, ova greška nije prisutna jer se dimenzije ne skraćuju. Treba napomenuti da na točnost rezultata također utječe i diskretizacija vremena načinjena tijekom imaginarne vremenske evolucije.

Rényieve entropije u kritičnoj točki $\lambda_c = 1$ prikazane su na Slici 8.14

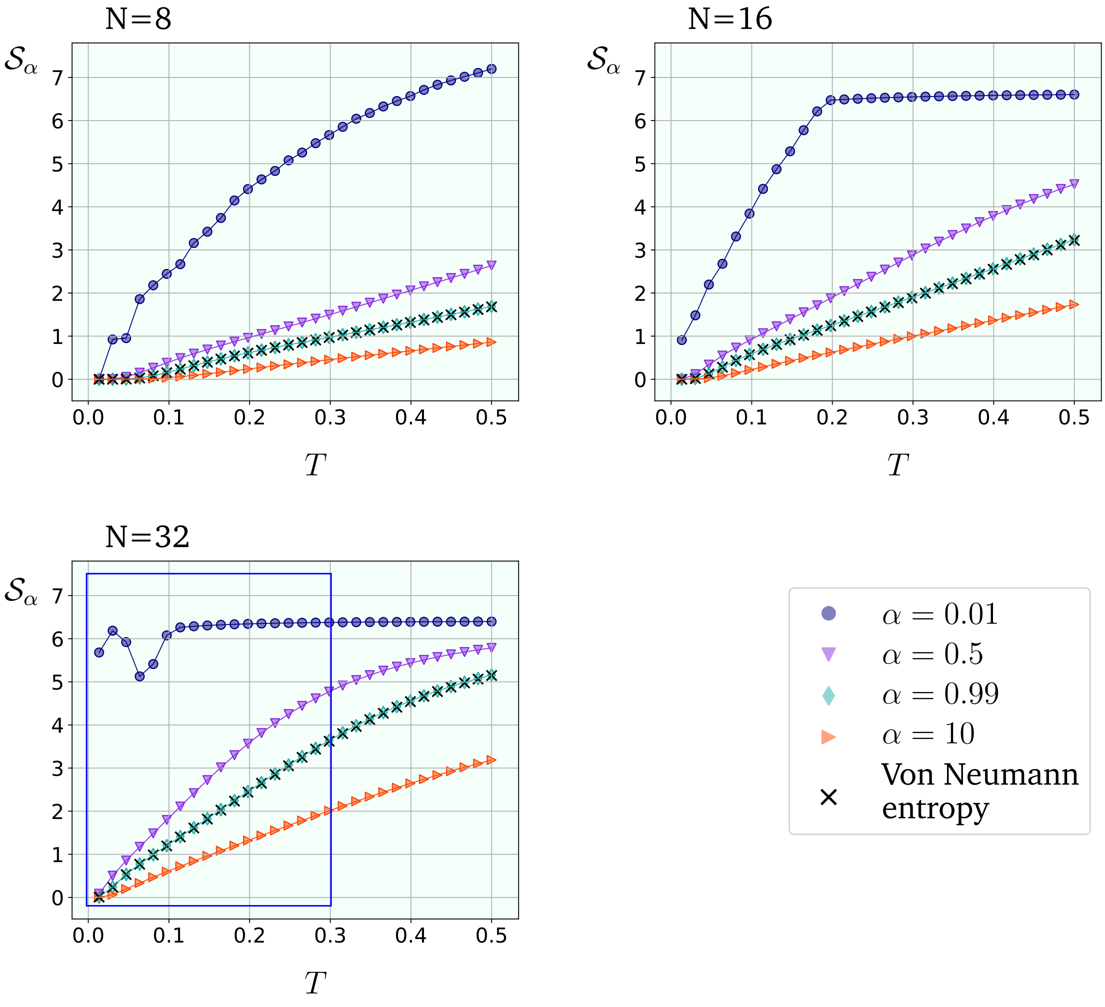

Slika 8.14: Rényieve entropije S_α kao funkcije temperature T izračunate za Isingov model za različite vrijednosti parametra α. Podaci u kritičnoj točki $\lambda_c = 1$. Podaci su izračunati za veličine sustava $N = 8$ (gore lijevo), $N = 16$ (gore desno) i $N = 32$ (dolje lijevo). Dodatno, prikazana je Von Neumannova entropija kako bi se potvrdilo slaganje s Rényijevom entropijom u granici $\alpha \longrightarrow 1$. Kao posljedica pogreške SVD skraćivanja dimenzija, za $N = 32$ očekujemo točne rezultate do $T \approx 0.3$, označeno plavim pravokutnikom. Von Neumannova entropija također je prikazana kako bi se potvrdilo podudaranje s Rényijevom entropijom u granici $\alpha \longrightarrow 1$. Temperatura T izražena je u jedinicama J/k_B.

Nadalje, izračunate mjere prepletenosti u kritičnoj točki $\lambda_c = 1$ prikazane su na Slici 6.13. Budući da izračunavanje prepletenosti formacije zahtijeva minimizacije nad K_0^2 parametara (za detalje vidi [30]), da bi se postigla konvergencija rješenja, dimenzija K_0, odnosno broj stanja zadržanih u matrici gustoće dodatno je smanjen. Smanjili smo K_0 postavljanjem njegove maksimalne vrijednosti na 20 i nadalje odbacili sva pobuđena stanja $|\psi_j\rangle$ s odgovarajućim vjerojatnostima p_j takvim da je $p_j/p_0 < 10^{-4}$. Vjerojatnost p_0 označava vjerojatnost osnovnog stanja. Budući da bi ograničavanje matrice gustoće na < 20 stanja dovelo do velike pogreške u području

$T > 0.1$, izračunali smo EoF za područje niske temperature, do $T = 0.1$.

Ponovno je moguće primijetiti da konačna temperatura najviše utječe na sustav s najviše čestica. Monotoni pad s temperaturom uočen je u obje mjere prepletenosti.

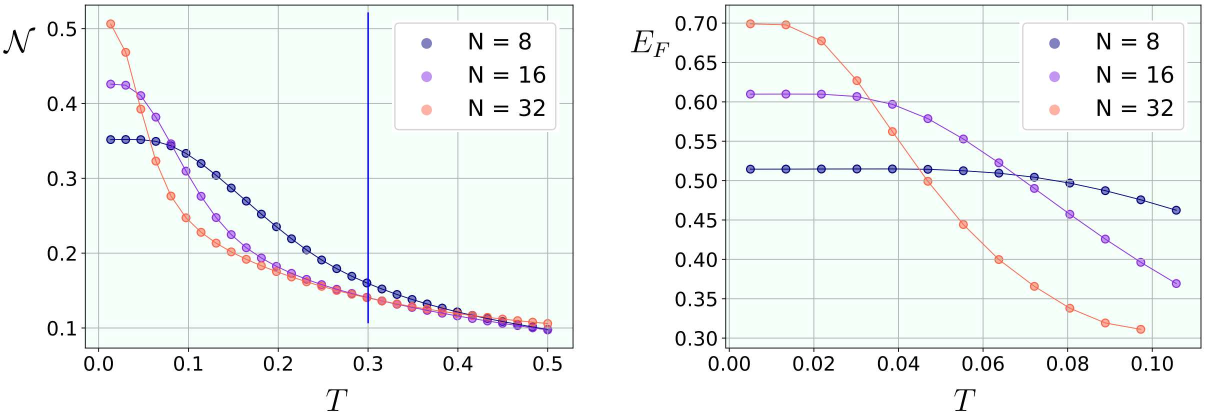

Slika 8.15: Negativnost $\mathcal{N}$ (lijevo) i prepletenost formacije E_F (desno) kao funkcija temperature T, izračunato za Isingov model u kritičnoj točki $\lambda_c = 1$ za različite veličine sustava. Za negativnost: temperaturni raspon u kojem očekujemo točne rezultate označen je plavom linijom za $N = 32$. Temperatura T je izražena u jedinicama J/k_B.

Povrh toga, potvrđeno je skaliranje prepletenosti formacije predviđeno konformalnom teorijom polja:

$$E_F(T, N) = \frac{c}{6} \log N + g(TN^z), \tag{8.27}$$

gdje je c središnji naboj, a z kritični eksponent. Za kritični Isingov model vrijednosti ovih koeficijenata su $c = 1/2$ i $z = 1$. Skaliranje je prikazano na Slici 8.16.

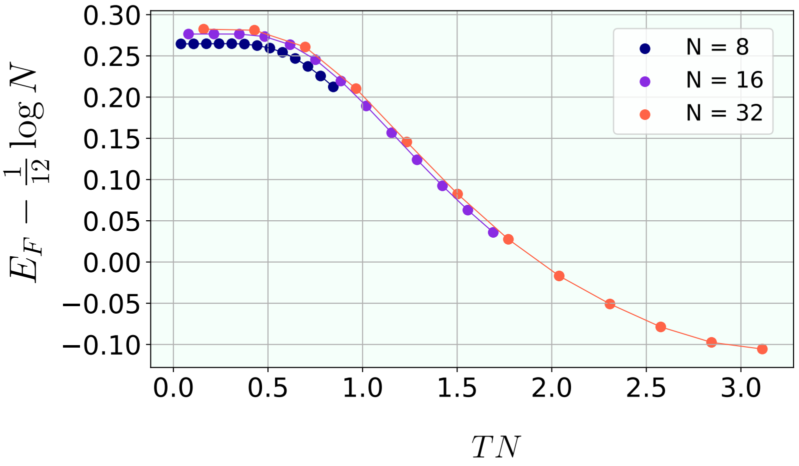

Slika 8.16: Skaliranje prepletenosti formacije izračunato za Isingov model u kritičnoj točki $\lambda_c = 1$. Poklapanje je vrlo dobro. Temperatura T izražena je u jedinicama J/k_B.

Nakon analize Isingovog modela, numeričku metodu koristimo za ispitivanje sustava neutralnih Rydbergovih atoma fiksiranih optičkim pincetama. Rydbergovi atomi su visoko pobuđeni neutralni atomi s glavnim kvantnim brojem $n \geq 10$. S jednim ili više elektrona pobuđenim u visokoenergetsko stanje vrlo daleko od atomske jezgre, Rydbergovi atomi su ogromni - njihov promjer može biti do reda veličine μm, što ih čini 10^4 puta većima od neutralnog atoma u osnovnom stanju. Posljedično, pokazuju vrlo zanimljiva svojstva u usporedbi s niskoenergetskim neutralnim atomima. Svojstvo koje nas posebno zanima je njihov veoma jaki dipolni moment induciran elektronom udaljenim daleko od jezgre. Kada su atomi blizu jedan drugoga, njihovi dipolni momenti uzrokuju međusobno odbojne interakcije te se energetski nivo stanja u kojemu su oba atoma pobuđena u Rydbergovo stanje podižu prema većim energijama. Taj se energetski pomak skalira kao $1/R^6$, gdje je R udaljenost između atoma, sa skaliranjem pripadnog množećeg koeficijenta kao n^{11}. Stoga je postojanje dvaju prostorno bliskih atoma u pobuđenom Rydbergovom stanju energetski izrazito nepovoljno i efektivno onemogućeno. Opisani mehanizam naziva se Rydbergova blokada, a događa se unutar određenog radijusa oko atoma pobuđenog u Rydbergovo stanje.

Budući da Rydbergova blokada sprječava pobuđivanje više prostorno bliskih atoma u Rydbergovo stanje, pobuđivanjem jednog atoma u Rydbergovo stanje efektivno kontroliramo stanja ostalih atoma. Ove interakcije koje možemo kontrolirati ključna su značajka koja čini Rydbergove atome dobrim kandidatima za fizičke predstavnike kubita [59]. Privlačna kvaliteta Rydbergovih atoma kao fizičke kvantne računalne platforme je njihova skalabilnost do velikih veličina sustava. Budući da se radi o identičnim neutralnim atomima čija jedina interakcija dolazi od Van der Waalsovih interakcija, jednostavnost njihove strukture omogućuje nam pakiranje velikog broja neutralnih atoma na točno definirane pozicije pomoću optičke pincete [60,61]. Rydbergovim atomima lako se eksperimentalno manipulira s vanjskim poljima te pokazuju duga vremena koherencije, koja se mogu iskoristiti za realizaciju kvantnih logičkih vrata visoke vjernosti [62–64]. Također, pokazali su se vrlo uspješnim alatima za platforme kvantnih simulatora [65–68].

U pojednostavljenoj slici, sustav se može modelirati spin-$1/2$ modelom sa stanjem $|\downarrow\rangle$ koje predstavlja niskoenergetsko stanje, i stanjem $|\uparrow\rangle$ koje predstavlja visoko pobuđeno Rydbergovo stanje [69–71]. U aproksimaciji rotirajućeg vala (eng. *rotat-*

ing wave approximation) te uzimajući u obzir samo interakcije između prvih susjeda, Hamiltonijan se može zapisati kao:

$$\hat{H} = J\Big(\sum_{i=1}^{N-1} n_z^i n_z^{i+1} + \tilde{\Omega}\sum_{i=1}^{N} \sigma_x^i\Big), \tag{8.28}$$

gdje je $n_z = \frac{1}{2}(\sigma_z + 1)$. Ovdje je parametar $\tilde{\Omega}$ proporcionalan Rabijevoj frekvenciji, a izraz σ_x^i opisuje pobudu lasera. Član interakcije $n_z^i n_z^{i+1}$ opisuje Rydbergovu blokadu - kada je jedna od čestica u paru u stanju $|\downarrow\rangle$, interakcija nestaje. Kada su obje čestice u stanju $|\uparrow\rangle$, energija interakcije se povećava. Parametar J ponovno određuje energetsku skalu Hamiltonijana.

Slično kao u slučaju Isingovog modela, i kod Rydbergovog modela očekujemo manifestaciju dva režima, ovisno o vrijednosti parametra laserske pobude $\tilde{\Omega}$. Kada je $\tilde{\Omega}$ velik, član s σ_x predstavlja glavni doprinos u Hamiltonijanu i stoga osnovno stanje odgovara sustavu sa svim spinovima poredanim duž x-osi. Ovaj slučaj analogan je Isingovom $\lambda \gg 1$ scenariju. Kada je $\tilde{\Omega}$ malen, vodeći doprinos dolazi od Rydbergove interakcije. Ovaj režim favorizira bilo koju kombinaciju orijentacije spina u kojoj dva susjedna spina nisu poravnata u istom smjeru duž z-osi. U granici nestajanja $\tilde{\Omega}$, malo detaljnija analiza pokazuje da degeneracija osnovnog stanja u ovisnosti o broju čestica slijedi Fibonaccijev niz. Za $N = 8$, osnovno stanje je 55-struko degenerirano, za $N = 16$ je 2584-struko degenerirano, a za $N = 32$ je 2178309-struko degenerirano. Takva velika degeneracija osnovnog stanja uvelike će smanjiti točnost naše metode u području niskih $\tilde{\Omega}$.

Kao i kod Isingovog modela, broj energetskih stanja u matrici gustoće K_0 je postavljen na $K_0 = 100$ za $N = 16$ i $K_0 = 85$ za $N = 32$. Za slučaj $N = 8$ ova dimenzija nije reducirana, odnosno uzeta je maksimalna moguća vrijednost $K_0 = 256$.

Kako bi dobili uvid u kvalitativno ponašanje modela, izračunavamo čistoću, Von Neumannovu entropiju i negativnost kao funkcije parametra $\tilde{\Omega}$ i temperature T. Čistoća je prikazana na Slici 8.17. Možemo uočiti dva različita područja. U području (otprilike) ispod dijagonale sustav je dominantno u osnovnom stanju, tj. stanju svih spinova poredanih u smjeru x. Ova konfiguracija ostaje otpornija s temperaturom u zoni većeg $\tilde{\Omega}$ jer povećanje $\tilde{\Omega}$ povećava energetski procijep između osnovnog i pobuđenog stanja Hamiltonijana iz (8.28). U drugom području, iznad dijagonale, čistoća je vrlo blizu nuli. Povećanje veličine sustava čini granicu između ovih regija jasnijom. Ista dva područja mogu se prepoznati i kod Von Neumannove entropije (Slika 8.18).

Promatrajući izračunatu negativnost na Slici 8.19, identificiramo točku najveće isprepletenosti oko $\tilde{\Omega} = 0.05$. Analogno s Isingovim modelom, gdje je najviše prepletenosti bilo prisutno na točki loma degeneracije osnovnog stanja $\lambda_c = 1$, u numerički egzaktno izračunatom Rydbergovom spektru za $N = 8$, na $\tilde{\Omega} = 0.05$ uočavamo križanje dvaju pobuđenih stanja (Slika 8.20).

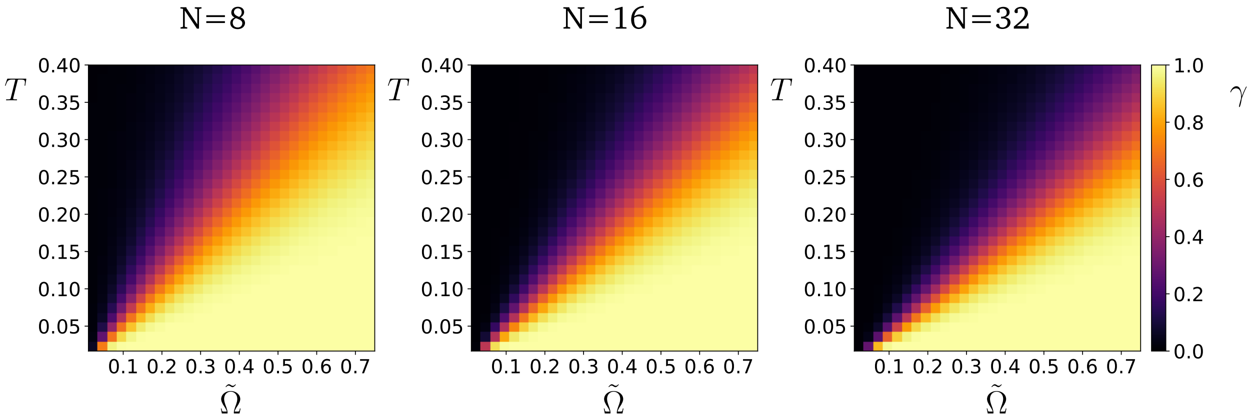

Slika 8.17: Čistoća γ za model Rydbergovih atoma kao funkcija parametra $\tilde{\Omega}$ i temperature T izračunate za različite veličine sustava. Temperatura T izražena je u jedinicama J/k_B.

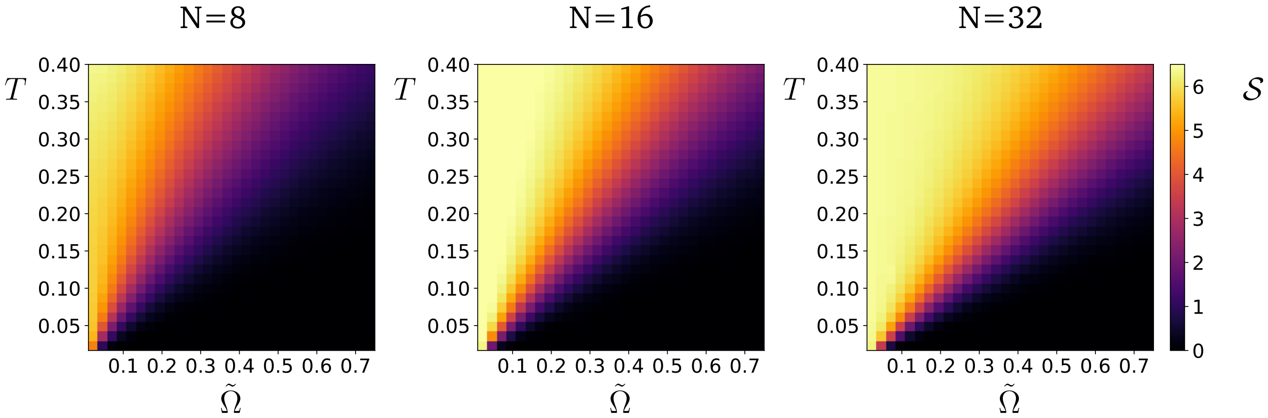

Slika 8.18: Von Neumannova entropija $\mathcal{S}$ za model Rydbergovih atoma kao funkcija parametra $\tilde{\Omega}$ i temperature T izračunata za različite veličine sustava. Temperatura T izražena je u jedinicama J/k_B.

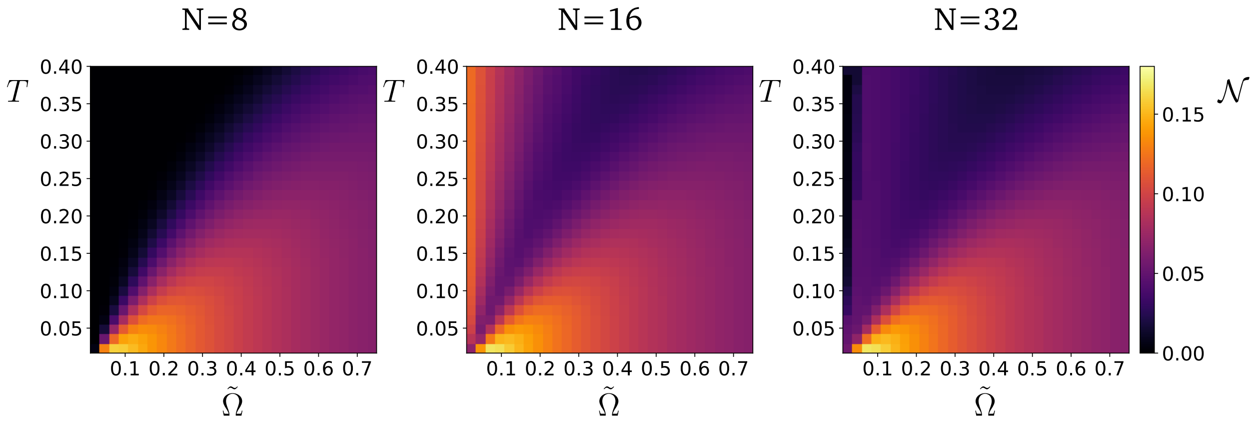

Slika 8.19: Negativnost $\mathcal{N}$ za model Rydbergovih atoma kao funkcija parametra $\tilde{\Omega}$ i temperature T izračunata za različite veličine sustava. Temperatura T izražena je u jedinicama J/k_B.

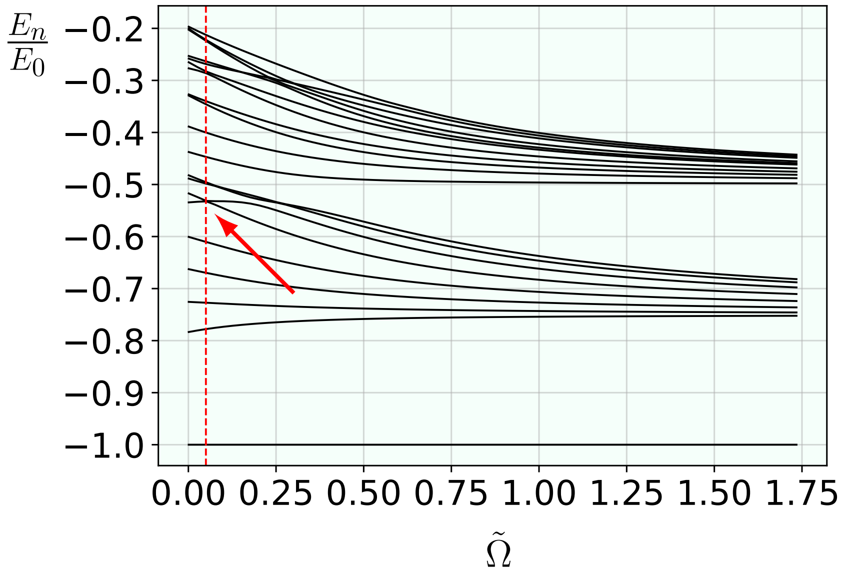

Slika 8.20: Energetski nivoi modela Rydbergovih atoma E_n podijeljeni s energijom osnovnog stanja E_0 kao funkcija parametra $\tilde{\Omega}$. Okomita crvena linija nalazi se na $\tilde{\Omega} = 0.05$ i označava točku najveće prepletenosti. Crvena strelica pokazuje točku križanja energetskih nivoa pobuđenih stanja.

U slučaju $N = 16$, za niske vrijednosti parametra $\tilde{\Omega}$ primjećujemo rast negativnosti s temperaturom. Očekujemo da je to posljedica pogreške koja proizlazi iz skraćivanja dimenzije veze K_0. Isti se učinak ne može primijetiti za $N = 8$, gdje dimenzije veze nisu skraćene.

Kao i u slučaju Isingovog modela, u točki najveće prepletenosti, $\tilde{\Omega} = 0,05$, analizirali smo grešku induciranu kraćenjem dimenzija tenzora tijekom SVD u konverziji LPTN u TTO. Došli smo do zaključka da se točni rezultati u slučaju $N = 16$ i $N = 32$ čestice mogu očekivati samo u području vrlo niskih temperatura, do otprilike $T \approx 0.03$ za $N = 16$ i $T \approx 0.02$ za $N = 32$. To je očekivano, budući da se točka

$\tilde{\Omega} = 0.05$ nalazi vrlo blizu $\tilde{\Omega} = 0$, gdje je osnovno stanje ekstremno degenerirano. U $\tilde{\Omega} = 0$ vrlo velik broj stanja doprinosi jednakim vjerojatnostima te stoga reduciranje dimenzije K_0 neizbježno odbacuje dio relevantnih stanja i rezultira nezanemarivom greškom.

Izračunate Rényieve entropije u točki najveće prepletenosti nalaze se na Slici 8.21. Izračunate mjere prepletenosti - negativnost i prepletenost formacije, prikazane su na Slici 8.22. Očekivano područje točnih rezultata u slučaju $N = 16$ i $N = 32$ čestica označeno je crvenom, odnosno plavom linijom. Vrijednosti svojstava u području viših temperatura služe kao kvalitativni uvid. Treba imati na umu da, iako se može primjetiti križanje krivulja negativnosti za $N = 16$ i $N = 32$, ti su učinci unutar temperaturnog raspona u kojemu se rezultati ne mogu smatrati točnima. Pri izračunavanju prepletenosti formacije, kao i u slučaju Isingovog modela, dimenzija K_0 dodatno je smanjena prema kriteriju objašnjenom kod analize Isingovog modela. Prepletenost formacije je izračunata za temperaturni raspon do $T = 0.01$.

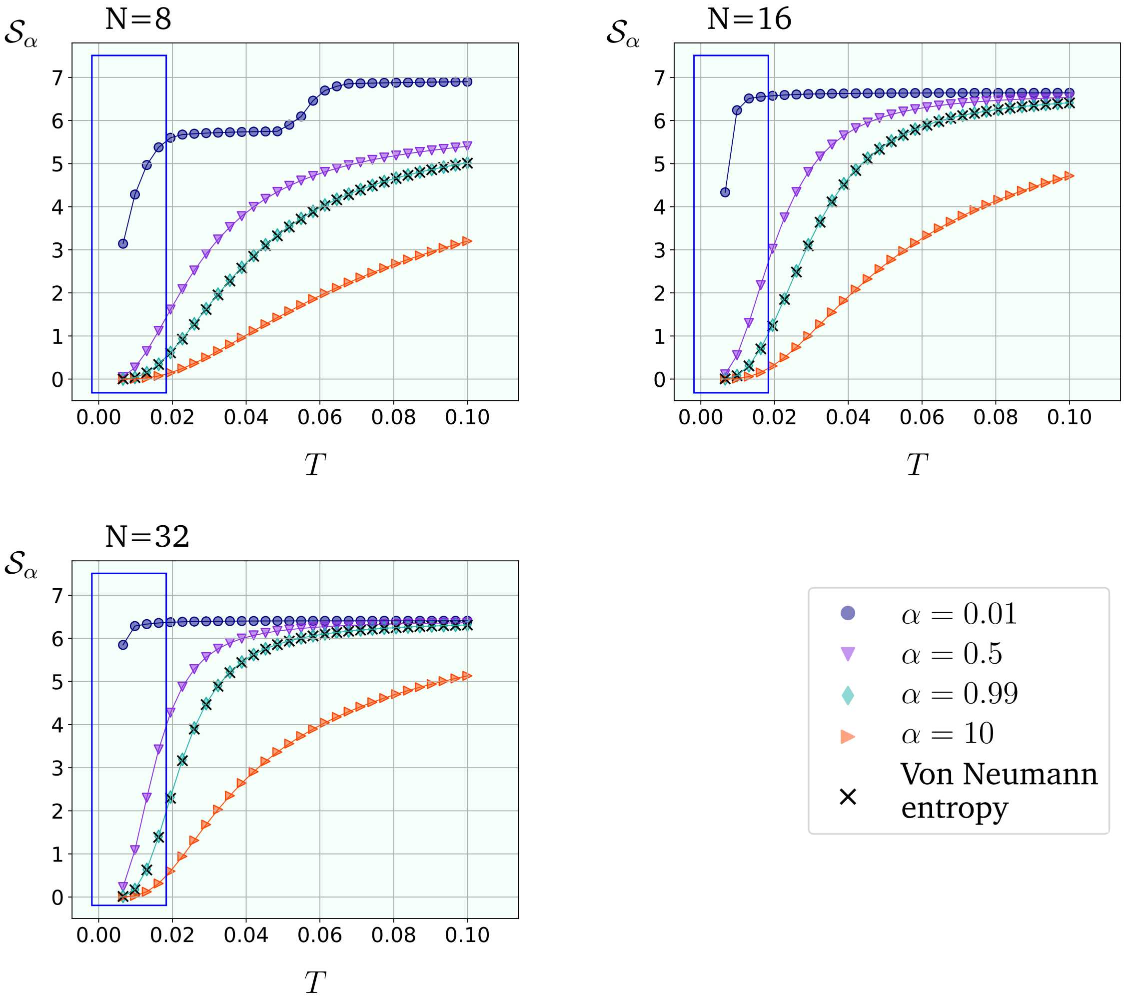

Slika 8.21: Rényijeve entropije $\mathcal{S}_\alpha$ kao funkcije temperature T, izračunata za Rydbergov model atoma za različite vrijednosti parametra α. Podaci u točki maksimalne prepletenosti $\Omega = 0,05$. Podaci su prikazani za veličine sustava $N = 8$ (gore lijevo), $N = 16$ (gore desno) i $N = 32$ (dolje lijevo). Dodatno, prikazana je Von Neumannova entropija kako bi se potvrdilo slaganje s Rényijevom entropijom u granici $\alpha \longrightarrow 1$. Kao posljedica pogreške SVD skraćivanja dimenzija, za $N = 16$ i $N = 32$ očekujeme točne rezultate u područjima unutar označenih pravokutnika. Vrijednosti izračunate u području viših temperatura služe kao kvalitativni uvid. Temperatura T izražena je u jedinicama J/k_B.

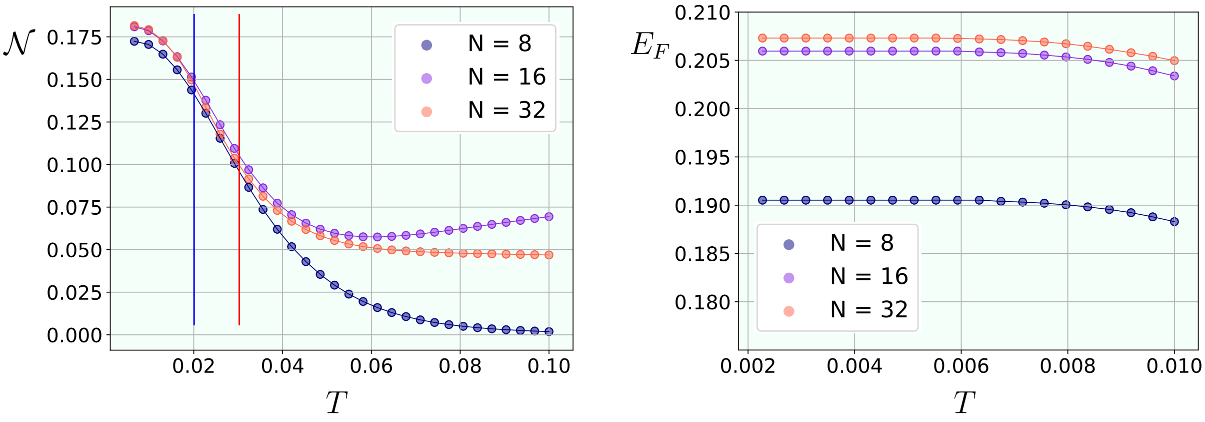

Slika 8.22: Negativnost $\mathcal{N}$ (lijevo) i prepletenost formacije E_F (desno) kao funkcija temperature T, izračunato za Rydbergov model atoma u točki maksimalne prepletenosti $\tilde{\Omega} = 0.05$ za različite veličine sustava. Za negativnost: temperaturni raspon u kojem očekujemo točne rezultate označen je crvenom linijom za $N = 16$ i plavom linijom za $N = 32$. Temperatura T izražena je u jedinicama J/k_B.

8.6 HR nazivi slika i tablica

List of Figures

List of Tables

Bibliography

[1] Feynman, R. P. Simulating physics with computers. International Journal of Theoretical Physics. Vol. 21(6-7), 467–488 (1982).

[2] Zhou, T.; Shen, J.; Li, X.; Wang, C.; Shen, J. Quantum Cryptography for the Future Internet and the Security Analysis. Security and Communication Networks. Vol. 2018, 1–7 (2018).

[3] Giani, A. Quantum computing opportunities in renewable energy. Nature Computational Science. Vol. 1(2), 90–91 (2021).

[4] Montanaro, A. Quantum algorithms: an overview. Npj Quantum Information. Vol. 2(1) (2016).

[5] Blatt, R.; Wineland D. Entangled states of trapped atomic ions. Nature. Vol. 453, 1008-1015 (2008).

[6] Brown, K. R.; Chiaverini, J.; Sage, J. M.; Häffner, H. Materials challenges for trapped-ion quantum computers. Nature Reviews Materials. Vol. 6, 892–905 (2021).

[7] Pino, J.M.; Dreiling, J.M.; Figgatt, C. et al. Demonstration of the trapped-ion quantum CCD computer architecture. Nature. Vol. 592(7853), 209–213 (2021).

[8] Clarke, J.; Wilhelm F. K. Superconducting quantum bits. Nature. Vol. 453, 1031 (2008).

[9] Arute, F.; Arya, K.; Babbush, R. et al. Quantum supremacy using a programmable superconducting processor. Nature. Vol. 574(7779), 505–510 (2019).

[10] Wu, Xiaoling et al. A Concise Review Of Rydberg Atom Based Quantum Computation And Quantum Simulation. Chinese Physics B, vol 30(2), 020305 (2021).

[11] Bluvstein, D.; Levine, H.; Semeghini, G. et al. A quantum processor based on coherent transport of entangled atom arrays. Nature. Vol 604, 451–456 (2022).

[12] Weimer, H.; Müller, M.; Lesanovsky, I. et al. A Rydberg quantum simulator. Nature Phys. Vol. 6, 382–388 (2010).

[13] Urban, E.; Johnson, T.; Henage, T. et al. Observation of Rydberg blockade between two atoms. Nature Phys. Vol. 5, 110–114 (2009).

[14] Eisert, J.; Cramer, M.; Plenio, M. B. Colloquium: Area laws for the entanglement entropy. Reviews of Modern Physics. Vol. 82(1), 277–306 (2010).

[15] Wolf, M. M.; Verstraete, F.; Hastings, M. B.; Cirac, J. I. Area Laws in Quantum Systems: Mutual Information and Correlations. Physical Review Letters. Vol. 100(7) (2008).

[16] Perez-Garcia, D.; Verstraete, F.;, Wolf, M.M.; Cirac, J.I.; Matrix Product State Representations. Quantum Information Computation. Vol. 7(5), 401-430 (2007).

[17] Östlund, S.; Rommer, S. Thermodynamic Limit of Density Matrix Renormalization. Physical Review Letters. Vol. 75(19), 3537–3540 (1995).

[18] Dukelsky, J.; Martín-Delgado, M. A.; Nishino, T.; Sierra, G.; Equivalence of the variational matrix product method and the density matrix renormalization group applied to spin chains. Europhysics Letters (EPL). Vol. 43(4), 457–462 (1998).

[19] Verstraete, F.; Porras, D.; Cirac, J. I. Density Matrix Renormalization Group and Periodic Boundary Conditions: A Quantum Information Perspective. Physical Review Letters. Vol. 93(22) (2004).

[20] White, S. R. Density matrix formulation for quantum renormalization groups. Physical Review Letters. Vol. 69(19), 2863–2866 (1992).

[21] Montangero, S.; Introduction to Tensor Network Methods. 1st ed. Springer, 2018.

[22] Orús, R. A practical introduction to tensor networks: Matrix product states and projected entangled pair states. Annals of Physics. Vol. 349, 117–158 (2014).

[23] Montangero, S.; Rico, E.; Silvi, P. Loop-Free Tensor Networks for High-Energy Physics. Philosophical Transactions of the Royal Society A. Vol. 380(2216) (2021).

[24] White, S. R. Minimally Entangled Typical Quantum States at Finite Temperature. Physical Review Letters. Vol. 102(19) (2009).

[25] Rényi, A. On Measures of Entropy and Information. In: Proceedings of the 4th Berkeley Symposium on Mathematics. Statistics and Probability. Vol. 1, 547-561 (1960).

[26] Bennett, C. H.; DiVincenzo, D. P.; Smolin, J. A.; Wootters, W. K. Mixed-state entanglement and quantum error correction. Physical Review A. Vol. 54(5), 3824–3851 (1996).

[27] Peres, A. Separability Criterion for Density Matrices. Physical Review Letters. Vol. 77(8), 1413–1415 (1996).

[28] Horodecki, M.; Horodecki, P.; Horodecki, R. Separability of mixed states: necessary and sufficient conditions. Physics Letters A. Vol. 223(1-2), 1–8 (1996).

[29] Shi, Y.-Y.; Duan, L.-M.; Vidal, G. Classical simulation of quantum many-body systems with a tree tensor network. Physical Review A. Vol. 74(2) (2006).

[30] Arceci, L.; Silvi, P.; Montangero, S. Entanglement of formation of mixed many-body quantum states via Tree Tensor Operators. Physical Review Letters. Vol. 128 (2022).

[31] Werner, A. H.; Jaschke, D.; Silvi, P.; Kliesch, M.; Calarco, T.; Eisert, J.; Montangero, S. Positive Tensor Network Approach for Simulating Open Quantum Many-Body Systems. Physical Review Letters. Vol. 116(23) (2016).

[32] Vidal, G. Efficient Simulation of One-Dimensional Quantum Many-Body Systems. Physical Review Letters. Vol. 93(4) (2004).

[33] Nielsen, M.A.; Chuang, I.L. Quantum computation and quantum information. 1st ed. Cambridge University Press, 2004.

[34] Bohr, N. Can Quantum-Mechanical Description of Physical Reality be Considered Complete? Physical Review. Vol. 48(8), 696–702 (1935).

[35] Bell, J.S.. On the Einstein, Podolsky and Rosen Paradox. Physics Physique Fizika. Vol. 1(3), 195-290, (1964).

[36] Dowling, J. P.; Milburn, G. J. Quantum technology: the second quantum revolution. Philosophical Transactions of the Royal Society A: Mathematical, Physical and Engineering Sciences. Vol. 361(1809), 1655–1674 (2003).

[37] Werner, R. F. Quantum states with Einstein-Podolsky-Rosen correlations admitting a hidden-variable model. Physical Review A. Vol. 40(8), 4277–4281 (1989).

[38] Bruß, D. Characterizing entanglement. Journal of Mathematical Physics. Vol. 43(9), 4237–4251 (2002).

[39] Jizba, P. The world according to Rényi: thermodynamics of multifractal systems. Annals of Physics. Vol. 312(1), 17–59 (2004).

[40] Li, F. An Introduction to Entanglement Measures. https://homes.psd.uchicago.edu/ sethi/Teaching/P243-W2020/final-papers/li.pdf

[41] Plenio, M. B.; Virmani, S. An introduction to entanglement measures. Quantum Information & Computation. Vol. 7(1), 1-51 (2007)

[42] Vedral, V.; Plenio, M. B.; Rippin, M. A.; Knight, P. L. Quantifying Entanglement. Physical Review Letters. Vol. 78(12), 2275–2279 (1997).

[43] Bennett, C. H.; Bernstein, H. J.; Popescu, S.; Schumacher, B. Concentrating partial entanglement by local operations. Physical Review A. Vol. 53(4), 2046–2052 (1996).

[44] Wootters, W. K. Entanglement of Formation of an Arbitrary State of Two Qubits. Physical Review Letters. Vol. 80(10), 2245–2248 (1998).

[45] Brunton, S. L.; Kutz, J. N. Data Driven Science & Engineering: Machine Learning, Dynamical Systems, and Control. 1st ed. Cambridge University Press, 2019.

[46] Schollwöck, U. The density-matrix renormalization group. Reviews of Modern Physics. Vol. 77(1), 259–315 (2005).

[47] Verstraete, F.; García-Ripoll, J. J.; Cirac, J. I. Matrix Product Density Operators: Simulation of Finite-Temperature and Dissipative Systems. Physical Review Letters. Vol. 93(20) (2004).

[48] Zwolak, M.; Vidal, G. Mixed-State Dynamics in One-Dimensional Quantum Lattice Systems: A Time-Dependent Superoperator Renormalization Algorithm. Physical Review Letters. Vol. 93(20) (2004).

[49] Kittel, C. Elementary statistical physics. John Wiley Sons, Inc., 1958.

[50] Hatano, N.; Suzuki, M. Finding Exponential Product Formulas of Higher Orders. Lecture Notes in Physics, 37–68 (2005).

[51] Lin, S.; Zaletel, M.; Pollmann F.; Efficient Simulation of Dynamics in Two-Dimensional Quantum Spin Systems with Isometric Tensor Networks. arXiv:2112.08394 (2021).

[52] Hughston, L. P.; Jozsa, R.; Wootters, W. K. A complete classification of quantum ensembles having a given density matrix. Physics Letters A. Vol. 183(1), 14–18 (1993).

[53] W. Lenz. Beitrag zum Verständnis der magnetischen Erscheinungen in festen Körpern. Phys. Z. Vol. 21, 613 (1920).

[54] Ising, E. Beitrag zur Theorie des Ferromagnetismus. Zeitschrift Für Physik. Vol. 31(1), 253–258 (1925).

[55] Onsager, L. Crystal Statistics. I. A Two-Dimensional Model with an Order-Disorder Transition. Physical Review. Vol. 65(3-4), 117–149 (1944).

[56] Calabrese, P.; Cardy, J. Entanglement entropy and conformal field theory. Journal of Physics A: Mathematical and Theoretical. Vol. 42(50), 504005 (2009).

[57] Gallagher, T.F. Rydberg atoms, 1st ed. Cambridge University Press, 2005.

[58] Weber, S. et al. Calculation of Rydberg interaction potentials. Journal of Physics B: Atomic, Molecular and Optical Physics. Vol. 5(13) (2017).

[59] Saffman, M.; Walker, T. G.; Mølmer, K. Quantum information with Rydberg atoms. Reviews of Modern Physics. Vol. 82(3), 2313–2363 (2010).

[60] Barredo, D.; Lienhard, V.; de Léséleuc, S.; Lahaye, T.; Browaeys, A. Synthetic three-dimensional atomic structures assembled atom by atom. Nature. Vol. 561(7721), 79–82 (2018).

[61] Kim, H.; Lee, W.; Lee, H.; Jo, H.; Song, Y.; Ahn, J. In situ single-atom array synthesis using dynamic holographic optical tweezers. Nature Communications. Vol. 7, 13317 (2016).

[62] Jaksch, D.; Cirac, J. I.; Zoller, P.; Rolston, S. L.; Côté, R.; Lukin, M. D. Fast Quantum Gates for Neutral Atoms. Physical Review Letters. Vol. 85(10), 2208–2211 (2000).

[63] Safman, M.; Walker, T.G.; Mølmer, K. Quantum Information with Rydberg Atoms. Reviews of Modern Physics. Vol. 82, 2313 (2010).

[64] Pagano, A.; Weber, S.; Jaschke, D.; Pfau, T.; Meinert, F.; Montangero, S.; Büchler H.P. Error budgeting for a controlled-phase gate with strontium-88 Rydberg atoms. Physical Review Research. Vol. 4(3) (2022).

[65] Hague, J. P.; Downes, S.; MacCormick, C.; Kornilovitch, P. E. Cold Rydberg Atoms for Quantum Simulation of Exotic Condensed Matter Interactions. Journal of Superconductivity and Novel Magnetism. Vol. 27(4), 937–940 (2013).

[66] Lesanovsky, I. Liquid Ground State, Gap, and Excited States of a Strongly Correlated Spin Chain. Physical Review Letters. Vol. 108(10) (2012).

[67] Weimer, H.; Müller, M.; Lesanovsky, I.; Zoller, P.; Büchler, H. P. A Rydberg quantum simulator. Nature Physics. Vol. 6(5), 382–388 (2010).

[68] Keesling, A.; Omran, A.; Levine, H.; Bernien, H.; Pichler, H.; Choi, S.; Samajdar, R.; Schwartz, S.; Silvi, P.; Sachdev, S.; Zoller, P., Endres, M.; Greiner, M.; Vuletić, V.; Lukin, M. D. Quantum Kibble–Zurek mechanism and critical dynamics on a programmable Rydberg simulator. Nature. Vol. 568, 207–211 (2019).

[69] Robicheaux, F.; Hernández, J. V. Many-body wave function in a dipole blockade configuration. Physical Review A. Vol. 72(6) (2005).

[70] De Léséleuc, S.; Weber, S.; Lienhard, V.; Barredo, D.; Büchler, H. P.; Lahaye, T., Browaeys; A. Accurate Mapping of Multilevel Rydberg Atoms on Interacting Spin- 1/2 Particles for the Quantum Simulation of Ising Models. Physical Review Letters. Vol. 120(11) (2018).

[71] Labuhn, H.; Barredo, D.; Ravets, S.; de Léséleuc, S.; Macrì, T.; Lahaye, T.; Browaeys, A. Tunable two-dimensional arrays of single Rydberg atoms for realizing quantum Ising models. Nature. Vol. 534(7609), 667–670 (2016).

[72] Giudici, G.; Angelone, A.; Magnifico, G.; Zeng, Z.; Giudice, G.; Mendes-Santos, T.; Dalmonte, M. Diagnosing Potts criticality and two-stage melting in one-dimensional hard-core boson models. Physical Review B. Vol. 99(9) (2019).